68 / 2-28-87

JB

②

I - 32863

DR 0355-7

SERI/STR-211-3249
DE88001116

October 1987

Stable, High-Efficiency, $CuInSe_2$-Based, Polycrystalline Thin-Film Tandem Solar Cells

Final Subcontract Report
16 March 1984–15 March 1987

R. W. Birkmire
J. E. Phillips
Institute of Energy Conversion
University of Delaware
Newark, Delaware

Prepared under Subcontract No. XL-4-04025-1

Solar Energy Research Institute
A Division of Midwest Research Institute

1617 Cole Boulevard
Golden, Colorado 80401-3393

Operated for the
U.S. Department of Energy
under Contract No. DE-AC02-83CH10093

SERI/STR--211-3249

DE88 001116

Stable, High-Efficiency, $CuInSe_2$-Based, Polycrystalline, Thin-Film Tandem Solar Cells

Final Subcontract Report
16 March 1984-15 March 1987

R. W. Birkmire
J. E. Phillips
Institute of Energy Conversion
University of Delaware
Newark, Delaware

October 1987

SERI Technical Monitor: R. Mitchell

Prepared under Subcontract No. XL-4-04025-1

Solar Energy Research Institute
A Division of Midwest Research Institute

1617 Cole Boulevard
Golden, Colorado 80401-3393

Prepared for the
U.S. Department of Energy
Contract No. DE-AC02-83CH10093

MASTER

Printed in the United States of America
Available from:
National Technical Information Service
U.S. Department of Commerce
5285 Port Royal Road
Springfield, VA 22161

Price: Microfiche A01
Printed Copy A06

SUMMARY

Objectives:

This research effort has as its long-term objective the development of a stable thin-film solar cell of 15% efficiency based on polycrystalline semiconductor materials. The immediate goals were:

1. To develop a transparent CdTe/CdS solar cell of 10% efficiency to couple with a high efficiency $CuInSe_2$ cell in a tandem device configuration. A goal of 60% transmission through the entire CdTe/CdS top cell was an interim goal with a long-term goal of 90% transparency below the CdTe bandgap.

2. To establish the scientific data base required to develop a large-area technology for high efficiency $CuInSe_2$/CdS single junction cells.

3. To analyze the operation of CdTe/CdS and $CuInSe_2$/(CdZn)S heterojunctions and quantify the loss mechanisms controlling performance and relate these to material and processing parameters.

4. To demonstrate a high efficiency tandem cell using polycrystalline materials.

The successful achievement of these objectives will form the basis for the development of high efficiency single or multijunction polycrystalline solar cells with efficiencies of over 15%.

Discussion:

The research program was divided into three tasks: CdTe cell development, $CuInSe_2$ cell development and Tandem Junction Development.

Task I – CdTe Cell Development

The focus of this task was to develop a process for fabricating high efficiency CdTe/CdS cells that is compatible with $CuInSe_2$/CdS cells in either a monolithic (2-terminal) or mechanically stacked (4-terminal) tandem cell configuration. The major problems addressed were control of the p-type conductivity of the CdTe films and development of a reliable transparent ohmic contact to the CdTe. The CdTe films were deposited by thermal evaporation onto a substrate with a transparent contact or on a CdS superstrate. Post deposition heat treatments were used to control the p-type conductivity of the CdTe and to optimize the device performance.

Task II - $CuInSe_2$/CdS Cell Development

This task was divided into three sub-tasks; improvement of $CuInSe_2$ cell efficiency, developing a quantitative model of $CuInSe_2$ film growth, and development of a large area cell technology.

To improve cell efficiency, efforts were directed towards increasing the open circuit voltage by reducing the electron affinity mismatch between the $CuInSe_2$ and CdS. The approach was to increase the bandgap of the CdS by the addition of Zn. The wider bandgap also permits more light to reach the $CuInSe_2$, thus increasing the J_{sc}. Additional improvements in J_{sc} were pursued by reducing the thickness of the CdS window layer. Modelling of the $CuInSe_2$/(CdZn)S device was performed based on I-V measurements as a function of temperature and light intensity and internal photo emission and quantum efficiency measurements. The effects of oxidizing and reducing heat treatments on the $CuInSe_2$/CdS devices were also analyzed using these techniques.

A semi-quantitative model of $CuInSe_2$ film growth relating flux rate, substrate temperature and growth rate to composition was developed. The general applicability of this model to physical vapor deposition, reactive sputtering and film growth by selenization was investigated.

To develop a large area cell technology, efforts were directed towards depositing $CuInSe_2$ films uniformly over a 60 cm² area. The approach was to deposit films by vacuum evaporation using Knudsen type effusion sources. Film uniformity was evaluated by sampling device performance over this area as well as analyzing the composition of the $CuInSe_2$ films. Processing tolerances were examined by analyzing a data base of $CuInSe_2$ cell results with respect to $CuInSe_2$ composition and resistivity and CdS properties.

Task III - Tandem Junction Development

Both monolithic, 2-terminal, and mechanically stacked, 4-terminal, tandem device were investigated. For the 2-terminal configuration, CdTe cells were deposited onto a $CuInSe_2$ cell forming a series connected tandem. For the 4-terminal device, the $CuInSe_2$ and CdTe cells were mechanically coupled and electrically independent. The two device structures were evaluated to determine the effect of device thickness and geometry on the spectral sensitivity. A preliminary process design based for commercial fabrication of tandem cells was developed in order to identify critical material processing issues.

Conclusions:

The major results and accomplishments of this research program are:

- A reproducible cell fabrication process has been developed based on $CuInSe_2$ films grown by Knudsen-type effusion sources. Total area uniformity of the $CuInSe_2$ films exceeds 60 cm^2 based upon $CuInSe_2$/CdS device results.

- The best $CuInSe_2$ cell efficiencies measured at SERI:
  9.4% 1cm^2
  10.7% active area.

- Effect of oxidizing and reducing heat treatments on $CuInSe_2$ cell are to change carrier concentration of the $CuInSe_2$ layer. The change in Fermi level is reflected in V_{oc}. J_o and thus V_{oc}, appear to be controlled by band-to-band recombination.

- The addition of Zn to the CdS does not appreciably change V_{oc}, and analysis of the $CuInSe_2$/(CdZn)S devices indicates that V_{oc} is not dominated by interface recombination.

- A model of $CuInSe_2$ film growth has been developed which shows the latitude in fabricating $CuInSe_2$ films due to a volatile In-Se species.

- A transparent ohmic contact to CdTe device has been developed yielding devices with 8.5% efficiency.

- Analysis of two- and four-terminal tandem devices taking into account area and thickness of individual cells has shown that practically achievable efficiencies of the two device structures can be similar under certain constraints.

List of Contributors

Edgar Ashmead
Thomas Bledsoe
Sally Buchanan
Alicia Canedo
James Cebulka
Savvas Damaskinos
Louis DiNetta
Ronald Dozier
Christopher Field
Sally Gordon
Mary Gorton
Joan Hall
Steven Hegedus
Scott Jackson
Patrick Lasswell
Michele Malanowicz
Brian McCandless
Sheila Moore
Madumita Roy
Bernard Runk
Kenneth Schubert
Stuart Spinner
George Streetman
Herbert Wardell
Cathy Zetterlund

Table of Contents

PAGE

LIST OF FIGURES

LIST OF FIGURES

LIST OF TABLES

PAGE

LIST OF TABLES

SECTION 1.0
INTRODUCTION

Research under a previous contract[1] had resulted in a physical vapor deposition technique for the production of $CuInSe_2$ films that yielded heterojunctions with CdS of about 7% conversion efficiency. Developments in thin film solar cells taking place at that time indicated that the next major increment to thin film solar cell efficiency would be achieved by utilizing the tandem cell concept. Accordingly, a tandem cell development effort was proposed to SERI that would utilize CdS heterojunctions based on $CuInSe_2$ and CdTe. Research on this combination was carried out during 1983 under Subcontract XL-3-03065-01. The major thrusts of that program were to develop a CdTe/CdS heterojunction that would be compatible with the existing $CuInSe_2$/CdS solar cells. The research was directed towards a monolithic structure which required the deposition of the CdTe cells on an existing $CuInSe_2$ cell.

All reported CdTe cells of good efficiency have been made by processes in which the CdS or window layer was deposited first followed by the CdTe layer. This sequence was unusable for the monolithic tandem being developed and accordingly a substantial effort was devoted to developing a CdTe/CdS process in which the first layer deposited was CdTe. At the end of the contract period, a number of major advances have been achieved. A physical vapor deposition (PVD) process for CdTe had been developed and good progress made towards a usable transparent interconnect between the two individual heterojunctions. The requirement was a layer that would make ohmic contact to the top CdS layer of the $CuInSe_2$ cell and also function as an appropriate surface onto which to deposit the CdTe layer. The interconnect must, of course, also make ohmic contact to the CdTe. Although the efficiency achieved did not match those reported for CdTe cells developed elsewhere, it did prove possible to construct CdTe/CdS cells on a transparent contact with efficiencies of the order of 5%. The contact was a sputtered ITO layer onto which was deposited approximately 2-5nm of Cu.

During the contract year some progress was also made on the overall efficiency of the $CuInSe_2$ cells which reached about 8% by the end of the contract. A number of prototype monolithic tandem junctions were assembled which clearly demonstrated voltage addition giving a Voc of over one volt and overall efficiencies of about 3%. In these prototypes devices the efficiency limiting component was clearly the CdTe cell where less than ideal ohmic contacts resulted in severely limited fill factors. Nevertheless, it was demonstrated that sequential production of two junctions could be carried out and the research served to identify the major obstacles to the further development of efficient tandem cells.

This research effort under this contract has the long-term objective of a stable thin-film cell of 15% efficiency based on polycrystalline materials. The immediate objectives were:
a) to develop a CdTe/CdS solar cell of at least 10% conversion efficiency with an interim transparency below the CdTe bandgap of 60% (with the long term goal of 90% transparency below the CdTe bandgap) to couple with the available high efficiency $CuInSe_2$ cell; b) to develop a large-area technology for high efficiency $CuInSe_2$/CdS single junction cells; and c) to analyze the operation of the present CdTe/CdS and $CuInSe_2$/CdS heterojunctions and quantify the loss mechanisms controlling efficiency. The results and conclusions of this research effort are described in this report.

1.1 $CuInSe_2$ FILM GROWTH AND CELL FABRICATION

$CuInSe_2$ films are deposited by thermal evaporation from three elemental effusion sources. The fluxes of the Cu, In and Se are controlled by precise control of the effusion source temperature in contrast to the open boat system used by Mickelsen[2]. A complete description of the deposition system and operating procedures is presented in References [3] and [4].

The substrate holder contains a 3 x 3 array of nine 2.5 x 2.5 cm^2 substrates. The substrates are radiatively heated and a thermocouple imbedded in one of the substrates is used to control the temperature. Two uncoated 7059 glass slides are used for film diagnostics. One is shuttered to provide samples of the individual layers during multilayer deposition. Typically, six of the substrates are Corning 7059 glass sputter coated with 1 μm of Mo to provide an ohmic contact to the $CuInSe_2$ film. It should be noted that Mo layers much less than about 1 μm thick do not form an adequate contact. This suggests that an interaction between the Mo and Cu, In and Se occurs during film growth modifying at least the Mo-$CuInSe_2$ interface.

The $CuInSe_2$ films are deposited in two stages as reported by Mickelsen and Chen[2]. The initial layer of the film is typically deposited at a substrate temperature between 300 and 350°C, resulting in a slightly copper-rich film. For the second layer, the substrate temperature is raised to 450°C and the indium rate is increased to yield a copper deficient layer. (The composition ranges are 24-30% Cu, 23-26% In, 46-51% Se for the first layer and 15-20% Cu, 27-30% In, 51-57% Se for the second layer.) The $CuInSe_2$ film growth rate is about 10 A/sec and the thickness of the composite film is about 3 μm.

The average effusion rates for Cu, In and Se are estimated from mass loss measurements and are about 6, 15 and 80 mg/min respectively. Only about 40-50% of the Se evaporated and 70% of the In is actually incorporated into the film. This implies that the film composition is controlled by substrate temperature, surface reactions and re-evaporation rates rather than solely by incident flux rates.

A qualitative model of $CuInSe_2$ film growth has been developed which relates flux rates, substrate temperature and film growth rate to film composition. Appendix 1 is paper (A Chemical Reaction Model for Physical Vapor Deposition of Compound Semiconductor Films) describing the model and its applicability to $CuInSe_2$ film growth as well as other semiconductors.

CdS-(CdZn)S Films

To form efficient $CuInSe_2$/CdS heterojunctions, the CdS conductivity must be high enough so that the field is nearly all in the $CuInSe_2$ and the Fermi level is close to the conduction band to maintain a high V_{oc}. CdS films with conductivities of 10 to 10^{+3} S/cm are easily obtained using indium doping. The upper limit of the conductivity is dictated by loss of transmission through the CdS at high indium doping levels.

The CdS(In) films are deposited by physical vapor deposition in a separate evaporation system using a powder CdS source and an indium source identical to that used in the $CuInSe_2$ system. The indium doped CdS is deposited onto the $CuInSe_2$ substrates maintained at 200°C at a growth rate of 130 Å/sec. The CdS film thickness has been varied from 0.5 to 7.5 μm. Thin CdS films (less than 2.0 μm) increase the transparency of the film resulting in improved short circuit current of the $CuInSe_2$/CdS devices.

(CdZn)S films are deposited using a stacked source bottle where the ZnS is in the upper chamber. A two zone heater assembly is used to control the relative temperatures of the ZnS and CdS, thus controlling the effusion rates and composition of the growing film. Films with 0-25% Zn have been grown with resistivities from 10^{-3}-10^{-1} Ω-cm using In as a dopant.

Top Contact and Cell Delineation

A sputtered ITO film, ~ 2500 Å thick and a Ni bus bar are deposited onto the CdS to provide the top contact. The cell area and contacts are defined by a photolithography-etching procedure in which excess CdS and ITO are removed by a concentrated HCl etch; the Ni bus bars are etched with 20% HNO_3. The procedure yields 12 cells each 3 x 3 mm² on a 2.5 x 2.5 cm² substrate with an active area of ~0.08 cm². See Figure 1.1. Using this configuration, the uniformity across a substrate can be evaluated from the individual device results. Additionally, on uniform substrates, 12 identical cells are available for additional experiments. For 1cm^2 cells, a metal grid which is nominally 95% transparent is deposited on the ITO and the device area defined by photolithography. See Figure 1.2. There are also four 3x3mm^2 cells delineated on each sample with the 1cm^2 cell. The completed cells are then heat treated in air at 200°C to optimize the cell performance as described in section 1.3.

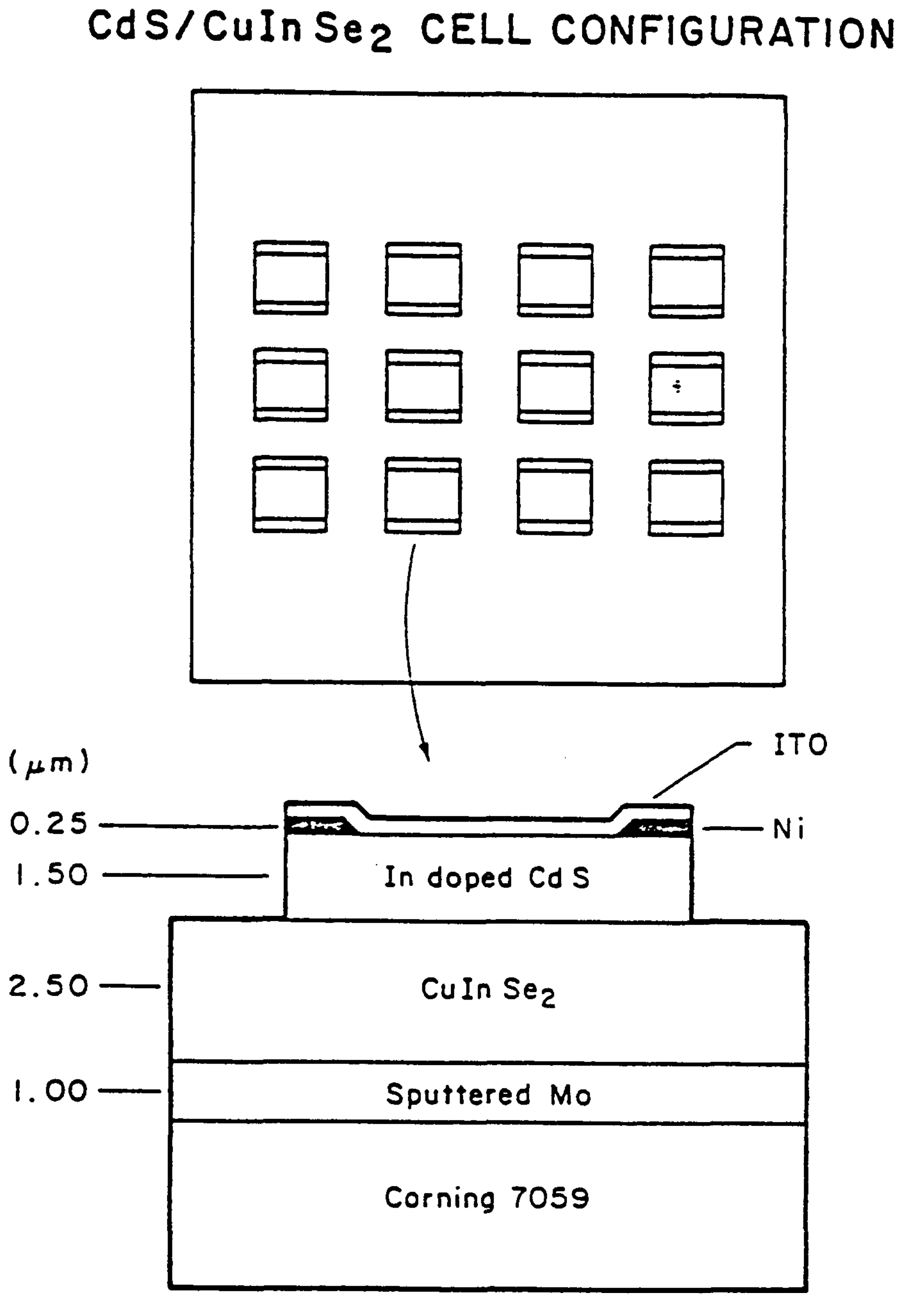

Figure 1.1 Schematic of $CuInSe_2$/CdS devices on a 2.5x2.5 cm^2 substrate.

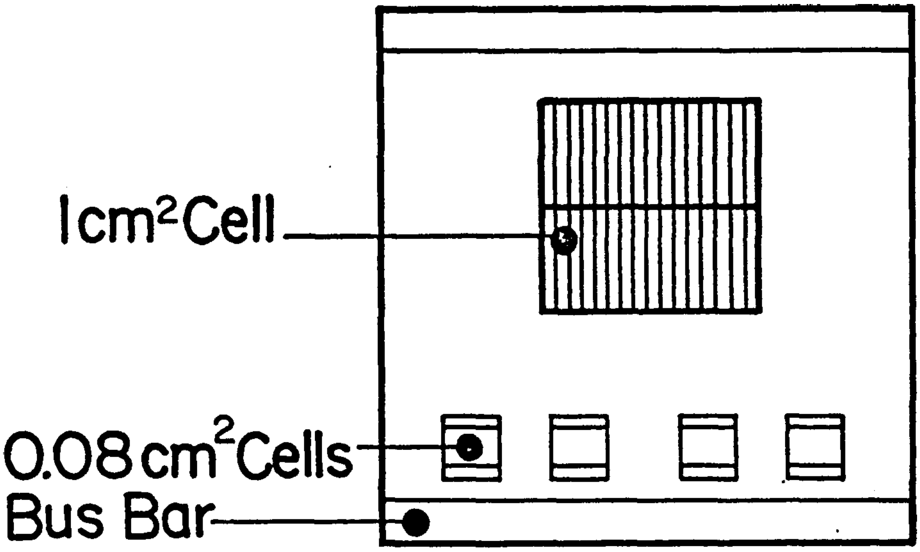

Figure 1.2 1 cm² cell configuration with 4 small area devices.

1.2 $CuInSe_2$ FILM ANALYSIS

Material studies were carried out in parallel with the cell performance testing. The $CuInSe_2$ films are characterized with respect to sheet resistance composition, structure and morphology.

Resistivity

The sheet resistance for each individual layer and the composite layer was determined using four point probe techniques. The initial layer is always p-type and highly conductive with a resistivity generally between 0.01 and 0.1Ωcm. The second layer is always highly resistive, essentially exceeding the measurement limit of our four point probe apparatus. The composite layer is somewhat more conducting than the second layer and is usually detectably p-type. The film composition for each individual layer and the composite layer is determined by energy dispersion spectrometry (EDS) relative to secondary $CuInSe_2$ film standards measured at SERI. The relative error in the measurement is estimated to be ±2% of the measured value. The results of these measurements are correlated with device results and discussed in section 1.3.

Surface Morphology

Scanning electron microscopy to monitor the surface morphology, and X-ray diffraction to characterize the crystallinity were used to characterize $CuInSe_2$ films grown at different substrate temperature combinations in hopes of decreasing the surface texture to provide a better surface for fabricating tandem cells. No major changes with substrate temperature were observed as indicated by the data in Table 1.1. In all cases the first (A) layer is highly (112) oriented and reveals a somewhat facetted surface in the SEM at x5000. The second (B) layer is much smoother and is essentially randomly oriented. The composite layer still shows some preferred orientation and is distinctly facetted. It should be noted that the individual layers are deposited on bare 7059 glass (in order to allow resistivity measurements) whereas the composite films are on 7059/Mo substrates. It is estimated that at the start of the deposition the bare 7059 pieces are about 50°C cooler than the Mo coated 7059 but that as the $CuInSe_2$ builds up the temperatures become identical.

Table 1.1

X-ray diffraction intensities and composition for $CuInSe_2$ layers deposited at various substrate temperatures.

Run	Layer	Temp.	XRD Intensity			Composition (%)		
		(°C)	(112)	(220) (204)	(116) (312)	Cu	In	Se
31576	A	275	12,600	90	60	27.6	22.6	49.8
"	B	450	300	500	30	15.6	28.6	55.8
"	C		1,050	300	180	22.6	26.3	51.1
31588	A	300	31,000	70	40	28.7	23.4	49.9
"	B	500	600	200	60	17.3	28.5	54.2
"	C		960	350	240	24.9	25.1	50.0
31580	A	300	33,000	60	40	29.7	21.8	48.5
"	B	450	390	470	60	14.8	28.9	56.3
"	C		1,200	360	200	24.3	25.3	50.4
31570	A	350	16,700	140	110	27.9	25.0	47.1
"	B	450	260	500	50	17.6	29.6	52.8
"	C		1,020	390	260	26.2	26.8	47.0

Growth Defects

Optical and SEM observations revealed that some $CuInSe_2$ layers contained a distribution of defects which were up to 10 μm in diameter and many microns high. The defects resulted in locally poor coverage by the CdS layer which in turn led to shunts. Examination of the individual Cu rich layer (A) and In rich layer (B) revealed that the defects were almost universally caused by the B-layer deposition.

A systematic study of defects on the B-layer of substrate #31649.12 was carried out using SEM and X-Ray Emission spectroscopy (EDS). Fig. 1.3A shows the micrograph of a defect surrounded by the In rich B-layer. Other defects did not show the central dark region as illustrated in Fig. 1.3B from $CuInSe_2$ film #31683.12, however similar EDS results were obtained for the two defect types. The EDS showed that the outer regions of the defects were of a higher In content than the general film and the center region was essentially In with a low Se content (~80/20). The surface of the defect was etched with Br/MeOH and H_2SO_4 with the result that the outer region of the defect then showed an increased In content. At this stage it was tentatively concluded that In droplets were being ejected from the source during the deposition of the B-layer possibly due to the increased operating temperature of the In source during the B-layer deposition. If this occurs during the early stages of the B-layer growth there would be subsequent $CuInSe_2$ overgrowth in keeping with the results of the etching experiment.

In order to test the hypothesis pure In films were deposited using a range of source In temperatures. For an operating temperature of 1045°C the In film was featureless, raising the temperature to 1065°C yielded a few small defects and at 1080°C there were many large defects. Operation of the In source was modified in two ways which in combination resulted in essentially defect free films. First the highest In source temperature used was reduced to 1065°C and the Cu source temperature re-adjusted to give the desired film composition. In addition the temperature gradient in the In source was increased with the intent of eliminating boiling within the liquid and ensuring that all evaporation took place from the free surface. This was achieved by reducing the power to the lower source heater from 50W to 20W; the upper source heater is thermostatically controlled and automatically adjusted to an increased power level to maintain the desired operating temperature. $CuInSe_2$ films grown using this new procedure, generally, had fewer defects.

A semi-quantitative measure of defect density was obtained by counting visible defects in an actual film area of 10mm^2 as seen through an optical microscope at a magnification of about X40. Using the original operating system the defect count on the second layer was as high as 200 and never less than 20; the most defect laden first layer had up to 20 defects. By keeping the Indium source temperature below 1065°C the second layers were produced essentially free of defects with <5 and frequently 0 defects in the 10mm^2 areas surveyed.

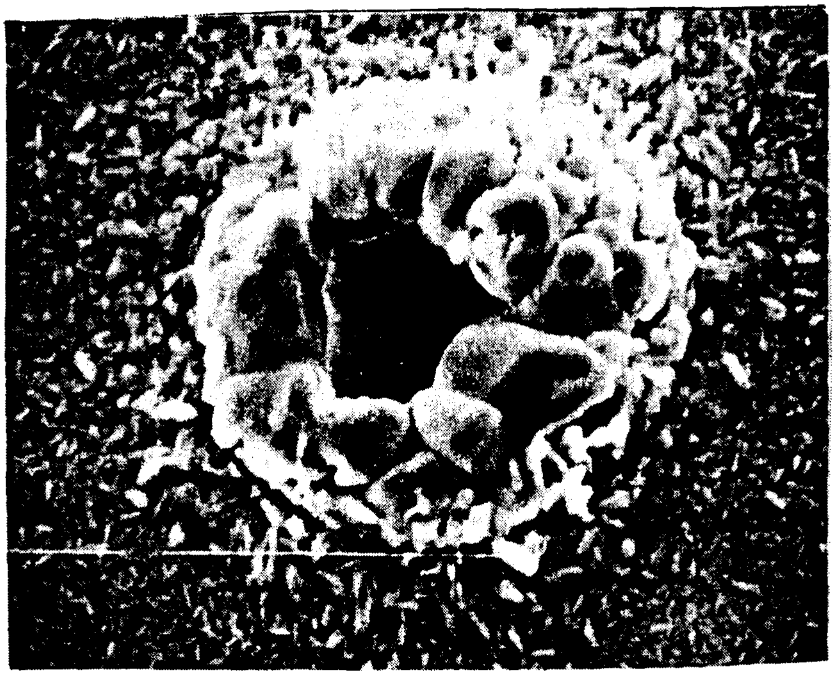

Figure 1.3A: Scanning electron micrograph of an In droplet induced defect in the second (B) layer of deposition run #31649. Magnification x 5,000, tilt 20°

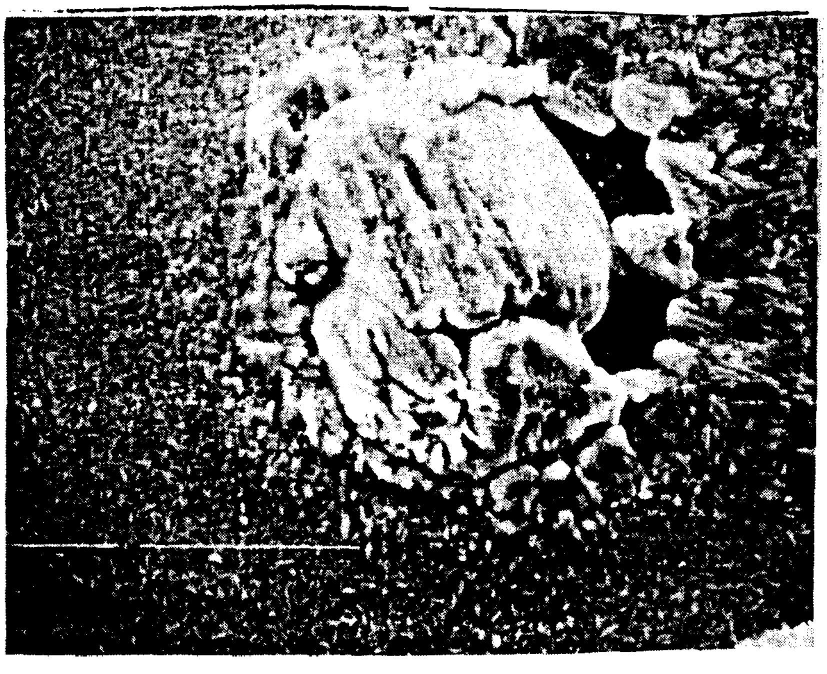

Figure 1.3B: Scanning electron micrograph of a defect in which the control bright region is essentially In-Se. Second layer from deposition #31683. Magnification x3000, tilt 20°

1.3 CELL RESULTS AND DEVICE ANALYSIS

Device performance at IEC has been measured under a simulator using 4 General Electric ELH tungsten halide bulbs. These bulbs are held at 115 V with voltage controlled d.c. power supplies. The light intensity is set at 87.5 mW/cm^2 equivalent (approximately AM1.5 direct) for single crystal silicon solar cells. Silicon cells have been used as a calibration standard because their bandgap is about midway between that of CdTe and $CuInSe_2$ (in photon flux), thereby allowing an approximate calibration for both types of single junction cells and tandem devices.

This calibration procedure has given currents for $CuInSe_2$ devices that are about 5% higher than the AM1.5 direct spectra would give. We have compensated by testing at a temperature of 32°C which lowers the voltage by a proportional amount and hence gives the correct efficiency.

Recently[4] SERI has standardized to the ASTM 86 global spectra. Changing from a direct to global spectra increases the proportion of photons in the blue region which are unusable to present $CuInSe_2$/CdS devices. Hence efficiencies are derated. Recent tests suggest that the amount is about 4% (i.e. a solar cell that measures 10% efficiency under a direct spectra would be derated to 9.5% efficiency.)

IEC and SERI are engaged in developing a set of calibration standards for $CuInSe_2$/(CdZn)S devices in order to simulate the present ASTM 86 global standard. Meanwhile, past IEC test results can be approximately compared to this standard by increasing voltages 5% since SERI measurements are made at 25°C and derating current 9%. Efficiency is hence derated by 4%.

1.3.1 I-V Test Results

Device optimization

After the final contacts are applied, the $CuInSe_2$/CdS devices on each substrate are I-V tested and their performance then optimized with 200°C air heat treatments[3]. Figure 1.4 shows the evolution of a typical high efficiency device during the optimization treatment. Initially the device shows a very "soft" or almost shorted diode characteristic which rapidly saturates in short-circuit current and more slowly in open-circuit voltage or junction "barrier height". Heat treatment times of 16-32 hours are usually required to optimize the cells. Section 1.3.2 discusses the effects of the heat treatments.

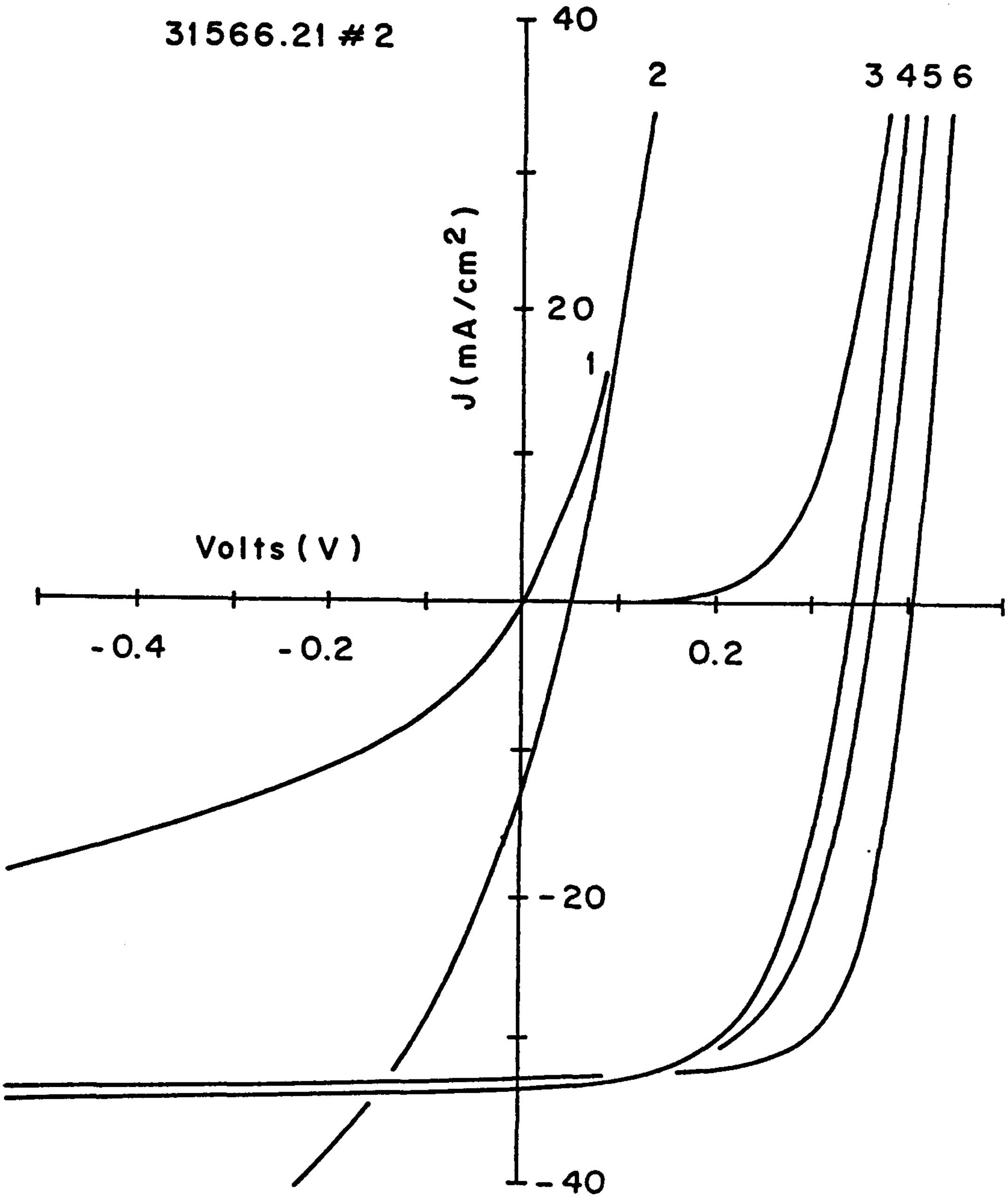

Figure 1.4: Evolution of a high efficiency $CuInSe_2/CdS$ device with heat treatment at 200°C in air.

1 cm^2 cells

1 cm^2 $CuInSe_2$ based solar cells have been made by the process described in section 1.1. The best devices have tested over 10% efficiency on IEC's simulator. The I-V characteristics of the dozen that have been tested of over 9% efficiency are shown in Table 1.2. Most of the 1 cm^2 cells will be used for simulator calibration and efficiency comparisons with other laboratories.

Table 1.2
Best 1 cm^2 $CuInSe_2$ Cell Results

$CuInSe_2$ piece #	Eff	$J_{sc}{}^{+}$	V_{oc}	FF	test date
31741-22	10.48	32.2	0.425	66.7	10Jul86
31743-22	10.37	33.6	0.409	66.0	18Jul86
31739-23	10.08	31.8	0.420	66.1	18Jul86
31739-21	9.67	30.5	0.427	64.9	10Jul86
31749-32	9.64	31.6	0.405	65.9	4Nov86
31740-22	9.59	34.7	0.419	57.8	8Sep86
31758-22	9.41	32.0	0.401	64.1	4Nov86
31746-21	9.37	30.1	0.427	63.9	12Aug86
31754-22	9.36	32.2	0.386	65.7	15Oct86
31740-21	9.22	30.9	0.407	64.1	8Oct86
31699-22	9.05	30.7	0.408	63.3	18Apr86
31708-22	9.02	31.0	0.405	62.8	29Apr86

+ELH simulation at 87.5 mW/cm^2; cell temperature: 32°C

3x3 mm^2 cells

The $CuInSe_2$ program at IEC has concentrated on producing a 3x4 matrix (see Figure 1.1) of 12 small cells on a 2.5 cm square piece of $CuInSe_2$ material. This has allowed us to check uniformity and yield of all the processes involved in making the devices as well as providing a convenient sized device for detailed analysis. The performances of these devices are essentially active area performances because of their construction. Table 1.3 shows the I-V results of the best cell from 11 different $CuInSe_2$ evaporations that have produced cells with efficiencies over 10.5%.

Table 1.3
Best I-V tests for 3x3 mm^2 $CuInSe_2$ cells on separate $CuInSe_2$ evaporation runs

$CuInSe_2$ piece #	cell #	Eff	$J_{sc}$$^+$	V_{oc}	FF	test date
31580-22	305	11.20	36.1	0.426	63.7	3Jul85
31539-22	305	11.00	34.9	0.420	65.7	1Apr85
31553-21	303	10.90	33.9	0.421	67.0	7May85
31556-21	304	10.84	33.5	0.417	68.0	7May85
31569-22	312	10.82	35.1	0.418	64.4	26Jun85
31544-21	302	10.79	33.0	0.421	68.0	30Apr85
31566-22	308	10.73	33.5	0.422	66.4	10Jun85
31755-21	312	10.67	34.6	0.406	66.5	13Jan87
31550-33	310	10.60	33.3	0.428	65.2	21Jun85
31573-21	305	10.54	32.2	0.417	68.7	13Jun85
31565-11	312	10.51	35.1	0.401	65.4	31May85

+ELH simulation at 87.5 mW/cm^2; cell temperature: 32°C

Double and single tab measurements

The loss in fill factor FF in $CuInSe_2$/(CdZn)S cells has been quantified by double and single tab I-V measurements. Such measurements require a cell structure with two separate bus bars or tabs at opposite ends of the cell. Testing a cell of this type with each tab individually and with both tabs connected together, gives a set of I-V characteristics that differ only in effective tab spacing. This cell structure gives a three terminal device which allows the direct measurement of the sheet resistance of the CdS/ITO top layer. The fill factor loss due to the CdS/ITO can be calculated and removed from the measured fill factor, leaving the junction of $CuInSe_2$ losses. A detailed description of the technique can be found in Ref. [5]. The loss in FF from the one-tab/two-tab measurements is given by (1).

$$\Delta FF_{(1+2)} = \frac{FF_{(1+2)} - FF_{(1\ \text{or}\ 2)}}{3} \qquad (1)$$

where (1+2) designates the FF measured with both tabs connected and (1 or 2) designates the FF measured with one of the tabs connected.

Table 1.4 shows the best values for double and single tab I-V measurements for a selected number of $CuInSe_2$ cells. The FF and thus the efficiency are the two parameters affected from these measurements. For example, piece #31743.22 using equation (1) gives a $\Delta FF \simeq 3.5\%$ which means a spreading resistance FF loss approximately 3.5%, thus the maximum FF at zero grid spacing is 68%.

Table 1.4 also shows the results of two special pieces #31756.212 and #31756.211 which had thick (1.7 μm) In-doped CdS with and without ITO respectively.

The results show that Δ FF (1+2) without ITO $\simeq$ 3.5%
Δ FF (1+2) with ITO $\simeq$ 2.0%

The limiting fill factor losses with and without ITO were ~2.0% and ~3.5% respectively. The difference between the two FF losses is too small to draw any conclusions.

Table 1.4
Best values for double and single tab I-V measurements

CuInSe2 Piece #	Tab Type	# of cells tested	Max.Eff. (%)	Max.FF. (%)	Max.Jsc. (mA/cm²)	Max.Voc. (V)	
31354-11	single	12	7.44	57.94	29.27	0.3896	
31354-11	single	12	7.53	57.10	30.51	0.3873	
31354-11	double	12	8.18	59.65	31.59	0.3914	
31355-32	single	5	7.90	55.86	34.54	0.3874	
31355-32	single	5	7.90	54.60	34.54	0.3849	
31355-32	double	5	8.85	59.64	34.77	0.3872	
31569-11	single	12	9.34	60.79	32.33	0.4171	
31569-11	single	12	9.40	61.20	32.34	0.4174	
31569-11	double	12	10.15	66.66	32.28	0.4169	
31699-21	single	12	8.69	57.59	33.27	0.4108	
31699-21	single	12	8.68	57.35	33.44	0.4098	
31699-21	double	12	10.19	65.29	34.02	0.4078	
31706-33	single	4	8.22	59.33	30.18	0.4017	
31706-33	single	4	8.00	57.46	30.21	0.4034	
31706-33	double	4	9.11	64.74	30.45	0.4045	
31739-23	single	4	9.31	59.93	33.85	0.4208	
31739-23	single	4	9.02	58.56	33.75	0.4205	
31739-23	double	4	10.25	66.23	33.18	0.4191	
31743-22	single	4	8.69	54.89	35.50	0.3984	
31743-22	single	4	8.60	53.74	35.59	0.4021	
31743-22	double	4	10.41	64.80	35.53	0.4048	
31756-211	single	6	7.88	54.06	32.01	0.4088	NO
31756-211	single	6	7.89	54.38	31.99	0.4068	ITO
31756-211	double	6	9.40	64.15	32.19	0.4070	
31756-212	single	3	9.10	60.98	31.82	0.4169	
31756-212	single	3	9.16	61.07	31.79	0.4168	ITO
31756-212	double	3	9.87	66.61	31.93	0.4165	

$CuInSe_2$ substrate material

Most of the $CuInSe_2$ devices made at IEC have used 7059 glass as a substrate. During the development of the devices, however, three other substrates namely Soda Lime (Kodak Microscope Slides), Soda Lime* (window glass), and Alumina were also used. Table 1.5 shows the best I-V results for the different substrates used to make the $CuInSe_2$ devices. In each case the substrate tried was compared with the currently used 7059 glass. Cells with $\eta>8\%$ and FF>60% have been made using both soda lime and alumina substrates showing that the insensitivity of the device performance to substrate material. This result is particularly significant since soda lime glass is inexpensive and would be ideal for large scale production.

Table 1.5
I-V results for the various substrates used
for CuInSe2 based devices

$CuInSe_2$ Piece #	Substrate	Highest eff (%)	J_{sc}^{+} (mA/cm²)	V_{oc} (V)	FF (%)
31393-23	7059 Glass	7.91	29.90	0.3866	61.04
31394-21	7059 Glass	0.61	12.62	0.1496	31.64
31395-21	7059 Glass	8.42	29.35	0.4000	63.06
31395-22	Soda Lime	8.95	29.97	0.4109	64.95
31396-21	7059 Glass	8.36	29.83	0.3973	62.44
31396-22	Soda Lime	7.74	28.11	0.4006	63.43
31396-32	7059 Glass	7.58	32.17	0.3940	57.53
31397-21	7059 Glass	7.50	27.13	0.3904	63.08
31397-22	Soda Lime	7.74	29.41	0.3862	60.98
31398-21	7059 Glass	7.56	27.74	0.3862	62.68
31398-22	Soda Lime	7.22	28.62	0.3778	58.44
31401-22	Soda Lime	7.71	32.69	0.3712	56.07
31401-23	Soda Lime	7.79	32.78	0.3776	55.93
31402-21	7059 Glass	7.53	32.63	0.3931	54.38
31556-11	7059 Glass	8.41	31.88	0.4110	56.14
31556-21	7059 Glass	10.84	34.80	0.4198	68.86
31556-223	7059 Glass	9.64	34.13	0.3873	63.79
31556-33	Alumina	8.65	34.05	0.3670	62.20
31560-21	7059 Glass	8.31	34.16	0.3710	60.74
31624-21	7059 Glass	7.98	33.65	0.3670	57.16
31624-22	Soda Lime*	7.96	33.78	0.3604	59.41
31625-21	7059 Glass	7.28	32.89	0.3427	56.52
31625-22	Soda Lime*	7.10	31.96	0.3637	55.90
31630-222	Soda Lime*	9.12	33.29	0.3922	61.30
31639-222	7059 Glass	9.31	33.57	0.3882	63.16

+ELH simulation at 87.5 mW/cm²; cell temperature: 32°C

Metal contacts to $CuInSe_2$

In order to achieve a $CuInSe_2$/(CdZn)S solar cell with low series resistance losses, it is necessary to provide a low resistance ohmic back contact to the $CuInSe_2$. Earlier work done at IEC on ohmic back contacts for $CuInSe_2$[1] had investigated Ni, Au, as well as Mo as possible back contact metals. The high work functions of those metals[6] suggested that they would make a low resistance contact to p-type $CuInSe_2$. The conclusion of that investigation was that all three metals (Au, Mo, Ni) appeared to give a low resistance back contact to p-type $CuInSe_2$ when applied properly. Mo was selected based on cost and ease of deposition on to the substrate. The back contact was further investigated by depositing a thin Pt layer on selected Mo substrates. Table 1.6 shows the I-V results for standard Mo and Mo/Pt contact to $CuInSe_2$. Piece numbers 31360 to 31372 have a Pt layer of 5000A while Piece numbers 31372 to 31378 have a 500A Pt layer. Within the limited amount of data, some cells with Mo/Pt back contacts were made with an efficiency comparable to Mo alone ($\eta>7\%$). Due to the scatter in the results, it is difficult to make a firm conclusion about Pt as a contact, but the preliminary results suggests that there is no difference between Mo and Pt. Further, the deposition of $CuInSe_2$ on these back contacts takes place in a rich Se atmosphere and reaction between Se and Pt may occur resulting in the disappearance of the Pt layer.

Table 1.6

I-V results for standard Mo and Mo/Pt contact to $CuInSe_2$

$CuInSe_2$ Piece #	Substrate	Highest Eff (%)	$J_{sc}{}^{+}$ (mA/cm^2)	V_{oc} (%)	FF (%)
31361-11	Mo	7.18	25.87	0.3827	64.87
31362-23	Mo/Pt	6.39	26.89	0.3567	61.87
31362-33	Mo	6.56	27.19	0.3793	
31373-11	Mo	6.14	26.40	0.3552	59.09
31373-22	Mo/Pt	7.24	28.89	0.3688	61.72
31373-23	Mo/Pt	6.00	29.16	0.3617	51.66
31374-11	Mo	7.20	28.38	0.3809	60.25
31374-23	Mo/Pt	5.97	29.53	0.3517	50.72
31376-11	Mo	7.09	26.85	0.3933	60.27
31377-11	Mo	7.73	29.20	0.3927	59.76
31377-22	Mo/Pt	6.63	27.01	0.3558	62.04
31378-21	Mo/Pt	6.27	30.48	0.3483	56.42

+ELH simulation at 87.5 mW/cm^2; cell temperature: 32°C

Area Uniformity of $CuInSe_2$ Films

The uniformity of the $CuInSe_2$ films over 66 cm^2 substrate area was evaluated as an initial step toward making large area (>25cm^2) $CuInSe_2$/CdS cells. The approach was to use small area device performance as a measure of uniformity. A data base of 785 2.5x2.5 cm^2 $CuInSe_2$ samples each with 12 0.3x0.3 cm^2 $CuInSe_2$/CdS cells were analyzed and in addition, samples from a single $CuInSe_2$ deposition were processed simultaneously into cells to directly examine uniformity. Figure 1.5 shows the diagram of the substrate area in the $CuInSe_2$ evaporator, with each piece location designated by a two digit number. Table 1.7 shows the best I-V test parameters (η, J_{sc}, V_{oc}, FF) as a function of piece location in the $CuInSe_2$ evaporator divided into percentiles. Piece locations 12 and 13 were reserved for material analysis of the $CuInSe_2$ (hot probe, resistivity, EDAX) while piece location 31 was used to control the substrate temperature. As can be seen from the Table 1.7, there is no correlation with the piece location in the evaporator (Figure 1.5) and the device parameters for the maximum to the 75th percentile. Also included in Table 1.7 are the results from $CuInSe_2$ run #31755 where all $CuInSe_2$ samples were processed together. These results further demonstrate the $CuInSe_2$ uniformity. This lead us to conclude that $CuInSe_2$ is uniform with respect to device parameters over at least 66 cm^2 area of deposition.

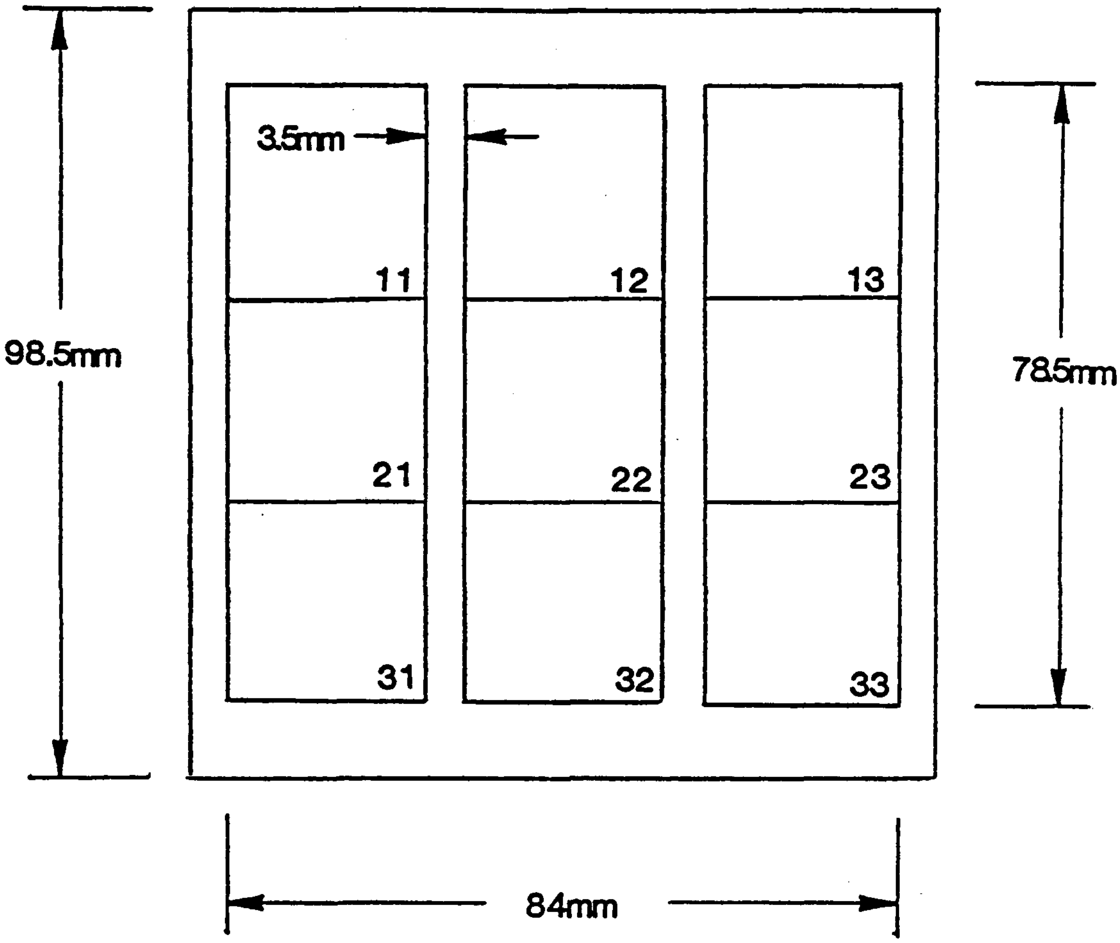

Figure 1.5. Substrate area in the $CuInSe_2$ evaporator with each piece location designated by a two digit number.

Table 1.7

Best I-V test parameters as a function of piece location in the $CuInSe_2$ evaporator (total of 551 12-cell pieces)

Location $CuInSe_2$ Evaporator	No. of Pieces	Max.	95th %tile	90th %tile	75th %tile	Median	Cell #31755
			Efficiency				
11	106	10.51	9.68	9.50	8.45	7.23	10.3
21	148	10.90	10.40	9.99	8.83	7.14	10.7
22	122	11.20	10.30	9.94	8.91	7.11	9.3
23	87	10.29	9.66	9.20	7.91	6.49	10.3
32	19	10.07	10.07	10.04	7.18	6.10	10.1
33	69	10.60	10.20	9.51	8.25	6.27	10.2
			J_{sc}+				
11	106	35.8	34.3	34.0	32.6	31.3	33.1
21	148	36.4	35.0	34.1	33.3	31.7	34.8
22	122	38.0	35.9	34.9	33.8	31.6	35.8
23	87	35.8	35.0	34.3	32.4	30.6	34.3
32	19	34.1	34.1	33.9	32.8	31.5	34.1
33	69	35.5	34.1	33.6	32.2	30.4	32.6
			V_{oc}				
11	106	0.417	0.412	.409	0.394	0.381	0.415
21	148	0.433	0.420	.412	0.398	0.383	0.412
22	122	0.439	0.424	.412	0.397	0.377	0.378
23	87	0.431	0.418	.412	0.402	0.371	0.409
32	19	0.413	0.413	.398	0.393	0.360	0.318
33	69	0.428	0.418	.410	0.393	0.363	0.418
			Fill Factor				
11	106	67.3	65.5	64.7	62.2	59.1	67.3
21	148	68.9	66.8	65.5	62.4	58.0	66.5
22	122	68.1	66.8	65.2	62.5	57.7	61.6
23	87	67.2	65.2	64.2	60.9	54.4	67.2
32	19	67.4	67.4	65.8	56.5	53.8	65.8
33	69	68.2	66.4	65.2	62.5	51.5	66.8

+ELH simulation at 87.5 mW/cm^2; cell temperature: 32°C

$CuInSe_2$ composition vs. device performance

The film composition for each individual layer of the two layer $CuInSe_2$ film and the composite layer has been determined by energy dispersion spectrometry (EDS) on 389 separate $CuInSe_2$ evaporation as discussed in section 1.2. Comparison of film composition with device performance has shown little correlation over the range of composition produced at IEC. This is true with respect to either of the single layers as well as the composite $CuInSe_2$ film.

Tables 1.8a-d show the best device results vs. film composition of the final composite layer. As can be seen, cells with $\eta>10\%$ have been made with $CuInSe_2$ film compositions with Cu from 23% to 27% and In from 25% to 28%. The reason for this may be due to IEC's approach of adjusting the $CuInSe_2$ resistivity with oxidizing and reducing heat treatments in the final optimization of the device. (see page section 1.3.2).

Table 1.8(a)
Best efficiency device performance vs. CuInSe$_2$ composition for 389 CuInSe$_2$ evaporations

	% IN											
	<25		25		26		27		28		>28	
	EFF		EFF		EFF		EFF		EFF		EFF	
%CU	*	MAX	*	BEST	*	BEST	*	BEST	*	BEST	*	BEST
<21					1	7.5	2	6.8			2	5.2
21					2	6.7	8	7.9	1	8.0		
22					7	9.6	7	9.4	5	7.9		
23			1	9.9	25	10.8	16	9.9	4	7.8	3	7.1
24	1	8.5	12	11.2	32	10.9	22	10.4	7	7.8		
25			21	11.0	43	10.8	23	10.7	8	10.3		
26	4	9.9	22	9.8	33	10.7	23	10.8	5	10.3		
27	1	5.0	8	7.7	19	10.5	6	8.7	1	6.3		
28			5	5.7	6	6.8	1	7.1				
>28	1	0.0			1	0.3						

* # of runs

Table 1.8(b)

Best J_{sc} device performance vs. $CuInSe_2$ composition for 389 $CuInSe_2$ evaporations

	% IN											
	<25		25		26		27		28		>28	
	JSC		JSC		JSC		JSC		JSC		JSC	
	*	MAX	*	BEST	*	BEST	*	BEST	*	BEST	*	BEST
%CU												
<21					1	31.1	2	33.6			2	24.3
21					2	31.3	8	33.8	1	33.2		
22					7	34.1	7	32.8	5	33.8		
23			1	33.0	25	34.9	16	33.6	4	34.0	3	28.0
24	1	31.5	12	36.5	32	34.8	22	35.3	7	32.5		
25			21	36.4	43	36.0	23	35.7	8	34.2		
26	4	33.7	22	35.6	33	35.4	23	38.0	5	35.4		
27	1	31.4	8	31.5	19	35.8	6	35.9	1	28.6		
28			5	32.6	6	35.8	1	32.1				
>28	1	0.0			1	8.6						

* # OF RUNS

Table 1.8(c)

Best V_{oc} device performance vs. $CuInSe_2$ composition for 389 $CuInSe_2$ evaporations

	%IN											
	<25		25		26		27		28		>28	
	VOC		VOC		VOC		VOC		VOC		VOC	
	*	MAX	*	BEST	*	BEST	*	BEST	*	BEST	*	BEST
%CU												
<21					1	.374	2	.369			2	.346
21					2	.364	8	.382	1	.384		
22					7	.398	7	.394	5	.392		
23			1	.411	25	.420	16	.423	4	.391	3	.371
24	1	.392	12	.429	32	.425	22	.429	7	.422		
25			21	.433	43	.428	23	.428	8	.433		
26	4	.409	22	.422	33	.419	23	.439	5	.431		
27	1	.284	8	.393	19	.408	6	.395	1	.352		
28			5	.380	6	.370	1	.363				
>28	1	.000			1	.129						

* # OF RUNS

Table 1.8(d)

Best FF device performance vs. CuInSe$_2$ composition for 389 CuInSe$_2$ evaporations

	% IN											
	<25		25		26		27		28		>28	
	FF		FF		FF		FF		FF		FF	
%CU	*	BEST	*	BEST	*	BEST	*	BEST	*	BEST	*	BEST
<21					1	58.1	2	58.4			2	54.9
21					2	57.3	8	61.0	1	56.2		
22					7	65.5	7	65.7	5	65.7		
23			1	67.2	25	68.5	16	65.2	4	56.5	3	61.9
24	1	60.5	12	65.1	32	67.4	22	65.7	7	64.6		
25			21	65.8	43	68.9	23	68.7	8	63.1		
26	4	64.9	22	66.6	33	66.4	23	68.1	5	61.8		
27	1	51.6	8	61.9	19	65.4	6	61.3	1	56.5		
28			5	42.8	6	56.9	1	55.6				
>28	1	25.0			1	26.4						

* # OF RUNS

Device Properties vs. CdS thickness

The effect of the thickness of the CdS on the performance of $CuInSe_2$/CdS devices has been investigated. Table 1.9 shows the I-V parameters of the highest efficiency thickness of CdS layer. The best efficiency 3x3 mm² devices were made at an In-doped CdS thickness > 1μm, and the higher efficiency is due to higher fill factor. It is interpreted as an equivalent series resistance effect. J_{sc} does not seem to be affected by CdS thickness in this range. Further examination requires investigation of the role of the ITO transparent contact and possible improvements in that direction.

Table 1.9
Best efficiency I-V parameters vs. thickness of CdS layer (from .5 to 2 microns) on $CuInSe_2$ devices

CdS Thickness (microns)	# of runs	Best Eff (%)	FF (%)	J_{sc}+ (mA/cm²)	V_{oc} (V)	$CuInSe_2$ Piece #	# of $CuInSe_2$ pieces run
0.5	11	7.18	50.4	34.34	0.3770	31438-11	39
0.6	9	9.61	64.1	32.77	0.4212	31386-23	32
0.7	15	7.96	56.2	33.19	0.3839	31407-21	50
0.8	16	8.87	51.8	35.71	0.4192	31452-33	55
0.9	2	8.85	59.6	34.77	0.3872	31355-32	8
1.0	2	8.82	63.2	31.54	0.3921	31726-11	8
1.1	3	10.60	66.4	35.71	0.4181	31569-21	12
1.2	6	10.18	62.2	35.99	0.4118	31386-22	21
1.3	8	11.20	63.9	36.48	0.4286	31580-22	35
1.4	12	10.82	64.4	38.03	0.4184	31569-22	46
1.5	19	10.79	68.5	33.01	0.4205	31544-21	70
1.6	17	11.00	65.8	34.91	0.4246	31539-22	50
1.7	15	10.90	66.9	33.85	0.4207	31553-21	47
1.8	26	10.51	65.3	35.75	0.4078	31565-11	63
1.9	22	10.54	68.7	32.51	0.4180	31573-21	70
2.0	7	10.23	68.2	32.07	0.4189	31553-33	13

+ELH simulation at 87.5 mW/cm²; cell temperature 32°C

CdS double layer

The Boeing $CuInSe_2$/CdS cell has a double CdS layer: An undoped CdS layer is deposited initially on $CuInSe_2$ followed by In-doped CdS. IEC switched to a single CdS layer for simplicity. Although the Dark Spectral Response was found to be different for these two types of devices[7], they were found to be the same under simulated AM1 illumination. Table 1.10 shows comparison I-V results of double and single layer evaporations of CdS on $CuInSe_2$ devices made at IEC. The performance parameters show essentially no difference between single or double layer CdS. The conclusion that can be drawn from these results is that a single CdS layer should be more advantageous than the double CdS layer because it is simpler to use and requires less processing control.

Table 1.10 Comparison of double and single layer evaporations of CdS on $CuInSe_2$ devices

CdS run	double or single	$CuInSe_2$ piece #	Best Eff (%)	FF (%)	J_{sc}+ (mA/cm^2)	V_{oc} (V)	CdS thickness microns	CdS R sheet (ohm/sq)	Hrs H.T.
10835	dbl	31320-21	6.54	57.30	31.26	.3273	6.9	7.3	32
10847	sing	31349-11	5.96	60.86	24.28	.3689	7.3	3.6	18
10852	dbl	31359-23	5.33	57.02	29.88	.3189	5.3	11.0	28
10858	sing	31370-11	6.87	60.84	27.37	.3731	4.9	3.5	10
21875	sing	31314-22	7.97	60.94	30.46	.3758	6.1	2.7	38
21879	dbl	31316-11	6.74	61.14	26.95	.3745	6.1	4.5	16
21883	dbl	31322-11	7.21	64.62	26.70	.3737	6.5	5.0	24
21885	dbl	31324-33	7.49	62.68	27.46	.3809	6.1	8.1	12
21888	dbl	31327-22	6.63	60.82	27.60	.3530	6.9	4.1	12
21891	dbl	31329-33	6.77	61.35	27.69	.3631	6.4	3.6	8
21895	dbl	31331-21	8.18	63.49	30.05	.3833	7.2	4.5	8
21897	dbl	31336-22	7.89	64.79	28.50	.3832	6.7	3.3	4
21900	dbl	31338-22	7.14	60.94	28.26	.3645	6.8	4.1	16
21902	dbl	31341-22	6.75	57.98	28.37	.3629	6.4	3.8	8
21905	sing	31344-11	3.86	59.08	20.76	.3026	5.6	2.8	10
21910	dbl	31353-22	7.45	64.60	26.68	.3848	6.5	3.1	8
21914	dbl	31354-22	7.03	63.85	25.31	.3845	5.7	4.2	23
21917	sing	31356-22	7.93	61.74	29.18	.3913	5.3	2.6	36
21921	dbl	31361-11	7.18	64.87	25.87	.3827	4.8	3.9	8
21922	dbl	31364-11	7.25	62.50	27.19	.3808	4.9	4.2	24
21923	dbl	31365-11	7.46	58.97	29.23	.3879	4.8	3.9	16
21924	dbl	31366-11	5.60	51.14	25.96	.3690	5.1	4.1	24
21927	dbl	31368-11	6.58	61.86	27.39	.3804	4.8	4.5	10
21928	sing	31369-11	6.21	58.41	26.41	.3702	4.6	1.4	20
21929	dbl	31371-11	7.04	62.63	26.48	.3723	4.5	3.8	20
21930	dbl	31372-32	3.11	50.72	22.27	.2646	4.5	4.7	none
21932	dbl	31373-22	7.24	61.72	28.89	.3688	4.8	4.0	26
21934	dbl	31374-21	5.50	62.24	23.08	.3484	4.9	4.2	8
21936	dbl	31377-11	7.73	59.76	29.20	.3927	4.7	3.9	8
21946	dbl	31382-21	8.01	60.67	30.41	.3864	5.2	2.7	8
21947	dbl	31386-21	8.35	65.55	28.03	.4105	4.7	3.3	14
21949	sing	31388-21	6.35	62.87	25.16	.3748	5.0	1.9	16
21950	sing	31389-21	6.74	59.98	26.28	.3748	5.1	1.9	17
21951	sing	31390-21	6.80	62.08	26.58	.3723	4.9	2.0	14
21952	sing	31391-21	5.06	56.80	23.67	.3374	5.4	1.9	22
21954	sing	31394-22	2.86	44.61	18.52	.3050	4.8	2.0	none
21956	sing	31395-22	8.95	64.95	29.97	.4109	4.7	2.0	8
21957	sing	31393-23	7.91	61.04	29.90	.3866	4.6	1.9	16
21958	sing	31397-22	7.74	60.98	29.41	.3862	7.6	1.9	8

+ELH simulation at 87.5 mW/cm^2; cell temperature 32°C

1.3.2 Device analysis and performance with respect to oxidizing and reducing heat treatments

The influence of air (oxidation) and hydrogen (reduction) heat treatment cycles on the performance of high efficiency $CuInSe_2$/CdS devices and the resistivity of the $CuInSe_2$ films has been investigated. Current-voltage (I-V) characteristics as a function of temperature and light intensity as well as spectral response measurements are reported. These results will be discussed in terms of the observed changes in $CuInSe_2$ resistivity as a result of the oxidation/reduction treatments. In this section the appropriate band structure of the heterojunction and the position of the Fermi level under the states of oxidation and reduction is also considered.

Current-voltage measurements

Figure 1.6 shows the development of the dark and light I-V characteristics of a device reduced in hydrogen and subsequently oxidized by air heat treatments. The dark I-V curve of a reduced device shows highly resistive behavior; the light I-V shows a low open-circuit voltage V_{oc} and a significant cross-over of the light-dark IV's suggesting a much higher resistivity. It is one of the few cases reported where the superposition principle failed to such a degree.

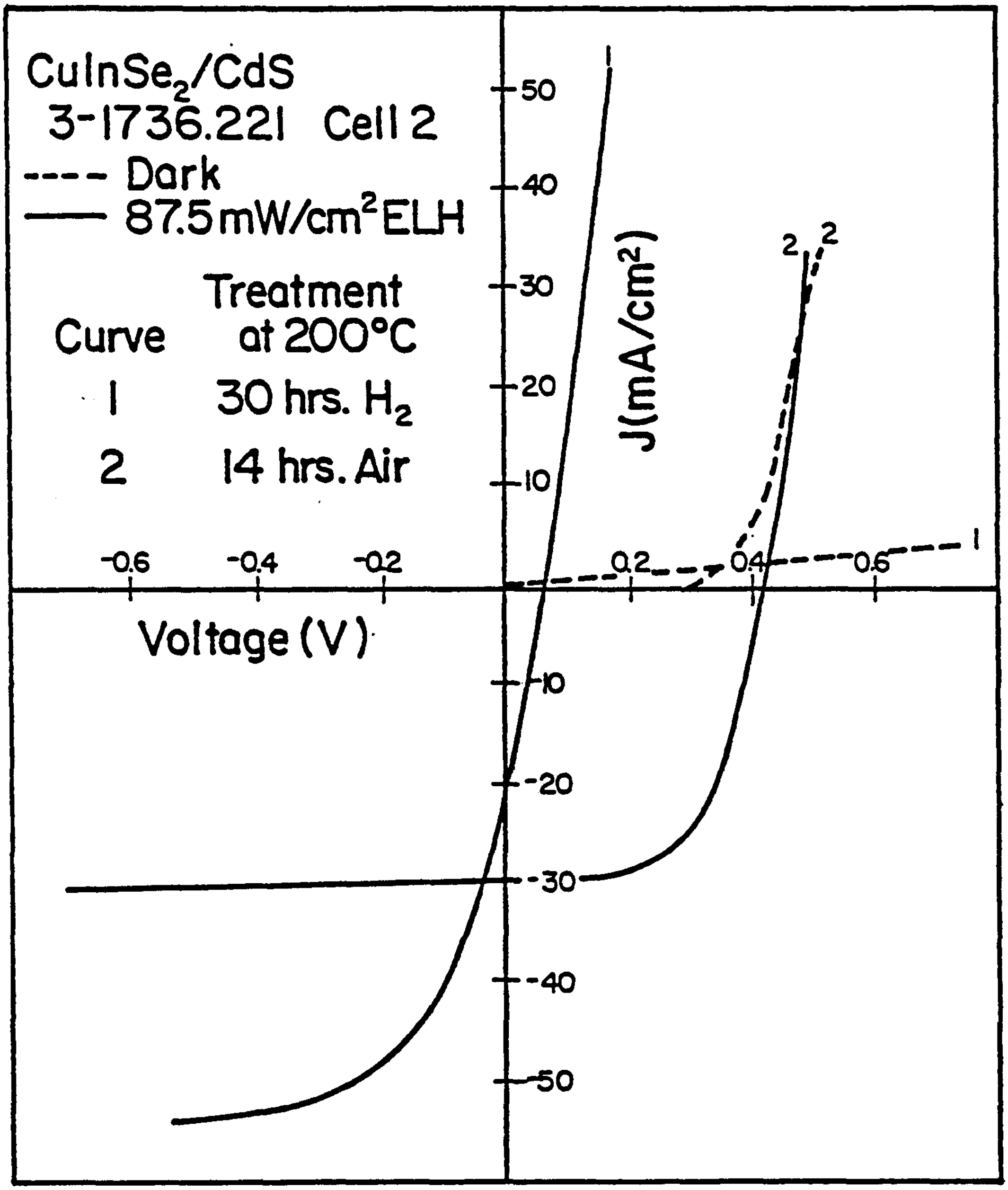

Figure 1.6: Current-voltage curves of a $CuInSe_2$/CdS device submitted to reducing/oxidizing treatments

The low V_{oc} in the reduced device is a direct consequence of a lower barrier height ϕ caused by the increase in resistivity of the CuInSe$_2$ which shifts the Fermi-level towards the middle of the gap as discussed below. Significant reduction of ϕ in highly reduced devices results in large increases in the reverse saturation current J_o which can be of the same order as the photocurrent, J_L. Thus the large apparent reverse bias photocurrents J_{LA} observed in strongly reduced devices is the sum of J_L and J_o ($J_{LA}=J_L+J_o$) with $J_L \simeq J_{sc}$. The approximation $J_o<<J_L$ in the diode equation is no longer valid where

$$J=J_L - J_o [\exp(a(V+RJ)) -1] - (V+RJ)G \qquad (2)$$

and $a = \dfrac{q}{AkT}$

with the different symbols having their usual meaning.

Table 1.11 shows the performance parameters of a CuInSe$_2$/CdS device submitted to oxidation/reduction heat treatment cycles. Virtually complete reversibility in performance has been observed. During the oxidation/reduction heat treatment cycles some of the devices were submitted to a total of more than 150 hours at 200°C treatments with virtually no degradation in performance. It shows the ability of these devices to withstand extreme operating conditions for a prolonged length of time.

Table 1.11

Piece #31750.11 Cell #4
Initial Treatment Oxidizing in Air

Accumulated Time (hrs)	Ambient	V_{oc} (V)	J_{sc}^{+} (mA/cm^2)	FF (%)	Eff (%)
16	Air	0.40	31.2	63.3	8.9
32	Air	0.40	31.6	63.0	9.2
48	Air	0.41	31.6	63.1	9.3
40	H_2	0.14	31.1	36.7	1.9
16	Air	0.41	31.2	65.0	9.6
16	H_2	0.14	28.9	30.7	1.4
6	Air	0.41	31.2	63.6	9.3

+ELH simulation at 87.5 mW/cm^2; cell temperature: 32°C

Barrier height measurements

Figure 1.7 shows plots of V_{oc} versus temperature for a device submitted to different heat treatments. Curve 1 was obtained for an oxidized device while plots 2 and 3 were obtained during two subsequent hydrogen heat treatments. Table 1.12 summarizes the results obtained for ϕ and V_{oc} during an oxidation/reduction cycle. These results indicate that the change in barrier height $\Delta \phi$ is proportional to the change in open-circuit voltage ΔV_{oc}. Subsequent air heat treatments restore ϕ to its original value.

From equation (2) assuming G $\simeq$ o, one can obtain V_{oc} in the form

$$V_{oc} = \frac{AkT}{q} \ln \frac{(J_L+J_o)}{J_o} \qquad (3)$$

separating the log form yields,

$$V_{oc} = \frac{AkT}{q} \left[\ln\frac{(J_L)}{J_o} + \ln \frac{(1+J_o)}{J_L} \right] \qquad (4)$$

The reverse saturation J_o is given by

$$J_o = J_{oo} \exp \left(- \frac{q\phi}{AkT} \right) \qquad (5)$$

The second term in equation (4) shows the contribution of J_o when it is of the same order as J_L. The fact that $\Delta \phi$ is found to be proportional to V_{oc} may suggest that band-to-band recombination is the dominant conduction loss mechanism. In such a case at the Richardson constant limit we have

$$J_{oo} = A^{*}T^{2} = 2.25\times10^{9} \text{ mA/cm}^{2} \text{ at } 300 \text{ k}$$

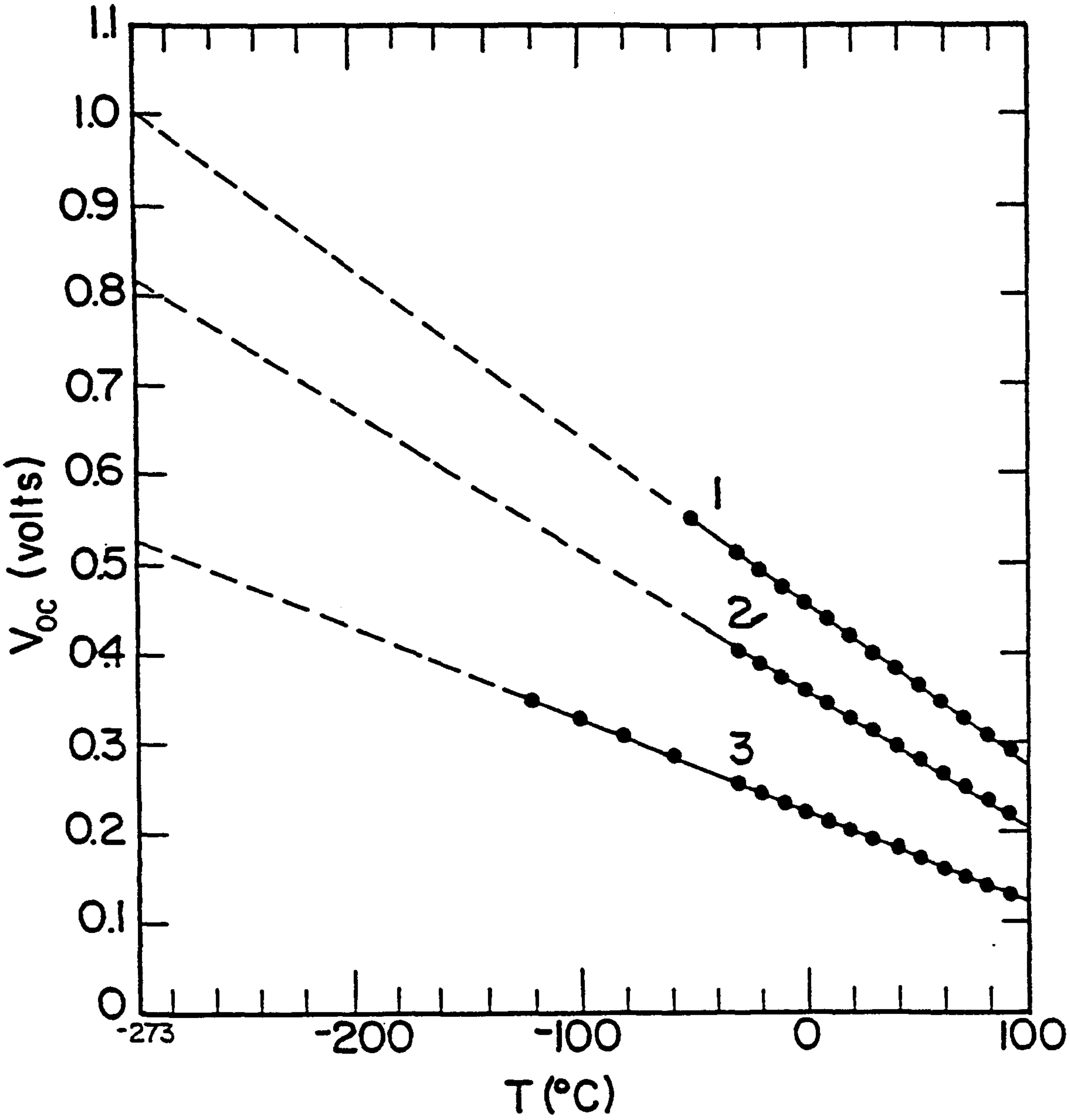

Figure 1.7 V_{oc} versus temperature curves for a $CuInSe_2$/CdS cell **(31756.11) after various heat treatments.** 1. 48 hours/200°C/Air 2. 4 hours/200°C/H_2 3. 8 hours/200°C/H_2

Table 1.12

Summary of ø and V_{oc} during an oxidational reduction heat treatment cycle

Piece #31756.11 Cell #4

Heat treatment Time (hrs)	Ambient	V_{oc} (volts) at 32°C	ø (eV)
48	Air	0.41	1.00 ± 0.02
4	H_2	0.33	0.82
8	H_2	0.15	0.53
6	Air	0.41	1.00

Table 1.13 shows the range of calculated values of J_o using equation (5) for ø values obtained from the V_{oc} vs T measurements. For ø values of highly reduced devices the calculated values of J_o are of the same order as J_L, found from the I-V measurements. The possibility of band-to-band recombination being the dominant conduction loss mechanism is currently under investigation.

Table 1.13
Calculated values of J_o at the Richardson constant limit using ø values obtained from Figure 2

ø (eV)	J_o (mA/cm²)	Voc+ (V)
1.0	7×10^{-8}	0.52
0.82	6×10^{-5}	0.35
0.53	4	0.06

+ assuming $J_L=J_{sc}$ = 33mA/cm² and A=1.

Light intensity measurements

The large apparent photocurrent J_{LA} observed in highly reduced devices lead us to further investigate the light intensity effects in these devices. The short-circuit current J_{sc} was found to change linearly with illumination while J_o was found to increase with light intensity. Such an experiment is usually used to determine the diode factor A from equation (3) with the assumptions that $J_o \ll J_L$ and J_o remains constant under the different light intensities. In this case neither of the assumptions are valid and equation (3) cannot be used to determine A.

Resistivity measurements

Light I-V testing using cut-off filters to change the amount of light absorbed in the CdS, lead us to conclude that the changes in I-V behavior observed during an oxidation/reduction heat treatment cycle were taking place in the $CuInSe_2$, and in particular they were related to the change of the resistivity of the $CuInSe_2$. This was supported by measurements of $CuInSe_2$ samples deposited on glass.

Table 1.14 shows the sheet resistance in the dark and under illumination obtained from a set of $CuInSe_2$ samples on glass under the different heat treatments. Dark resistivity of $CuInSe_2$ was found to increase by at least 2 orders of magnitude as a consequence of reducing heat treatments. Measurements in light show that $CuInSe_2$ becomes photoconductive. Complete reversibility of the dark resistivity of $CuInSe_2$ was achieved when submitted to an oxidation/reduction heat-treatment cycle.

Table 1.14
Sheet resistance of 3 μm thick $CuInSe_2$
submitted to reducing/oxidizing treatments

Heat Treatments	INITIAL		66h/200°C/H_2		24h/200°C/Air	
Samples	Sheet Resistance (ohm/O)□					
	D	L	D	L	D	L
3-1725.13	10^7	$3x10^6$	$2x10^9$	$9x10^6$	$8x10^4$	$4x10^4$
3-1735.13	$7x10^5$	$2x10^5$	10^7	$2x10^4$	4x105	$4x10^5$
3-1740.13	$2x10^4$	10^6	10^8	$2x10^4$	10^6	$5x10^5$
3-1750.13	$2x10^6$	10^6	$5x10^8$	10^7	10^5	$6x10^4$
3-1754.13	$2x10^6$	10^6	$5x10^8$	10^7	10^5	$6x10^4$

The increase in resistivity of $CuInSe_2$ is expected to shift the Fermi level E_f towards the middle of the energy gap. The Fermi level E_{fp} for a p-type $CuInSe_2$ under thermal equilibrium conditions is given by

$$E_{fp} - E_v = kT \ln \frac{N_v}{p} \qquad (6)$$

where E_v is the valence band energy level, N_v the effective state density of the valence band, and p the hole equilibrium free carrier concentration. Consider p_1, p_2 to be the carrier concentration of the same $CuInSe_2$ layer in an oxidized and highly reduced state respectively. Using equation (6) one can obtain the difference in E_f between the two concentrations in the form

$$E_{fp1} - E_{fp2} = kT \ln \frac{P_2}{P_1} \qquad (7)$$

Table 1.15 shows the shift in Fermi level towards the middle of the energy gap for a $CuInSe_2$ layer in different reducing states represented by the ratio P_1/P_2. The shift of E_f towards the middle of the gap changes the band bending at the interface between $CuInSe_2$ and CdS which reduces the barrier height ϕ.

Table 1.15
Shift of the Fermi-level towards the middle gap
for high resistivity $CuInSe_2$

P_1/P_2	$(E_{fp_1} - E_{fp_2})$ (eV)
10^2	0.12
10^3	0.18
10^4	0.24
10^5	0.30

Figure 1.8(a) shows the energy band diagram of CdS and $CuInSe_2$ before the formation of the heterojunction. ΔE_c is the conduction band discontinuity between the CdS and $CuInSe_2$, E_{fn}, is the Fermi level in CdS while E_{fp1} and E_{fp2} are the positions of the Fermi level in the $CuInSe_2$ for an air optimized and strongly reduced devices respectively. Figure 1.8(b) shows the energy band diagram during the formation of the heterojunction. Primed symbols correspond to E_{fp2} while all others correspond to E_{fp1}. The high resistivity $CuInSe_2$ reduces the band bending on both sides of the junction which reduces the barrier height.

Spectral Response

Figure 1.9 shows the normalized spectral responses of a device in oxidized state followed by a reduced state and a second oxidized state. The spectral response of the reduced state shows a loss in the 550-800 nm region with substantial gain in the 1000-1300 nm region. Work is under way to explain this behavior. As was expected the spectral response obtained after the second oxidation is almost the same as the one obtained from the first oxidation of the device.

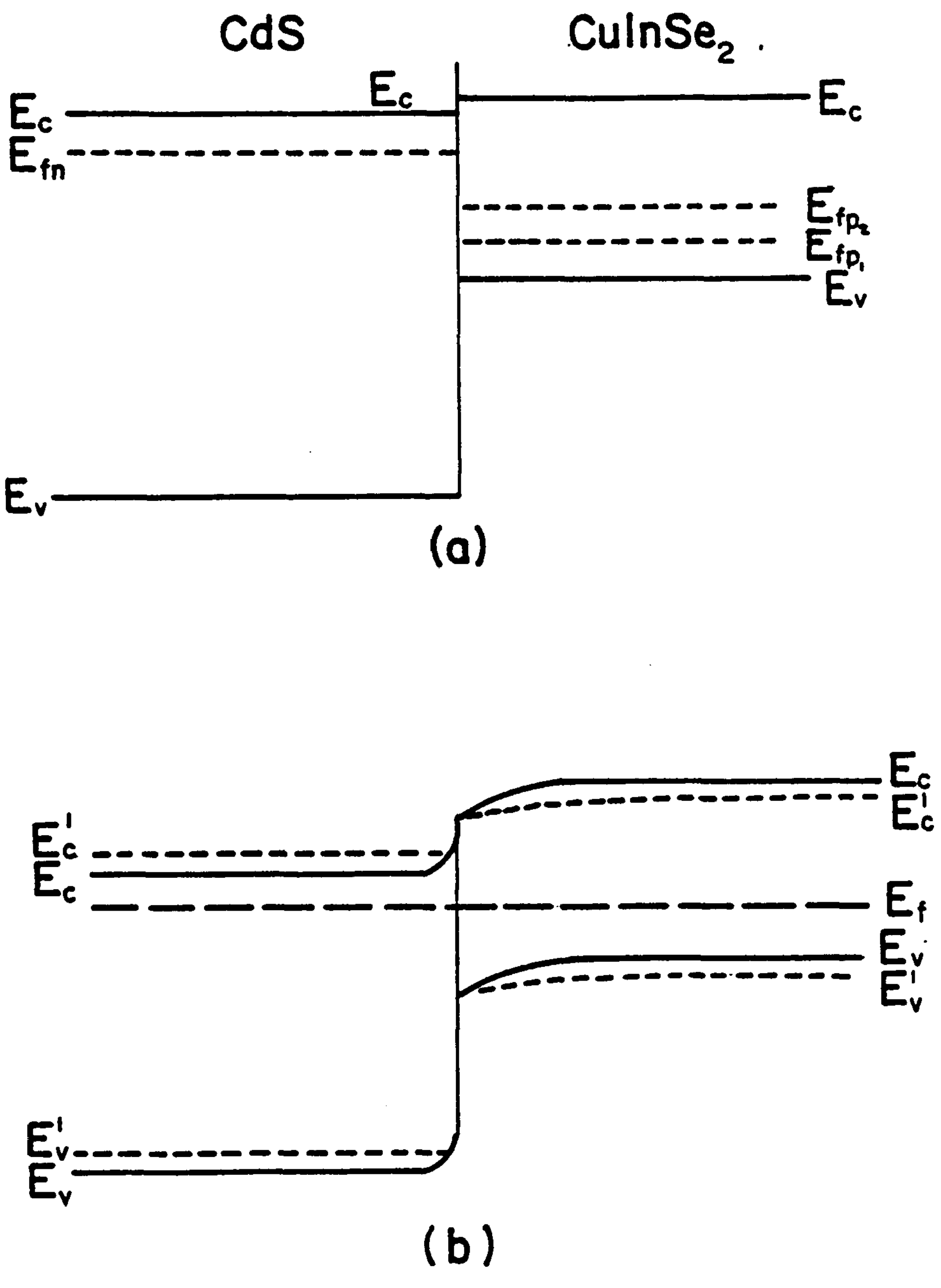

Figure 1.8: (a) Energy band diagram before the formation of the heterojunction; (b) Energy band diagram after the formation of the heterojunction.

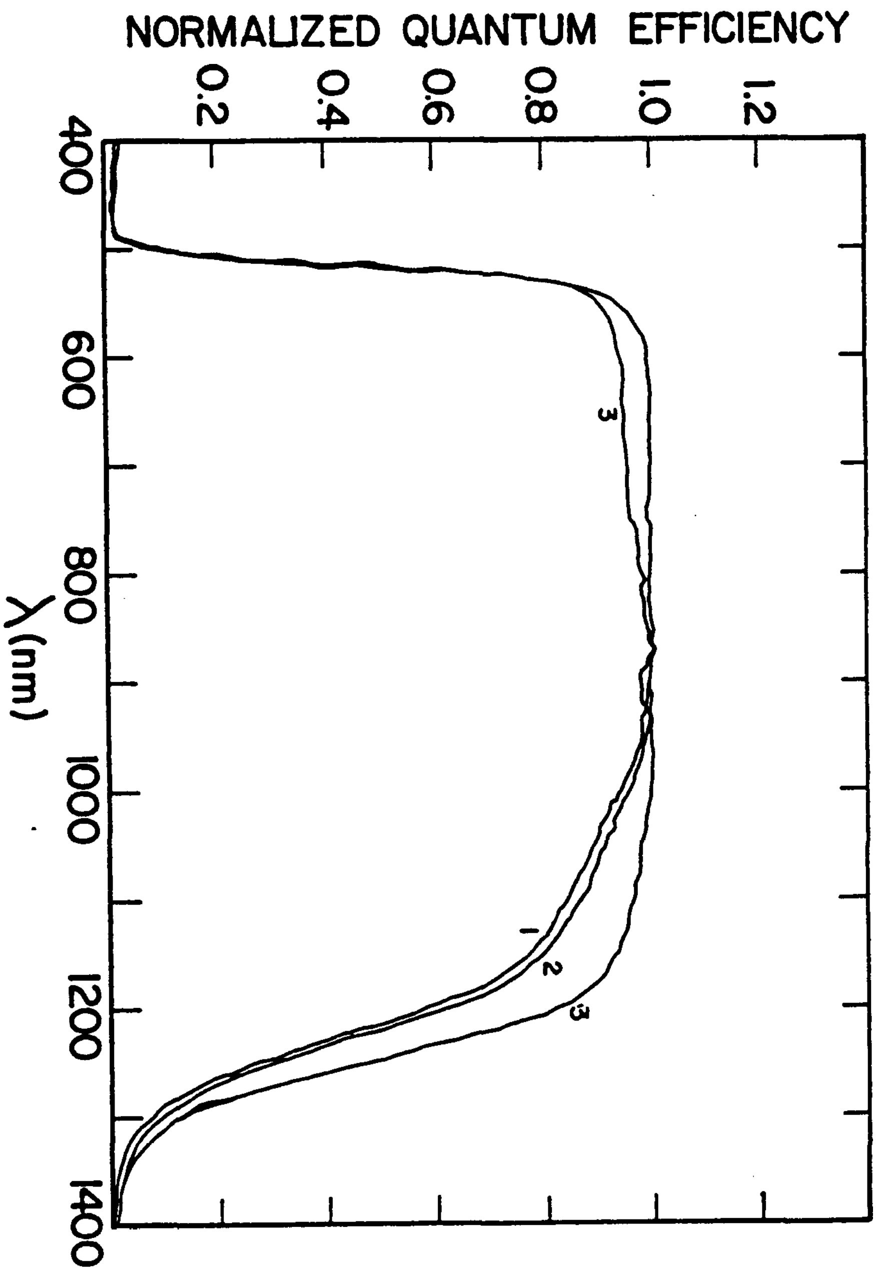

Figure 1.9: Normalized spectral response of a device submitted to an oxidizing/reducing cycle. 1. 48 hr/200°C/Air 2. 40 hr/200°C/H_2 3. 14 hr/200°C/Air

1.3.3 Non-ohmic back contact

In general any analysis of $CuInSe_2$/CdS devices assumes the contacts to $CuInSe_2$ and CdS to be ohmic. However, the ohmicity of the Mo/$CuInSe_2$ contact has been previously investigated[33] as a possible source of loss in V_{oc} and fill factor. Figure 1.10 shows the I-V behavior of an optimized $CuInSe_2$/CdS device at different temperatures. A second diode characteristic is observed at lower temperatures in forward bias indicating the presence of a junction in series with the main heterojunction. In general, the onset of the second diode is observed just below 0°C, although this varies from sample to sample, and the diode breakdown occurs at a voltage >2.5V. At room temperature the barrier height of the second junction is low enough to behave as an ohmic contact and is expected to have a minimum effect on the V_{oc} but could affect the fill factor. As the temperature is reduced the band bending extends into the $CuInSe_2$ increasing the number of photo-generated carriers collected by the second junction instead of the main heterojunction. At the same time the reverse saturation current J_o for the back contact decreases and at sufficiently low temperatures the second diode characteristic is observed. Figure 1.11 shows the proposed energy band diagram with the second diode present.

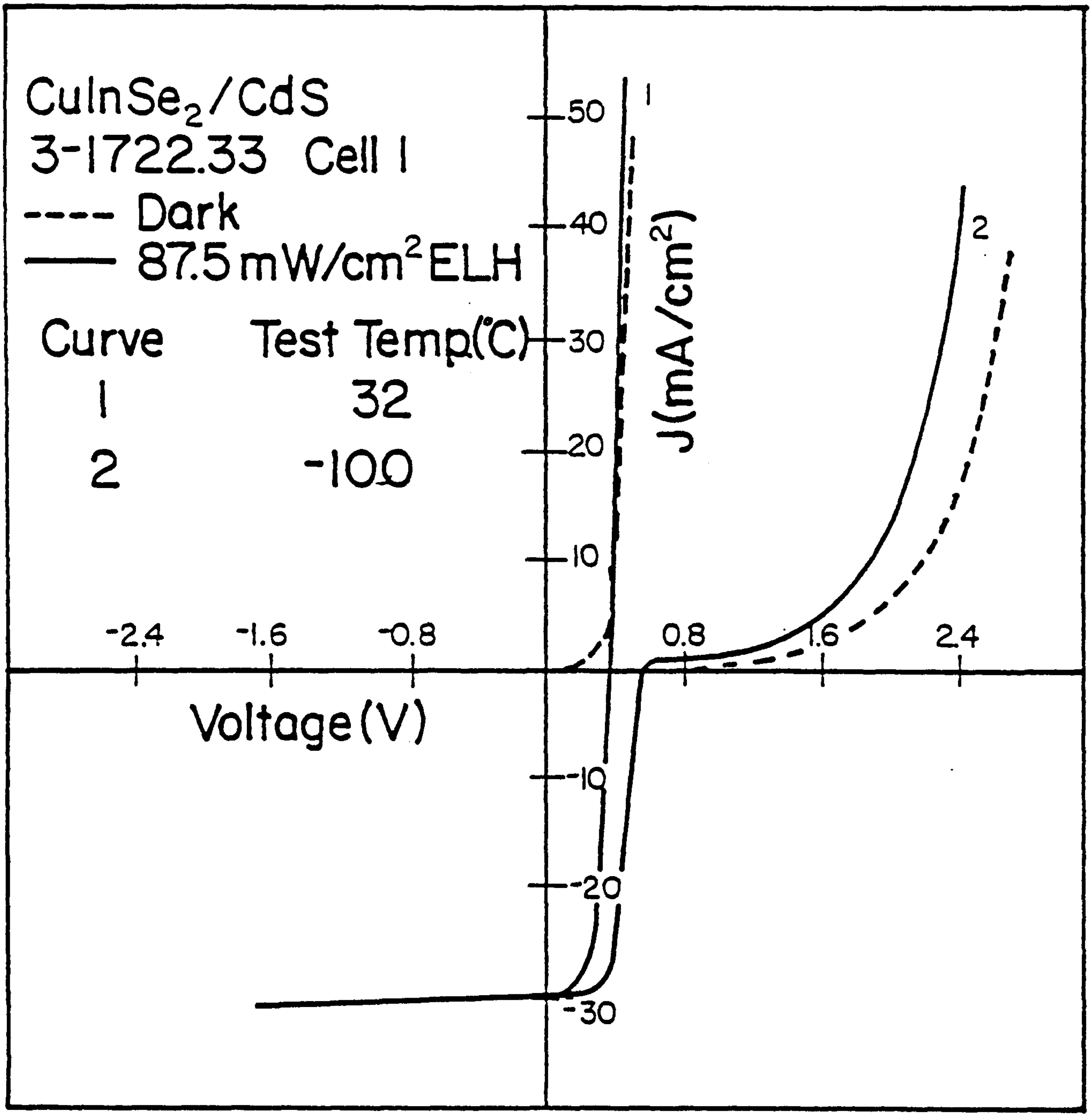

Figure 1.10 Current voltage curves of a CuInSe$_2$/CdS device at different temperatures.

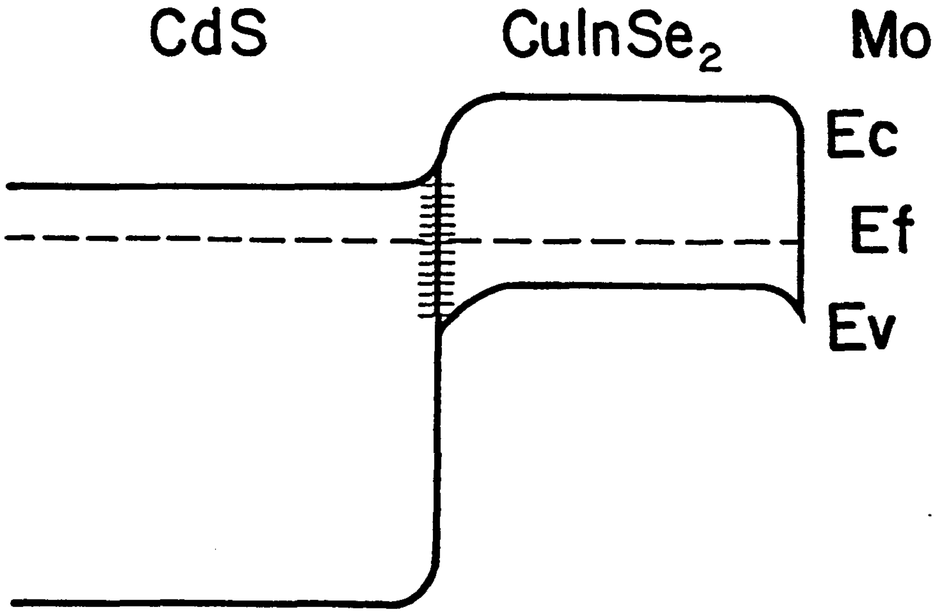

Figure 1.11: Suggested band diagram for the CdS/CuInSe$_2$/Mo structure at low temperatures.

1.3.4 Effect of zinc concentration in the (CdZn)S/$CuInSe_2$ heterojunction

Increasing the zinc content of the (CdZn)S increases the band gap of the heterojunction window layer. This should improve the performance of the $CuInSe_2$ solar cell due to enhancement in both J_{sc} and V_{oc} as discussed below.

The wider band gap optical window should allow more photons to pass through without being absorbed, hence generating more carriers in the absorber layer. This should show up as an increase in the measured short circuit current J_{sc} of the device.

Figure 1.12 shows the spectral responses of three cells on the same $CuInSe_2$ but with different Zn content in the (CdZn)S. The curves clearly show the increase in the (CdZn)S bandgap resulting in enhanced spectral response in the short wavelength region. Table 1.16 summarizes the results for these samples, showing about a 5% increase in J_{sc} for the cell with (CdZn)S.

Surprisingly, simultaneous enhancement of the response in the region from 950 to 1250 nm with increasing Zn content has been observed. The Zn causes a gain in collection efficiency in both the short and long wavelength region increasing the J_{sc}. The origin of the increased long wavelength response with Zn content is not clearly understood at this time.

Table 1.16
Summary of results concerning the increase in J_{sc} with the increase in bandgap of the CdS with the addition of Zn.

Device #	Zn%	Cut off in blue region	Shift in blue region	J_{sc}+ mA/cm²
31736.11 04	0	490 nm ~2.53 eV	0	31.05
31723.32 04	21.9	460 nm ~2.7 eV	0.17 eV	32.59
31741.22 05	23.5	460 nm ~2.7 eV	0.17 eV	33.34
31739.22 04	25.6	460 nm ~2.7 eV	0.17 eV	33.79

+ELH simulation at 87.5 mW/cm²; cell temperature: 32°C

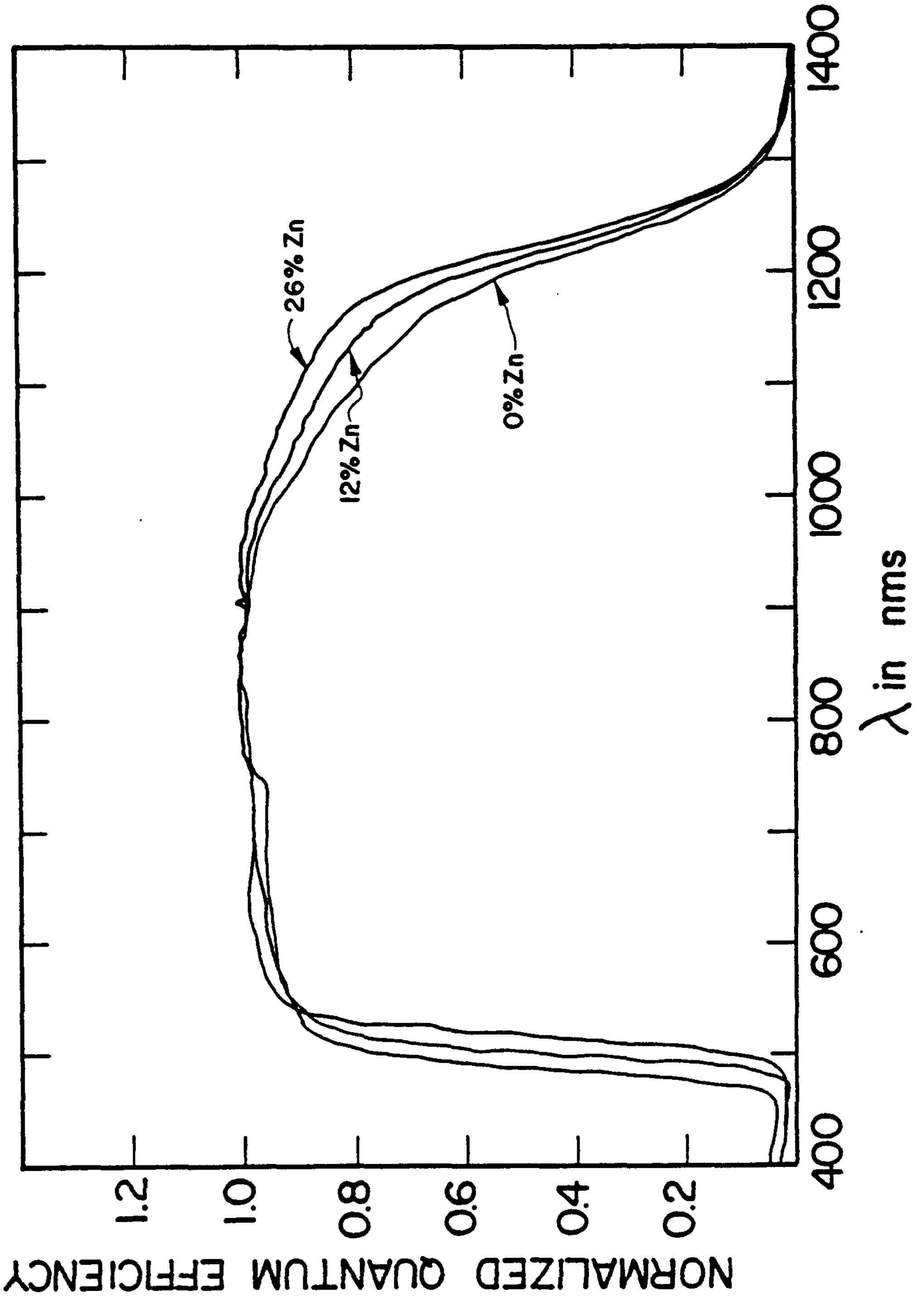

Figure 1.12: Spectral Response measurements of a set of cells with different Zn content in (CdZn)S.

The addition of Zn in the CdS was expected to increase the V_{oc} of the cells by reducing the electron affinity mismatch between the CdS and $CuInSe_2$. This is based on the assumption that interface recombination is the dominant conduction mechanism as was the case for the CdS/Cu_2S cell[8]. A change in the conduction band discontinuity ΔE_c should be directly reflected in ϕ and thus V_{oc}. Figure 1.13 shows the energy band diagram of a $CuInSe_2/CdS$ cell and the expected changes for with Zn content in CdS. Primed symbols reflect the latter case. The barrier height ϕ in the $CuInSe_2/CdS$ case can be expressed in terms of

$$\phi_B = Eg_2 - \Delta E_c - \delta_n - \delta_p \qquad (8)$$

Addition of Zn in CdS will result in a reduction in ΔE_c which should be reflected in V_{oc}.

Internal photoemission measurements at energies less than the intrinsic bandgap of the $CuInSe_2$ were used to obtain the barrier heights. The measurements on various mixed sulphide films do not show the expected increase in ϕ and V_{oc} as seen in Table 1.17. The above indicate that interface recombination is not the dominant conduction mechanism. Experiments are currently under way on the possible conduction mechanisms in these devices.

Table 1.17

Barrier height and open-circuit voltage results for a set of cells with different Zn content in (CdZn)S

Device #	% Zn	V_{oc} in volts	ϕ in eV
	31723 samples		
31723.23 -304	0	0.394	0.90
31723.32 -304	21.9	0.406	0.92
	31739 samples		
31739.33 -304	0	0.394	0.92
31739.23 -305	12	0.400	0.91
31739.22 -304	26	0.414	0.92

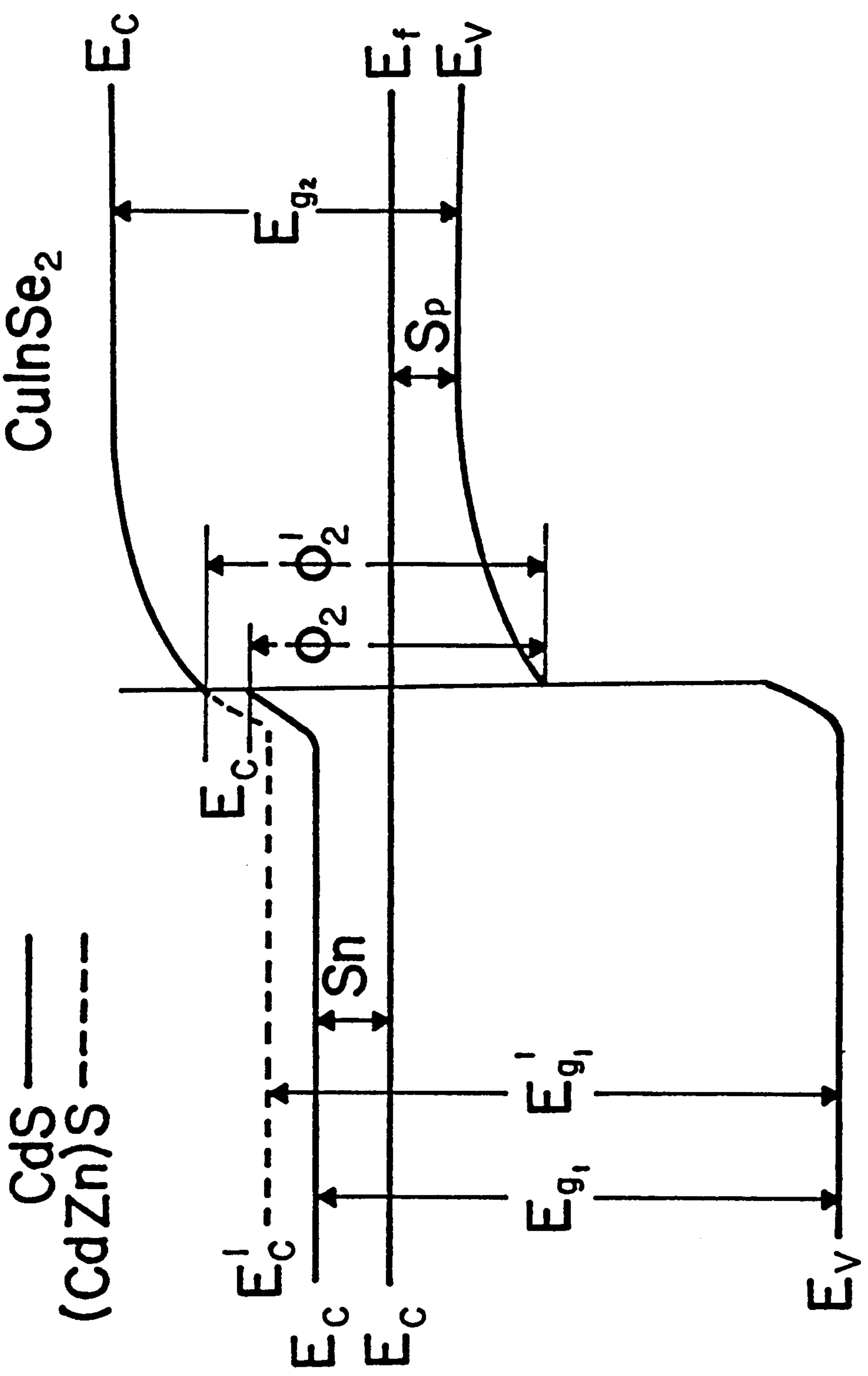

Figure 1.13: Energy band diagram of a $CuInSe_2$/CdS cell and the expected changes due to the addition of Zn in CdS.

SECTION 2.0

CdTe Cell Development

The major problems associated with making high efficiency CdTe/CdS cells are to reproducibly control the p-type conductivity of the CdTe film and to form a low resistance ohmic contact to it. Further, since the cells are being developed for tandem structures, the contact must be transparent as well as ohmic. Two CdTe/CdS device configurations have been examined. First, either CdTe or (CdHg)Te was deposited on a transparent conductive substrate followed by CdS to form the heterojunction. CdTe films with ~5% Hg were used rather than pure CdTe since lower deposition temperatures were possible and the electronic properties of the films were more reproducible[9]. This structure can be used in a monolithic CdTe-$CuInSe_2$ tandem cell structure but requires the formation of a transparent ohmic contact during the CdTe deposition. For the second structure, the CdTe is deposited on a 7059/ITO/CdS substrate leaving the CdTe surface exposed. With an appropriate transparent contact to the CdTe, this structure can be used in four-terminal mechanically stacked tandem cells.

2.1 7059/TCO/Cu/(CdHg)Te/CdS CELLS

Transparent (CdHg)Te/CdS solar cells have been made with efficiencies of 5-6% using either SnO_2 or ITO with 2-10nm of Cu as the transparent ohmic contact to the (CdHg)Te. However, the process for making the devices was not reproducible. Of the 111 samples processed into cells with transparent contacts only 18 samples yield devices over 3%. There was little or no correlation between deposition parameters, post deposition heat treatments or Cu thickness with device results. This lack of reproducibility made it impossible to optimize the deposition process. Furthermore, forming the CdTe transparent ohmic contact during deposition limits the ways in which the contact and CdTe properties can be modified after deposition.

In this section a summary of the work reported in previous reports under this contract, References [9] to [14], is described.

2.1.1 <u>CdTe -(CdHg)Te Film Growth and Cell Fabrication</u>

CdTe films were deposited by thermal evaporation from the compound using an effusion source. The bell jar deposition system typically operated at 1×10^{-6} torr except when using a dopant gas. The system was equipped with two additional effusion sources for elemental dopants. The range of deposition conditions used to grow CdTe films is summarized below:

CdTe effusion rate: 10-80 mg/min

Substrate temperature: 200-400°C

O_2 pressure: 9×10^{-4}-5×10^{-5} torr

Film growth rate: 0.01 - 0.2 μ/min

Single phase CdTe films were deposited provided the substrate temperature and effusion rates were appropriate. For high effusion rates and low substrate temperature multi-phase CdTe films were grown with Te precipitate. A semi-quantitative model of the growth kinetics was developed under SERI subcontract XL-4-03146-1[14].

To deposit (CdHg)Te films, a special effusion source was designed for Hg as described in Reference [9]. The range of deposition conditions were used to grow (CdHg)Te films and is summarized below:

CdTe effusion rate: 10-30 mg/min

Hg effusion rate: 20-70 mg/min

Substrate temperature: 140-200°C

Film growth rate: 0.02-0.04 μ/min

Single phase (CdHg)Te films were grown at substrate temperatures from 140 to 200°C. Above 200°C no Hg was incorporated in the films (maximum Hg effusion rate used increased the pressure in the belljar to 9×10^{-4} torr) and below 140°C multi-phase films were grown. The Hg incorporation was strongly dependent on the substrate temperatures. Reference [14] also presents a model for the (CdHg)Te growth kinetics.

The CdTe deposition system was equipped to hold nine 2.5×2.5 cm^2 samples which were radiatively heated. The substrate temperatures was controlled by a Eurotherm temperature controller using a thermo-couple embedded in one of the samples. In each deposition at least one Corning 7059 glass sample was included for optical and XRD measurements.

Three different conductive substrates 7059/Mo, 7059/ITO and 7059/SnO_2 were used in conjunction with a thin (10-100Å) Cu layer to provide ohmic contact to the CdTe. The optical and electrical properties of the CdTe-contact are discussed in sections 2.1.2.

For cell fabrication, the CdTe or (CdHg)Te films were heat treated in air at 300°C for 30 minutes prior to the CdS deposition. This treatment was found to improve the p-type conductivity of the film as well as the fill factor of the final device. The CdS was deposited by thermal evaporation from CdS powder at a film growth rate of 0.3 μm/min onto 200°C substrate. The resistivity of the CdS films was ~0.01Ω-cm and was controlled by co-evaporation of In during deposition. The low resistivity ensured that the depletion layer was entirely in the (CdHg)Te, thereby aiding current collection.

A sputtered ITO film (250nm thick) and a Ni bus bar were deposited to provide the ohmic contact to the CdS. The cell area and contacts were defined by a photolithography-etching procedure yielding 12 cells each 3x3 mm^2 on a 2.5x2.5 cm^2 substrate.

2.1.2 Film Properties

Structure

The CdTe and (CdHg)Te films were highly (111) oriented independent of substrates used. The degree of orientation and existence of Te second phases were routinely monitored using x-ray diffraction. Complete 2-theta scans were not necessary for this purpose and the following peaks were spot checked:

	CdTe		Te	
(hkl)	(111)	(311)	(100)	(003)
I/Io Random	100	50	20	8

Figure 2.1 shows representative x-ray diffraction scans for a film with and without a second Te phase.

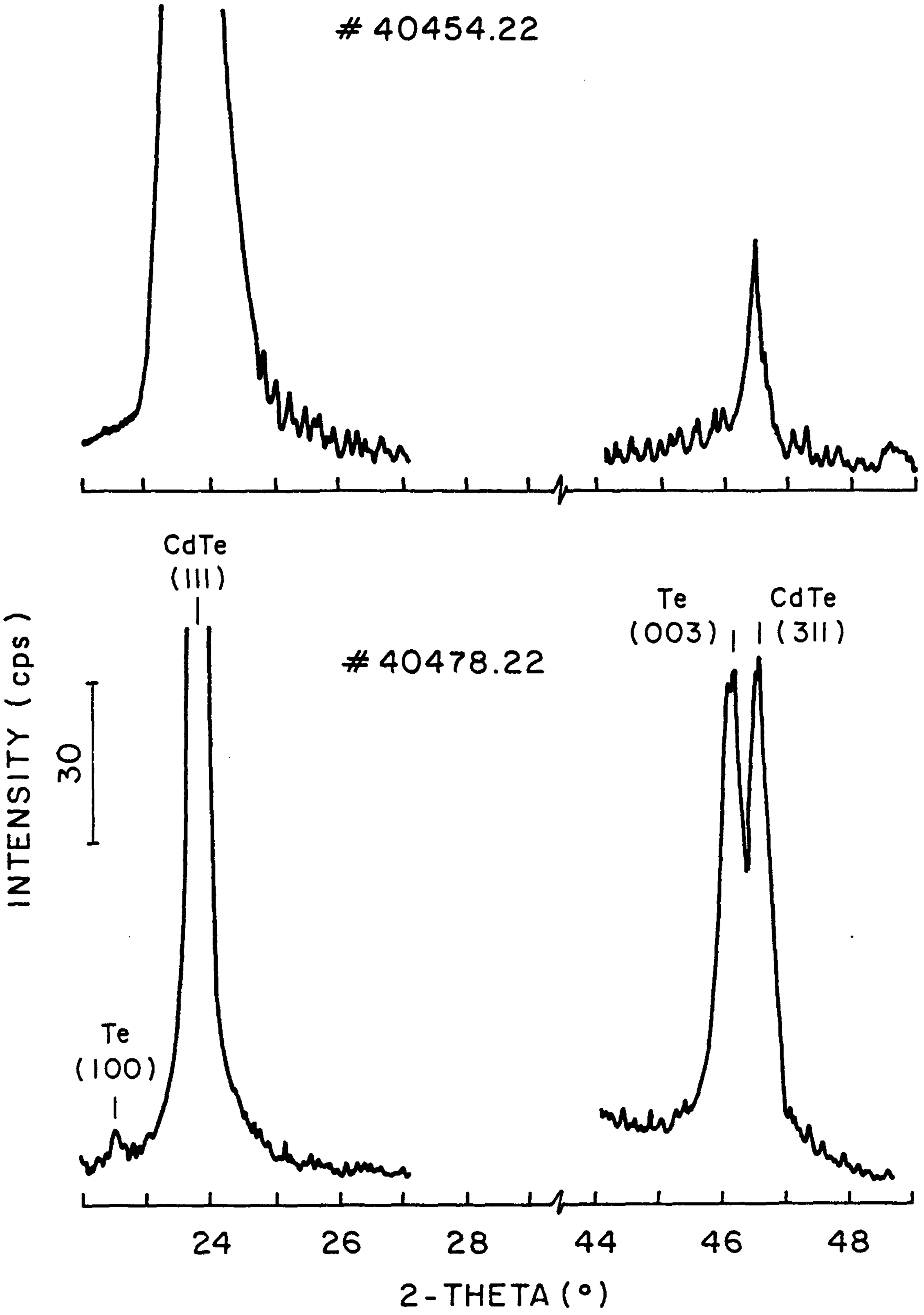

Figure 2.1: X-ray diffraction peaks for a CdTe film with and without a second Te phase

Effect of Cu on Film Growth

The thin Cu layer used to provide ohmic contact to the CdTe had adverse effects on the CdTe film growth which resulted in poor reproducible and yield of devices. The effects of Cu on the growth of CdTe were studied using XRD, SEM and Auger techniques and the results are discussed in References [10] to [12]. In summary, the Cu reacted with the Te forming a Cu-Te compound (probably Cu_2Te) resulting in whisker growth through the CdTe film. This growth left a textured and non-uniform surface on which to form the CdTe-CdS heterojunction resulting in poor yield and reproducibility of cell results. Further, the electrical and optical properties of the Cu/ITO contact to the CdTe were not reproducible and the variability was attributed to the Cu-Te interaction.

Composition and Bandgap of (CdHg)Te Films

The composition of (CdHg)Te films was inferred from bandgap or Auger election spectroscopy measurements. Five films covering the range of deposition conditions were sent to SERI for Auger analysis. The results are summarized in Table 2.1. The bandgap over this range of composition varied from 1.5 (0% Hg) to 1.3 eV (7.8% Hg) and is consistent with results reported by Li[15].

Table 2.1
AES bulk compositions determined by SERI
Analysis #1040

Substrate	Hg(a/o)	Cd(a/o)	Te(a/o)
40127.22	0	51	49
40307.22	< 1	49.8	49.5
40321.13	4.2	46	49.8
40323.13	7.8	43.5	49.6
40327.13	4.6	45.7	46.7

Transmission and Reflection

The total reflection and transmission of (CdHg)Te films deposited on ITO/Cu and SnO_x/Cu substrates were measured for Cu thickness from 2-10nm on as-deposited films and completed devices. The results including R and T for (CdHg)Te on 7059 glass are summarized in Table 2.2. As the Cu thickness increases transmission in the 950-1300 nm range drops and is below 30% for 10 nm Cu with the as-deposited films. However, a 3 hour, 300°C air heat treatment used to fabricate the devices increases the transmission to over 30%. For high efficiency tandem cells the transmission beyond the (CdHg)Te band edge for the entire (CdHg)Te cell should approach 90%. To achieve this, reflection losses will have to be minimized by proper control of individual layer thicknesses and appropriate AR-coatings. Absorption in the ITO/Cu/(CdHg)Te layer must be minimized by optimizing the Cu thickness and heat treatments while maintaining device performance and electrical properties of the contact.

Table 2.2
Nominal Transmission and Reflection at the
Indicated Wavelength (nm) for
As-Deposited (CdHg)Te Films on Different Contacts
and for Completed Cells

Substrate	Cu	Transmission %			Reflections %		
	(nm)	900	1025	1150	900	1025	1150
7059/(CdHg)Te	0	65	70	70	30	30	30
	2	60	60	50	25	25	30
7059/ITO/(CdHg)Te	5	45	40	40	20	20	20
	10	25	25	25	20	20	20
7059/SnO_2/(CdHg)Te	5	45	45	40	20	20	20
7059/ITO/(CdHg)Te/CdS/ITO	2	55	54	52			
	5	33	37	34			
	10	35	34	28			
7059/SnO_2/(CdHg)Te/CdS/ITO	2	60	62	60			
	5	43	43	42			
	10	33	33	32			

2.1.3 Cell Results

(CdHg)Te/CdS cells were fabricated on 214 2.5x2.5 cm^2 substrates each containing 12 $3x3mm^2$ cells. Of these samples, the (CdHg)Te contacts were:

1) 103 substrates with Mo/Cu
2) 69 substrates with ITO/Cu
3) 42 substrates with SnO_2/Cu

Tables 2.3 through 2.5 summarize the cell results for all devices with efficiencies greater than 3%. Included in the tables are the Cu thickness and the (CdHg)Te deposition parameters. Only 40 of the 214 substrates yielded devices over 3%. Little or no correlation was found between (CdHg)Te deposition conditions and device performance. Prior to CdS deposition (CdHg)Te heat treatments in air or O_2 at 300°C for 3 hours were required to produce "live" devices. The best devices were obtained using a Mo/Cu/(CdHg)Te with a Cu thickness of ~2nm as can be seen from the tables. (CdHg)Te devices with either ITO/Cu or SnO_2/Cu transparent contacts were produced with efficiencies greater than 5%. Al-Copper thickness of 2 to 10 nm was required to form a moderately good ohmic contact to the (CdHg)Te. For most devices, the I-V curve exhibited some curvature in the forward bias region indicating a non-ideal ohmic contact. Due to the lack of reproducibility of the cell fabrication process and the difficulty in forming an ohmic contact, emphasis of the research was directed towards the inverse device structure described in the next section.

Table 2.3

I-V Results of CdTe/CdS cells with an ITO/Cu Contact

Sample #	CdTe Deposition				HT Atmos	Best I-V Parameters			
	Tsub (°C)	Thk μm	Time (min)	Hg (°C)		Voc (V)	Jsc+ (mA/cm²)	FF (%)	Eff (%)
				Cu Thickness: 10nm					
40447.21	180	2.8	130	115	O_2	0.5817	16.74	49.27	5.48
				Cu Thickness: 5nm					
40447.13	180	2.8	130	115	O_2	0.5143	15.52	47.51	4.33
40448.13	180	2.9	130	115	O_2	0.4578	15.35	49.77	4.00
				Cu Thickness: 2nm					
40445.11	180	3.0	130	115	O_2	0.5220	14.32	47.19	4.03
40441.21	180	3.0	130	115	Air	0.5164	15.15	43.46	3.89
40447.12	180	2.8	130	115	O_2	0.5338	12.69	44.41	3.44
40437.11	180	1.9	98	116	Air	0.4444	14.05	45.20	3.23
40443.11	180	3.0	130	115	O_2	0.4872	13.07	43.38	3.16
40439.23	180	1.9	98	115	Air	0.4375	14.97	41.02	3.07
				Cu Thickness: 1nm					
40434.11	180	1.6	78	115	Air	0.2549	3.52	33.57	0.34

Note:
1. Cells with $\eta > 3\%$
2. Heat treatment prior to CdS deposition: 3 hr. 300°C in either O_2 or Air
3. CdS - thickness: ~2 μm
   resistivity: $\sim 10^{-2}$ Ω.cm

+ELH simulation at 87.5 mW/cm²; cell temperature 32°C

Table 2.4

I-V Results of CdTe/CdS cells with a SnO$_2$/Cu Contact

Piece #	CdTe Deposition				HT	Best I-V Parameters			
	Tsub (°C)	ThK μm	Time (min)	Hg (°C)		Voc (V)	Jsc$^+$ (mA/cm^2)	FF (%)	Eff (%)
				Cu Thickness: 10nm					
40449.21	180	2.7	130	115	Air	0.5458	13.05	44.60	3.63
				Cu Thickness: 5nm					
40449.12	180	2.7	130	115	Air	0.5765	15.65	52.74	5.44
40469.11	180	2.8	130	125	O$_2$	0.4043	14.08	49.54	3.22*
40460.21	180	2.9	130	125	O$_2$	0.5253	12.71	41.01	3.13
40469.32	180	2.8	130	125	O$_2$	0.4713	14.22	39.96	3.06
				Cu Thickness: 2nm					
40441.31	180	3.0	130	115	Air	0.5414	16.41	41.23	4.19
40445.32	180	3.0	130	115	Air	0.5219	13.74	44.01	3.61
40437.211	180	1.9	98	116	Air	0.4524	14.33	42.01	3.11

Note: 1. Cells with ^{n}>3%

2. Heat treatment prior to CdS deposition: 3 hr. 300°C in either O$_2$ or Air (*HT at 500°C)

3. CdS - thickness: ~2 μm
resistivity: ~10^{-2}Ω-cm

+ELH simulation at 87.5 mW/cm^2; cell temperature 32°C

Table 2.5

I-V Results of CdTe/CdS cells with a Mo/Cu Contact

Piece #	CdTe Deposition				HT	Best I-V Parameters			
	Tsub (°C)	ThK µm	Time (min)	Hg (°C)		Voc (V)	Jsc$^+$ (mA/cm^2)	FF (%)	Eff (%)
				Cu Thickness: 10nm					
40447.31	180	2.8	130	115	O_2	0.5099	16.25	47.19	4.47
40448.31	180	2.9	130	115	O_2	0.5204	11.77	44.80	3.14
				Cu Thickness: 5nm					
40376.31	160	1.5	75	115	Air	0.5857	16.01	45.85	4.91
40381.21	160	2.3	123	115	Air	0.6190	15.81	43.61	4.88
40377.31	160	1.7	75	115	Air	0.6026	13.14	42.67	3.86*
40379.21	160	1.4	67	115	Air	0.4698	13.68	49.30	3.62
				Cu Thickness: 2nm					
40430.12	161	1.6	77	115	Air	0.5399	18.27	57.05	6.43
40428.12	161	1.7	72	115	Air	0.4592	19.45	58.74	6.00
40435.21	180	1.9	98	115	Air	0.5527	17.54	52.65	5.83
40427.21	161	1.6	69	115	Air	0.5262	18.73	50.23	5.66
40366.21	160	2.3	90	115	Air	0.4607	18.90	56.74	5.65
40381.11	160	2.3	123	115	Air	0.5918	16.94	48.32	5.54
40423.21	180	1.8	78	115	Air	0.5620	16.61	49.91	5.32
40421.31	160	1.8	60	115	Air	0.5326	16.18	51.50	5.07
40431.21	161	1.7	69	115	Air	0.4967	18.01	48.12	4.92
40444.31	180	2.8	130	115	O_2	0.5359	14.90	49.77	4.54
40434.21	180	1.6	78	115	Air	0.5089	15.88	49.01	4.53
40438.11	180	1.9	98	115	O_2	0.5565	15.67	45.25	4.51
40440.31	180	2.9	130	115	Air	0.4580	16.95	49.95	4.43
40442.11	180	3.0	130	115	Air	0.5135	16.01	46.88	4.40
40441.11	180	3.0	130	115	O_2	0.5443	16.53	39.61	4.07
40378.11	160	1.0	50	115	Air	0.5527	14.18	41.36	3.70
40439.11	180	3.0	130	115	Air	0.5457	14.57	40.69	3.70
40380.32	160	2.0	100	115	Air	0.5177	12.52	49.63	3.68*
40429.12	161	1.6	74	115	Air	0.5131	14.21	43.65	3.64
40444.23	180	2.8	130	115	O_2	0.4749	14.20	44.79	3.45
40400.23	160	2.5	167	115	Air	0.5068	11.53	47.91	3.20*
40382.11	180	1.5	82	115	Air	0.4746	12.29	45.68	3.04*
				Cu Thickness: 1nm					
40434.32	180	1.6	78	115	Air	0.4963	9.46	33.09	1.77

Note:
1. Cell with ^{n}>3%
2. Heat treatment prior to CdS deposition: 3 hr. 300°C in either O_2 or Air (*HT at 350°C)
3. CdS - thickness: ~2 µm resistivity: 10^{-2}Ω-cm

+ELH simulation at 87.5 mW/cm^2; cell temperature 32°C

2.2 7059/ITO/CdS/CdTe CELLS

Transparent CdTe/CdS cells have been made with efficiencies over 8.5% and transmission to sub-bandgap light of about 50% (at 1000nm). A reproducible technique for forming a transparent ohmic contact to a CdTe/CdS cell has been developed. Short circuit currents of over 19 mA/cm^2 and fill factors as high as 70% have been measured for various devices. The highest open circuit voltage was ~0.650 V which is lower than the 0.700 to 0.750 nV reported for the best electroplated[16] or CSVT CdTe/CdS cells[17]. The control of the CdTe resistivity and the transparency of the entire device structure were the major problems remaining at the end of the contract.

2.2.1 CdTe and (CdZn)Te Film Growth and Cell Fabrication

The superstrates for the inverse cell were Corning 7059 glass are sputter coated with ITO with sheet resistance of ~10Ω/■ at a thickness of 400nm. Nominally 1 micron of CdS was deposited onto the 7059/ITO samples at a substrate temperature of 200°C and growth rate of 0.4 to 0.1 µm/min. The 7059/ITO/CdS superstrates for some cells were heat treated in air at 300°C for 3 hours since preliminary experiments indicated that this resulted in higher V_{oc}. The CdTe films were deposited onto the superstrates at a temperature of 200-300°C and film growth rates of 0.01 to 0.5 µm/min. The entire structure was then heat treated in air to lower the resistivity of the CdTe (discussed in section 2.2.2), etched to remove surface oxides and an ohmic contact formed. Cell areas were delineated by a photolithography-etch technique or by depositing the contact through an aperture mask. (CdZn)Te films were deposited by adding a ZnTe source to the deposition systems. A limited number of films were deposited to determine if the addition of Zn could be used to increase the conductivity of the films and to evaluate cells using the wider bandgap material.

2.2.2 Film Analysis

Effect of Heat Treatments on CdTe cross-grain resistivity

Experiments were conducted to determine the effect of heat treatments on the cross-grain resistivity, with particular attention placed on heat treatment temperature, time, and atmosphere. CdTe films were deposited on 7059/ITO substrate with a 100 micron gap which allowed cross-grain resistivity measurements of the films. Resistivity of CdTe films deposited under various conditions were nominally the same with dark resistivities in the range 5×10^{7} to 5×10^{8} ohm-cm, and light resistivities in the range of 1×10^{6} to 3×10^{6} ohm-cm.

Table 2.6 shows cross-grain resistivity data for CdTe films grown at a substrate temperature of 250°C and a growth rate of ~25A/sec. The samples were air heat treated for 15 minutes as described in appendix 2.

Table 2.6 CdTe Cross-grain resistivity as a function of temperature for samples from 40560.

Sample Condition	Temperature (C)	Cross-Grain Resistivity Dark	Light
As-Deposited	-	3×10^{8}	1×10^{6}
Heat Treated	400	1×10^{7}	2×10^{4}
Heat Treated	500	7×10^{7}	1×10^{4}
Heat Treated	550	3×10^{6}	4×10^{3}

At temperatures of 600°C and above, air heat treatments result in reaction/evaporation of the films from the substrate so that no measurements were possible. At temperatures below 400°C, little or no change in resistivity is observed in the 15 minute interval used. The heat treatment at 550°C was the most effective at increasing the p-type conductivity of the CdTe films. For samples heat treated at 550°C, there was no difference in post-treatment resistivity between samples which had been quickly cooled and those which had been slowly cooled. See Appendix 3.

Table 2.7 summarizes the effect of heat treatment time for samples heat treated at 550°C in air for 2 to 15 minutes.

Table 2.7 CdTe dark and light resistivity versus 550°C Heat treatment time

Time	Cross-Grain Resistivity			
	Dark (Ω-cm)	Light (Ω-cm)	Dark (Ω-cm)	Light (Ω-cm)
	sample - #40538		sample - #40549	
-	1×10^{8}	1×10^{6}	3×10^{8}	2×10^{6}
2	1×10^{8}	1×10^{8}	3×10^{8}	1×10^{4}
4	8×10^{7}	9×10^{3}	2×10^{7}	7×10^{3}
8	1×10^{7}	9×10^{3}	1×10^{6}	5×10^{3}
15	4×10^{6}	9×10^{3}	6×10^{6}	8×10^{3}

Before the HT the film resistivity is $\sim 10^{8}\Omega$-cm in the dark and $\sim 10^{6}\Omega$-cm under light bias. The dark resistivity is reduced by 2 orders of magnitude after 8 minutes at 550°C in air and is relatively stable for longer times. The light resistivity changes more rapidly, falling 2-3 orders of magnitude, in the first 2 minutes. From 4-15 minutes, there is no further change in light resistivity. In both the dark and light cases grain boundaries may be limiting the conductivity after the first few minutes of HT which would be consistent with work reported by Thorpe et al.[18]

To test the effect of atmosphere on the change in CdTe cross-grain resistivity, the 15 minute 550°C conditions were used. C/sec. Table 2.8 summarizes the cross grain resistivity measurements for inert, reducing and oxidizing atmospheres.

Table 2.8. CdTe cross-grain resistivity as a function of atmosphere for samples from 40536 and 40537.

Sample Condition	Atmosphere	Cross-grain Resistivity Dark	 Light
As Deposited		1×10^{8}	2×10^{6}
Heat Treated	Air	5×10^{6}	5×10^{3}
Heat Treated	Argon	2×10^{7}	9×10^{3}
Heat Treated	10% H2-Ar	1×10^{7}	2×10
Heat Treated	Hydrogen	4×10^{5}	2×10^{4}

The light and dark resistivity of the CdTe samples was lower for all samples independent of the atmosphere. This suggests that the temperature is the important parameter controlling resistivity. However, the best cell results were obtained with air heat treatments.

Temperature dependence of CdTe conductivity

Temperature dependent cross-grain conductivity measurements were made over the range 120°C>T>-40°C on CdTe films as-grown and after slow and quick cool heat treatments. Data for 2 samples is shown in figure 2.2 and in each case gives a good fit to $\sigma_d=\sigma_o \exp[-E_A/kT]$. The prefactors, σ_o, and activation energies, E_A, are listed in table 2.9. The as-grown films had $E_A \approx 0.7$eV indicating that the films are very intrinsic since $E_A \approx Eg/2$. The increase in the room temperature dark conductivity after heat treatment is due in part to the 0.03-0.06 eV change in E_A. There is also an increase in the prefactor, assuming $\sigma_o=q\mu p_o$, either the hole mobility or equilibrium concentration are increased by the heat treatments.

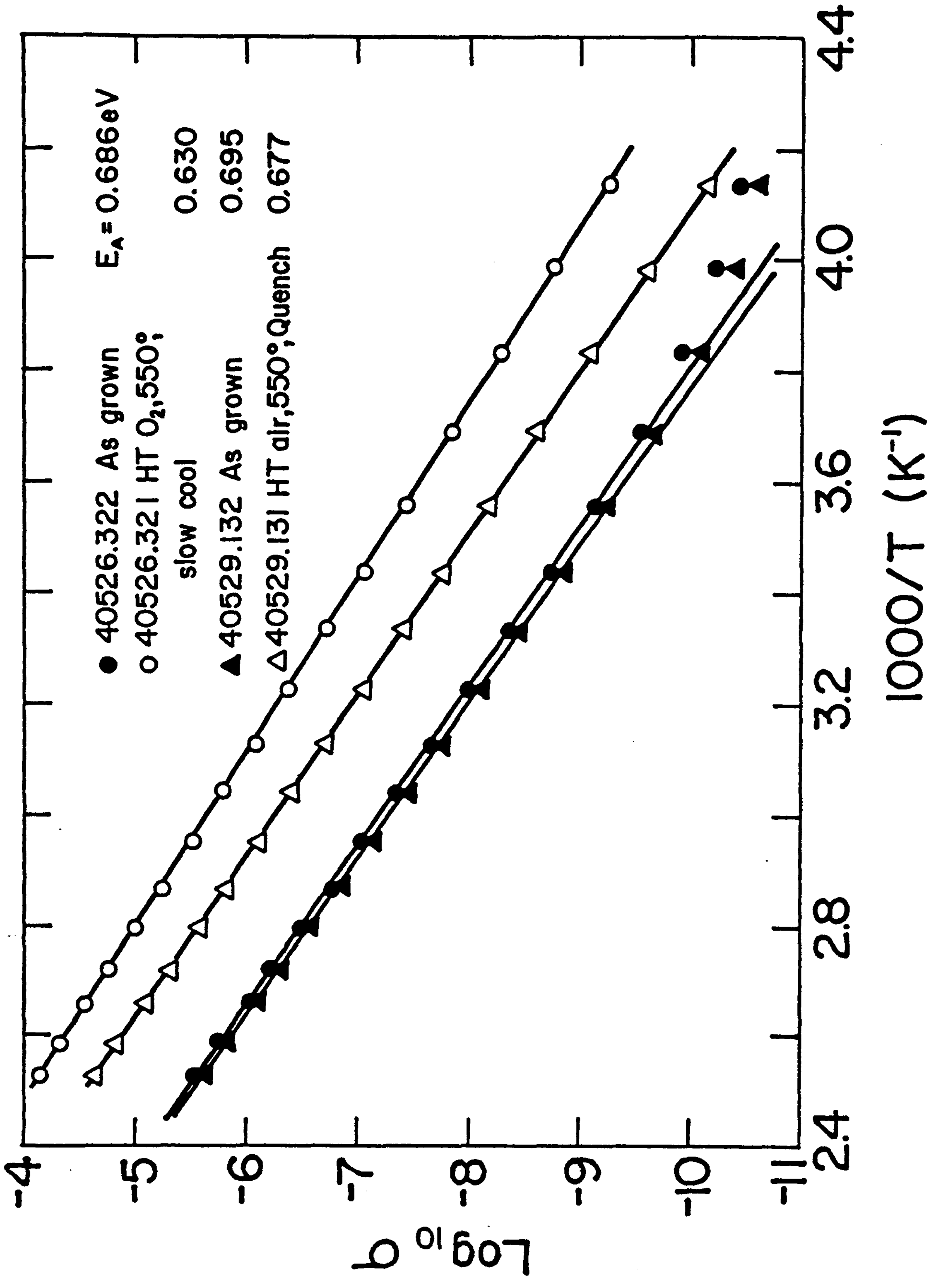

Figure 2.2: Temperature dependence of as grown and heat treated CdTe films.

Table 2.9
CdTe cross-grain conductivity temperature dependence: activation energy and prefactor

Sample	Condition	E_A(eV)	σ_0=(S/cm)	σ_d(300k)(S/cm)
40526-322	as-grown	0.69	1.5×10^{3}	3.8×10^{-9}
40526-321	HT(550°C,O_2, 15 min, slow cool)	0.63	7.4×10^{3}	1.7×10^{-7}
40529-132	as-grown	0.70	1.6×10^{3}	3.0×10^{-9}
40529-131	HT(550°C,air	0.67	9.0×10^{3}	3.5×10^{-8}

Composition, Bandgap and Resistivity of (CdZn)Te Films

The composition, bandgap and resistivity of (CdZn)Te films was determined and the properties compared with CdTe films. Table 2.10 summarizes the properties of the (CdZn)Te films.

Table 2.10
Properties of (CdZn)Te Films

Sample #	Zn Content (XRD) (%)	R+T at 1000nm (%)	Resistivity Dark (Ω-cm)	Resistivity Light (Ω-cm)	Eg (eV)
40503	2	~100	1.7×10^{8}	1.3×10^{6}	1.55
40501	5	~100	9.6×10^{7}	4.3×10^{7}	1.56
40504	5	95	1.2×10^{8}	1.2×10^{6}	
40552	5	~100	6.0×10^{8}	2.6×10^{6}	1.56
40502	7	~100	2.0×10^{7}	1.4×10^{6}	1.55
40507	10	~100	5.9×10^{8}	1.9×10^{6}	1.59
40508	10	~100	5.3×10^{7}	2.7×10^{6}	1.60
40553	10	~100	1.8×10^{8}	2.4×10^{6}	1.58
40554	10	~100	3.5×10^{8}	3.4×10^{6}	1.59
40499	17	89	8.5×10^{6}	6.7×10^{6}	1.63
40555	23	~100	1.1×10^{8}	1.6×10^{6}	1.68
40500	28	~100	2.0×10^{8}	4.9×10^{7}	1.68
40563	34	~100	6.6×10^{7}	1.6×10^{6}	1.72
40564	53	~100	2.2×10^{7}	6.1×10^{5}	1.79
40565	53	~100	2.4×10^{7}	6.9×10^{5}	1.76
40566	58	~100	8.6×10^{6}	4.0×10^{5}	1.86

The bandgap of the films was varied from 1.55 to 1.68 eV covering a composition range from ~5 to 23% Zn. The composition vs bandgap results are consistent with those reported by Olego et al.[19] for epitaxially grown (CdZn)Te films and the transmission of the films at 1000nm is comparable to our CdTe films. All films were high resistivity and p-type and the light to dark variation in resistivity was similar to the CdTe films. Some films were heat treated in air at 550°C for 15 minutes which reduced the dark resistivity to ~10^4Ω-cm similar to the results obtained on CdTe films. Thus, the addition of Zn did not aid in controlling the p-type resistivity of the films. Cells were made on some of these films and the results are discussed in Section 2.2.4.

2.2.3 Transparent Cu/ITO Contact

For use as the top cell in a tandem device, the CdTe cell must be transparent to light in the sub-band gap energy region $850\ \text{nm} < \lambda < 1400\text{nm}$. The sum of total reflection (R) and transmission (T) is shown in Figure 2.3 after 5 steps in the cell processing procedure optimized for maximum T. R and T measurements were made with a Perkin-Elmer model 330 spectrophotometer equipped with a 60 nm diameter integrating sphere. These process steps are: 1) the ITO (400 nm) front contact on a 7059 substrate, 2) CdS (1.7μ) then CdTe (1.2μ) deposited, 3) heat treated at 550°C for 4 minutes in air with rapid cooling, 4) KOH etch (4 molar, 60°C, 30 seconds), and 5) deposition of the Cu/ITO (2nm Cu, 200nm ITO) back contact. With anti-reflection coatings used to reduce R to <5% and a grid adding another 5% reflection, the total transmission would be ~50%.

The ITO film has ~3% absorption (A=1-R-T) for $500 < \lambda < 1000\text{nm}$ but increases to ~15% at 1400nm. There is additional absorption after the CdTe and CdS films are deposited such that at =1000nm R+T varies between 80 and 90%. The pre-contact heat treatment (HT), needed to increase the p-type conductivity of the CdTe, increases the absorption of the structure. The extent of this additional absorption depends on details of the HT including time, temperature, atmosphere, and cooling rate. The ITO also becomes more absorbing with HT for >1100nm causing the additional falloff seen in the R+T curve.

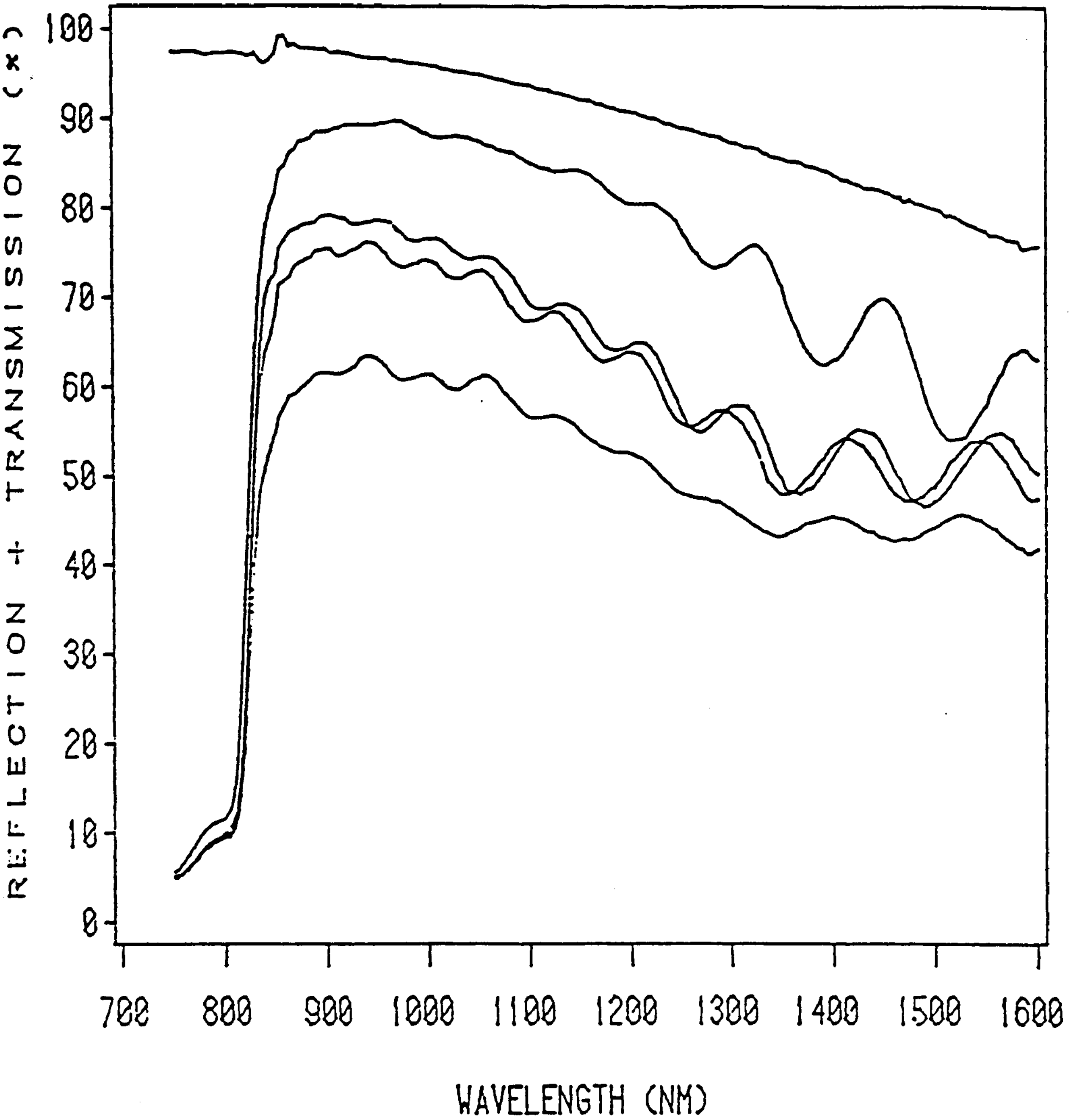

Figure 2.3: Reflection plus transmission after 5 cell processing steps.

A number of tests have been made to minimize the effect of the HT on the optical transparency while maximizing the final cell performance. Lower temperatures have less effect on transparency while there is no reduction in R+T, after 1 hour when the H.T. is done at 400°C. However, conductivity measurements on the CdTe films as well as final cell results indicate that 550°C is necessary.

The effect of the HT time on the transparency, cell results, (see section 2.4) and CdTe film resistivity (see section 2.2) has also been investigated. Three 7059/ITO/CdS/CdTe samples from CdTe deposition #40570 were cut in half and then heat treated from 1 to 15 minutes in air and rapidly cooled. R and T measurements were made after the HT and after the subsequent KOH etch. R+T at 1000 nm is shown for each case in Figure 2.4. Reducing the HT time as much as possible is clearly advantageous. At 1400 nm, where R+T is lower due to absorption in the ITO, there is little change in R+T with HT time.

The effect on the CdTe transparency of the 550°C HT atmosphere and cooling rate have also been studied. The change from a slow cooling to a quick cooling procedure after the HT was critical in improving the efficiency of the final device. The absorption at 1000 nm, is only 5% higher after the rapid cooling. The results for both the absorption and cell performance were nominally the same for heat treatments done in air or O_2 atmospheres. On the other hand, a H_2 atmosphere resulted in no additional absorption but also did not produce conductive p-type CdTe satisfactory for cell production.

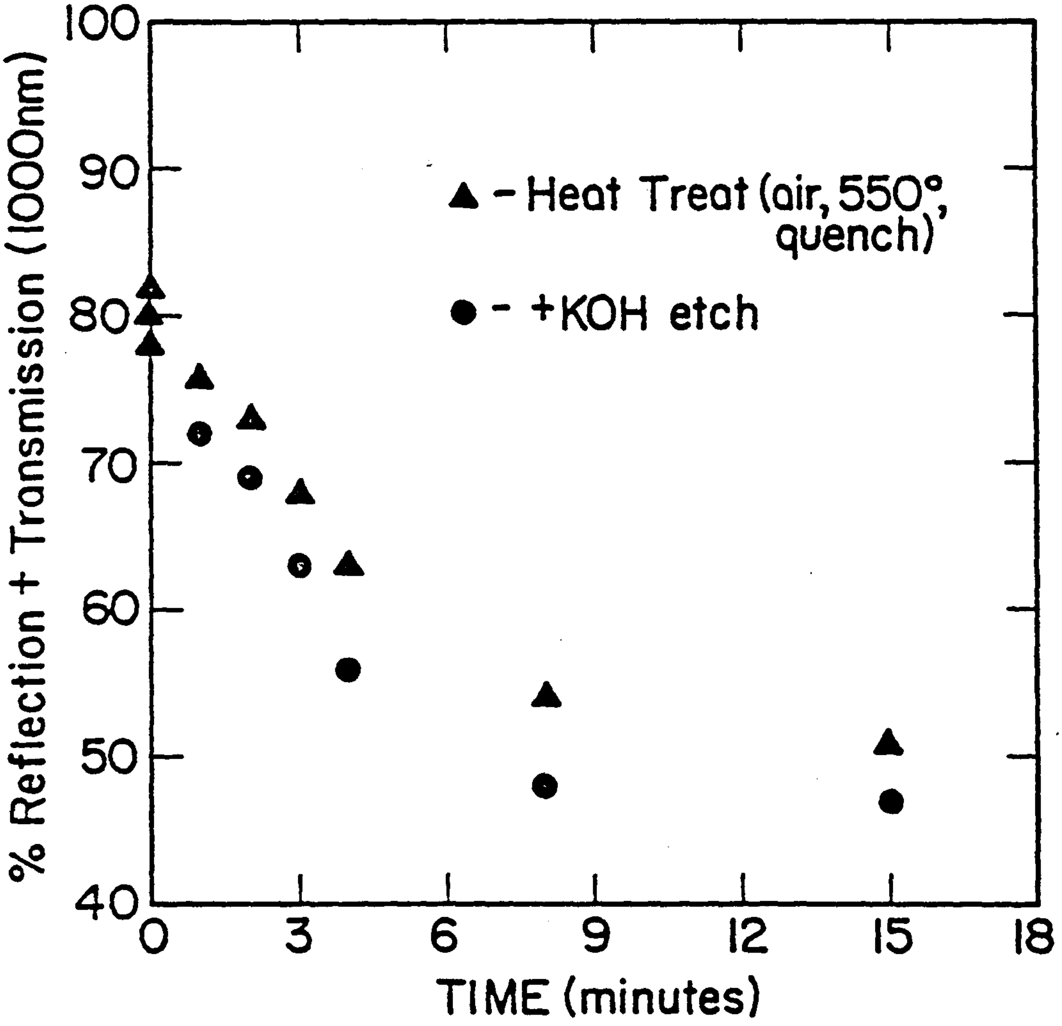

Figure 2.4: Total reflection plus transmission of a CdTe/CdS sample versus heat treatment time at 550°C in air

In addition to optimizing the pre-contact HT to produce the highest transparency cell, a second approach has been to remove surface layers formed by the HT. This would increase the transparency if, as expected, the additional absorption occurs in oxides at the exposed CdTe surface rather than in the bulk CdTe. A number of chemical etches which react with CdTe and remove material from the surface were tried. These included Br_2CH_3OH, HNO_3, HCl, and dichrol^R. None of these, however, succeeded in increasing the transparency of the device.

A more straightforward approach which did increase R+T was mechanical polishing of the CdTe surface. The polishing was done by hand with a 0.05µ particle size alumina powder suspended in H_2O. The average change in thickness was determined from the mass loss to ±0.02µ. Sample 40591.12, with an initial CdTe layer of 2.86µ and R+T = 84% at λ=1000nm was given a 15 minute 550°C HT. It was then polished down in steps of ~0.2µ with R and T measured at each step. The results are shown in Figure 2.4. After removing 0.86µ of the CdTe, R+T was 86% which was comparable to the pre-HT value. Similar results were obtained after an 8 minute HT with R+T comparable to the pre-HT value after ~0.65 µ had been removed.

The two polished 7059/ITO/CdS/CdTe samples were each cut in half. Each piece was etched in a different solution and then a Cu/ITO contact was deposited. The cell results are summarized in Table 2.11. All the cells had curvature in the forward bias region of the cell test I-V curve indicating non-ohmic contacts which caused the low fill factors. For 3 of the 4 samples, however, J_{sc} and V_{oc} were comparable to those obtained on good cells made with the standard process. This suggests that the surface layer formed during the pre-contact HT plays an important role in forming an ohmic contact between the bulk CdTe and the Cu/ITO. An additional aspect of the polishing experiments can be seen in Figure 2.5. There was no change in R+T after removing the first ~0.2µ of CdTe. This suggests the presence of two layers in the CdTe, a transparent top layer and a thicker, partially absorbing layer beneath.

TABLE 2.11

Polished and Etched CdTe/CdS Cell

Sample #	Etchant	Voc (V)	Jsc+ (mA/cm^2)	FF (%)	n (%)
40591.121	4M KOH/30sec	0.568	18.3	31.2	3.7
40591.122	0.1%Br_2CH_3OH/3sec	0.603	19.8	40.8	5.6
40591.231	Basol[1]	0.595	18.4	52.3	6.5
40591.232	Tyan[2]	0.585	12.6	20.5	1.7

1. Basol and Rod, U. S. Patent #4,388,483 - bromine methanol, dichrol, hydrozine

2. Tyan, U. S. Patent #4,319,069 - nitric acid - phosphoric acid

+ELH simulation at 87.5 mW/cm^2; cell temperature 32°C

This two layer structure on the surface of the CdTe was analyzed using: X-ray diffractometry; Auger depth profilometry; and SEM and Optical microscopy of exposed CdTe surfaces and in tapered cross-section samples. The results are summarized below:

X-ray Diffraction

2-theta x-ray diffraction (XRD) scans of CdTe/CdS/ITO layers on 7059 substrates using a scanning diffractometer with Cu K-alpha radiation were performed to determine film orientations and to determine the nature of any surface layers which formed during the 15 minute air heat treatment and during the KOH etch. Other investigators have identified a variety of surface oxides formed during air or oxygen heat-treatments of CdTe, including $CdTeO_3$[20], TeO_2[21-24], Te[21], and CdO[23]. Previously[14] we reported finding $CdTeO_3$ on oxygen heat treated and etched CdTe films on bare 7059, ITO/7059, and CdS/ITO/7059.

The effect of the heat treatment on the CdTe has two aspects: restructuring of CdTe and the appearance of $CdTeO_3$. Table 2.12 summarizes the CdTe and CdS XRD reflections and intensities observed for as-deposited, air heat-treated, and KOH etched CdTe deposited on CdS/ITO/7059.

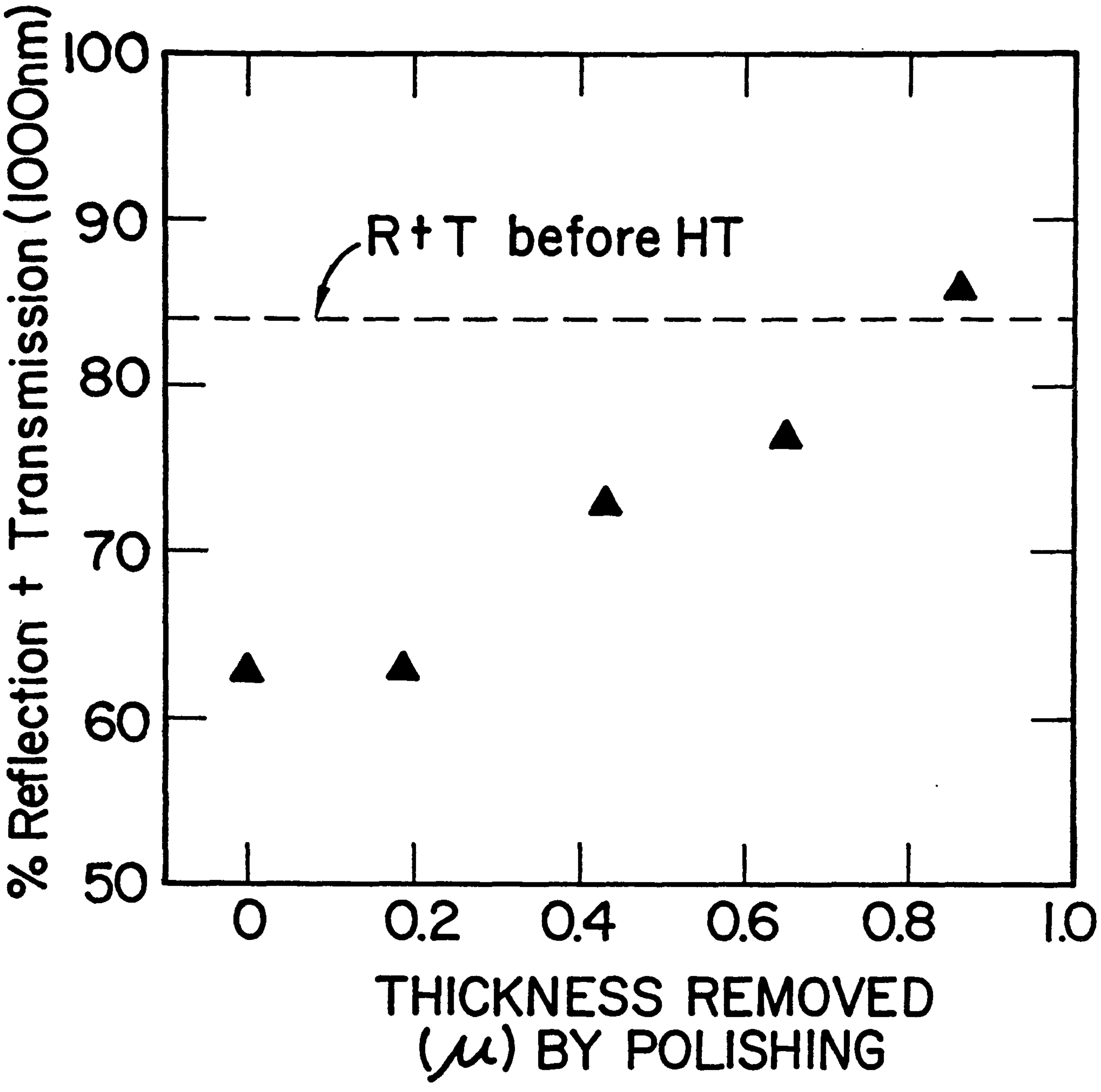

Figure 2.5: Total reflection plus transmission at 1000 nm for a CdTe/CdS sample after 15 minutes heat treatment versus thickness removed.

Table 2.12

X-ray diffraction intensity data for CdTe and CdS in the as deposited, air heat treated, and etched conditions for sample 50238.31.

Film	CdTe Reflections					CdS Reflections			
Random	(111)	(311)	(422)	(511)	(642)	(002)	(200)	(004)	(105)
As-dep	1800	5	12	25	8	245	10	20	15
H. T.	730	115	105	15	12	350	20	30	15
Etched	700	145	160	20	18	360	8	25	15

Significant restructuring of the CdTe occurs during the air heat treatment, a change which was likewise observed on samples which were oxygen heat treated. In the as-deposited and heat treated conditions, the Cu alpha 1 - alpha 2 split in large angle reflections is not observed, indicating a strained CdTe film. After etching, however, the reflections are resolves into alpha 1 - alpha 2 components for angles greater than 34 degrees. This suggests that the KOH etch allows relaxation within CdTe grains. SEM photomicrographs show furrowing and pitting of the CdTe surface after the etch, which is probably the mechanism responsible for the lattice relaxation.

Figure 2.6 shows 2-theta scans of the CdTe (422) peak showing an unresolved peak in as-deposited and heat treated conditions and resolved peaks after KOH etch.

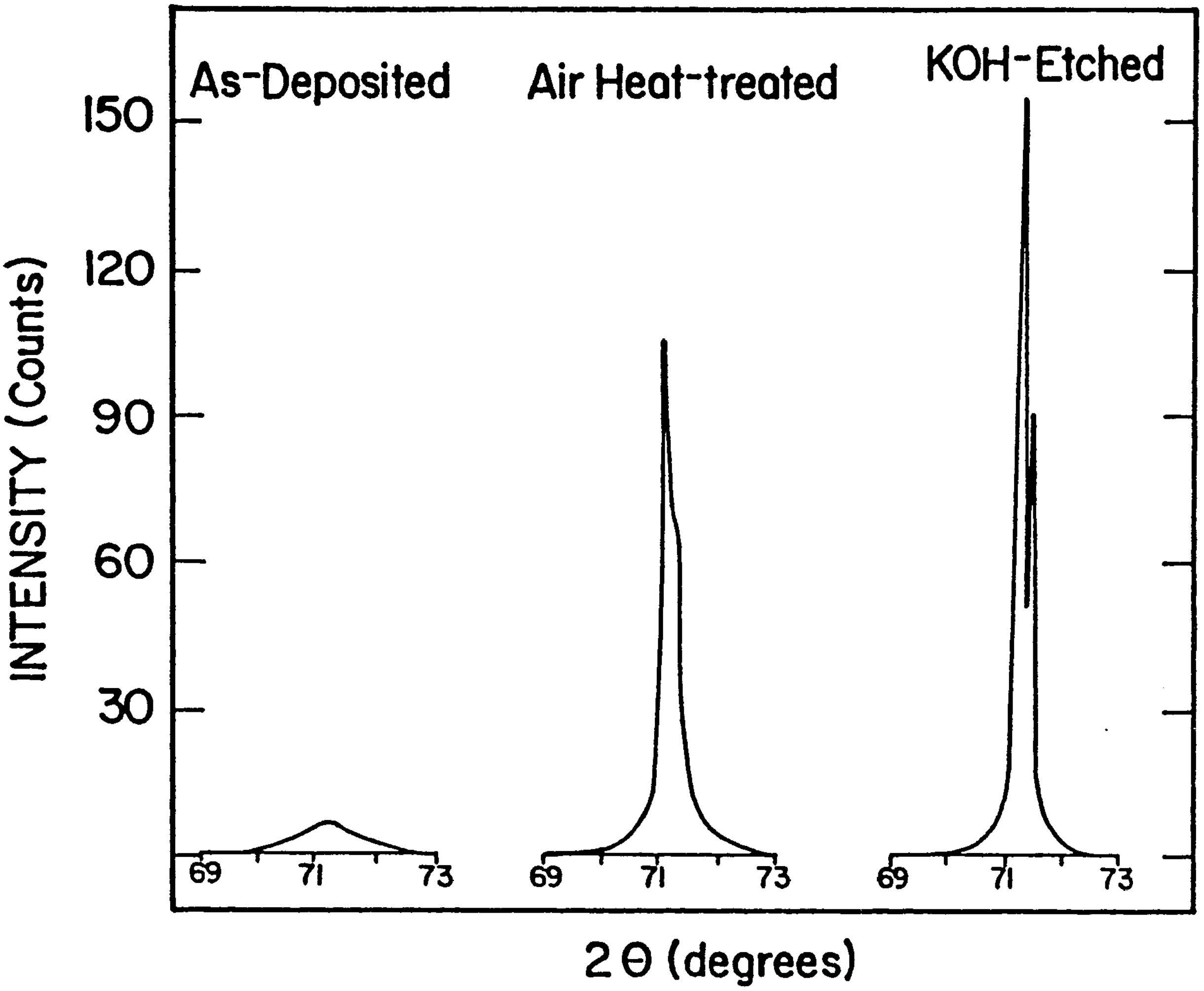

Figure 2.6: XRD scan of CdTe (422) peak showing change in structure after heat treatment and etch.

X-ray diffraction scans following the heat treatment and subsequent etching both showed a significant number of reflections which are indexed as $CdTeO_3$ and summarized in Table 2.13.

Table 2.13
Observed reflections in heat treated and etched CdTe/CdS/ITO attributed to $CdTeO_3$ for sample 50238.311.

$CdTeO_3$			Heat Treated		Etched	
d(A)	I/I1	hkl	d(A)	I (cts)	d(A)	I (cts)
3.573	3	002	3.55	10	ND	
3.173	20	122	3.13	10	ND	
3.011	100	022	3.01	30	3.019	27
2.910	55	220	2.915	5	2.919	9
2.812	45	040	ND		2.829	6
2.685	10	132	2.676	15	ND	
2.632	18	041	2.637	60	ND	
2.525	9	230	ND		2.543	10
2.409	11	311	2.385	5	ND	
1.897	4		1.885	8	ND	
1.786	11		1.788	20	ND	

The KOH etch removes a surface layer as described below. Additional etching in KOH does not remove the remaining $CdTeO_3$, indicative of either preferential etching or a self-limiting reaction between KOH and $CdTeO_3$. Whatever the chemistry, after the KOH etch, electrical contact to the CdTe cell must involve contacting to or through $CdTeO_3$.

An experiment was performed to determine the $CdTeO_3$ layer thickness by measuring mass change of 1" by 1" CdTe/CdS/ITO/7059 structures after H.T. and etch. No mass change was detected following the 15 minute heat treatment but after etching in KOH a mass loss corresponding to a $CdTeO_3$ thickness of 2000A was measured. X-ray diffraction scans of a sample which had been heat treated for 15 minutes, etched in KOH, and then mechanically polished to remove 1000A yielded no $CdTeO_3$ reflections, indicating an upper bound for the $CdTeO_3$ layer thickness of 3000A. Scans for a sample heat treated in air for 4 minutes gave $CdTeO_3$ peaks having 30% the intensity of those found on samples heat treated for 15 minutes. Mechanical removal of 1000A from this sample yielded no $CdTeO_3$ x-ray reflections.

Auger Profilometry

Auger electron spectroscopy was used to determine relative concentrations of Cd, Te, and O in as-deposited, air heat treated, and KOH etched CdTe layers deposited on CdS/ITO/7059 substrates. A comparison was made between samples which were slowly cooled and which were quickly cooled after the heat treatment.

On as-deposited CdTe films, a barely detectable surface oxide is observed. The depth profiles of as-deposited CdTe are very flat with tellurium concentration about five percent higher than the cadmium. An oxygen concentration in the 3 to 5% range is observed in as-deposited films.

On both slow and quickly cooled samples, a substantial oxygen concentration was found which decreased monotonically within the sample. Two regions are identified on heat treated samples: oxygen dominated region and cadmium-tellurium dominated region. In the first region, oxygen comprises nearly fifty percent of the layer. The Auger tellurium peaks (E=482 and 491 eV) in both regions are switched in intensity compared to peaks measured in the bulk of the film due to a change in the tellurium valence state in the presence of oxygen. There is little difference between samples which were slow cooled and samples which were quickly cooled.

After etching in KOH, there appears to be little or no oxygen dominated region. An increase in cadmium to tellurium concentration is also seen. The slowly cooled sample shows little oxygen and relatively flat profiles for cadmium, tellurium, and oxygen. The quickly cooled sample shows considerable oxygen down to the depth where the cadmium to tellurium concentrations return to those of bulk as-deposited CdTe.

SEM and Optical Cross-Section Microscopy

Oblique-angle cross-sections of as-grown, heat treated, and etch CdTe/CdS films were prepared by potting the samples at a 5° angle in an epoxy matrix. A cross section of the CdTe surface is obtained by mechanically polishing the samples. See Figure 2.7.

The three optical micrographs shown in Figure 2.8 show the formation of a thin layer on the surface of CdTe as well as formation of inclusive dark regions after the 550°C air heat treatment. Subsequent etching in KOH is clearly shown to remove this top layer, but the optically dark regions remain. The density of the dark regions decreases to zero well within the first micron of the sample. These results are consistent with the Auger data and the optical results on the mechanically polished sample showing a two layer surface structure.

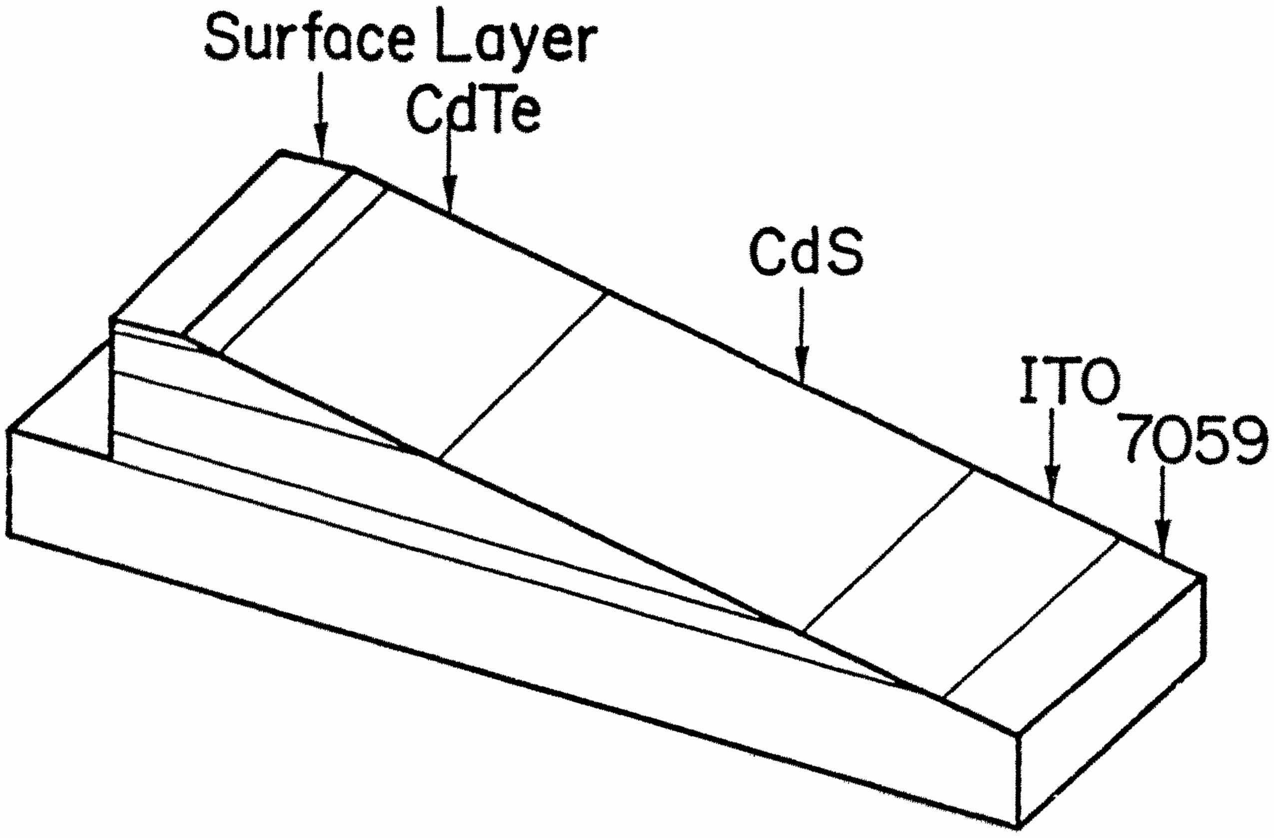

Figure 2.7 Schematic of oblique-angle cross section of CdTe/CdS/ITO/7059.

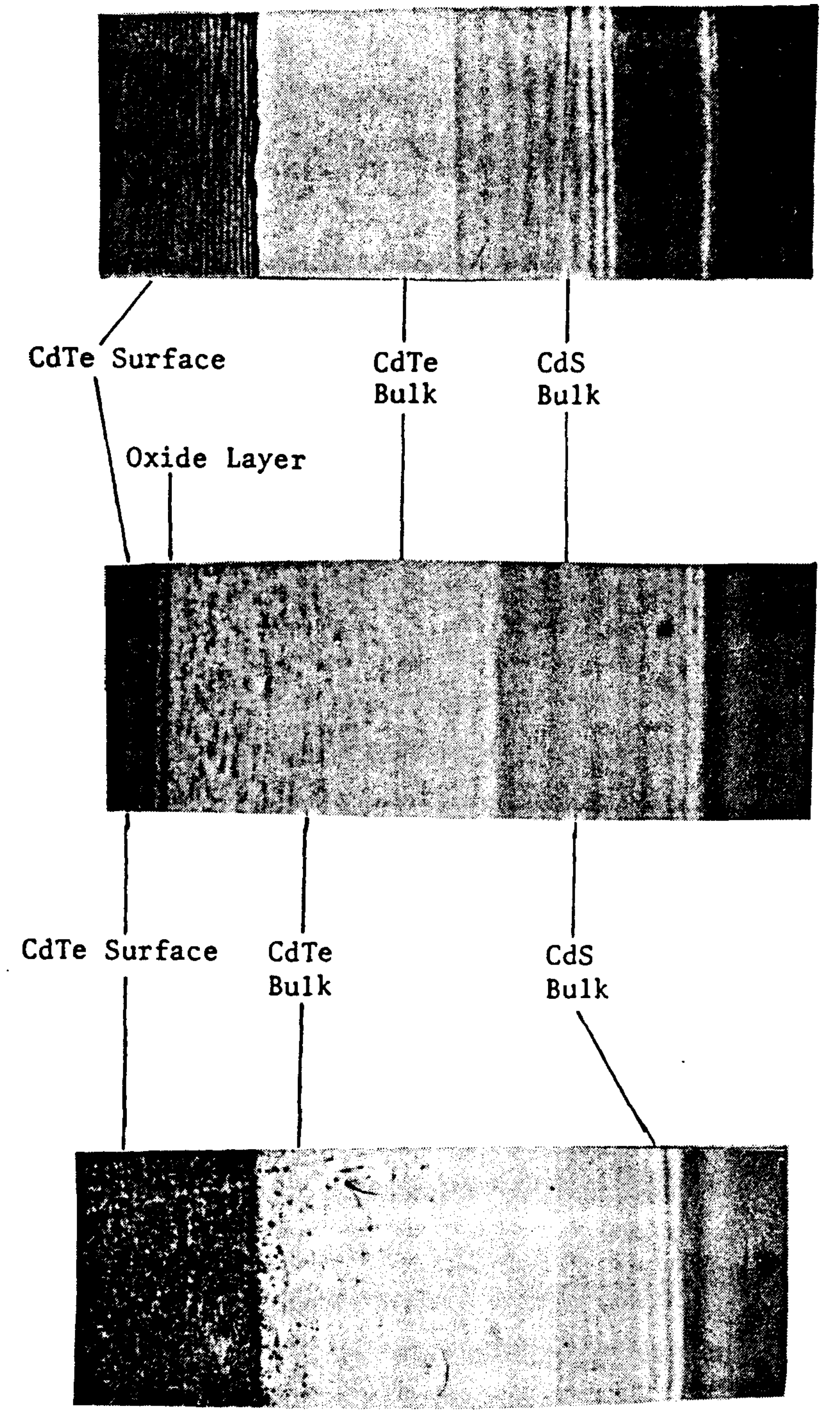

(a) As-deposited

(b) After 550°C air heat treatment

(c) After subsequent KOH etch

Figure 2.8 Optical micrographs of oblique-angle cross-sectioned CdTe/CdS/ITO/7059 under various conditions.

2.2.4 Cell Results and Device Analysis

Best Cell Results

Table 2.14 summarizes the best I-V results for all 2.5x2.5 cm^2 7059/ITO/CdS/CdTe/Cu/ITO samples processed having a device with efficiency over 8%. (All cells had a Cu/ITO contact). The short circuit currents and fill factors are as high as those reported for CdTe/CdS cells with n>10% [16,17,25] but the voltages are, in general, more than a tenth of a volt lower. The low V_{oc} is probably due to interface recombination (discussed below) and/or a high CdTe resistivity (8>10^{3}Ω-cm). Early in the program, CdTe/CdS devices with FF>70% were made having J_{sc} ~ 14 mA/cm^2 and V_{oc} ~ 0.57 volts. These are believed to be the highest fill factors measured for CdTe/CdS cells.

Table 2.14
CdTe/CdS Cells with ^{n}>8%

Sample #	V_{oc} (V)	$J_{sc}$$^{+}$ (mA/cm^2)	FF (%)	EFF (%)
40535.11	0.6271	18.26	61.90	8.10
40572.121	0.6474	20.11	55.17	8.21
40572.122	0.6510	19.64	57.02	8.33
40582.311	0.6173	18.92	63.89	8.53
40584.111	0.6180	20.82	56.44	8.30
40585.231	0.6115	20.50	60.54	8.67
40586.111	0.6628	19.78	57.32	8.59
40597.131	0.6057	19.20	60.92	8.10
40597.132	0.6239	19.45	59.14	8.20

+ ELH simulation at 87.5 mW/cm^2; cell temperature 32°C

A limited number of cells were made using (CdZn)Te films with Eg from 1.55 to 1.68eV. The best cell results were obtained on low Zn content films with Eg~1.55 eV. The highest efficiency was only 3.7% with J_{sc} ~ 12 mA/cm^2 and V_{oc} ~ 0.57. It is insignificant to note that none of these devices showed an increase in V_{oc} due to the wider bandgap. No attempt was made to optimize the device fabrication process for (CdZn)Te cells.

Effect of heat treatment:

As previously reported[14], a high temperature (T>500°C) heat treatment in air or O_2 was needed to increase the p-type conductivity of the CdTe which resulted in an increase in V_{oc}. A further increase in V_{oc} was obtained by increasing the heating and cooling rate used for the heat treatment. Appendix 2 describes the procedures used for the heat treatments.

Increasing the heating and cooling rate from 10^2°C/min to 10^3°C/min, for the CdTe/CdS samples, an increase in V_{oc} of 50-100 mV was obtained. Table 2.15 summarizes I-V results for CdTe/CdS cells made from the two CdTe deposition using the different heating and cooling rates. All cells have a transparent Cu/ITO contact.

TABLE 2.15
Effect of Cooling Rate on V_{oc}

Sample #	V_{oc} (V)	$J_{sc}{}^{+}$ (mA/cm^2)	FF (%)	η (%)	H.T.
40533.21	0.491	15.8	47.9	4.3	slow
40533.32	0.605	18.0	57.0	7.1	rapid
50236.13	0.513	16.1	50.0	5.7	slow
50236.23	0.583	16.8	51.9	5.2	rapid

+ ELH simulation at 87.5 mW/cm^2; cell temperature 32°C

An increase in V_{oc} was seen for all cells using the rapid heat treatment along with a small increase in FF and J_{sc}. The rate of heating and cooling effects both the contact and bulk properties of the CdTe as discussed below.

To investigate the effect of HT time on cell performance, five 7059/ITO/CdS/CdTe samples from the same CdS and CdTe depositions were made into cells after being heat treated from 1 to 8 minutes at 550°C in air and rapidly cooled. The samples were then etched in 4 molar KOH for 30 seconds at 60°C and cell areas were delineated using Cu/ITO transparent contacts. Post-contact heat treatments at 150°C and 200°C were used to optimize the cells' performance by improving the ohmicity of the contact. The best cell results in each case are summarized in Table 2.16. As the pre-contact HT time increased from 1 to 4 minutes V_{oc}, J_{sc} and the FF all increased consistent with a decrease in the CdTe bulk resistivity (Table 2.7) while no significant change was seen beyond 4 minutes. Results from other sets of cells confirm that heat treatments from 4-15 minutes yield comparable final cell results. Therefore, based on these results and the optical analysis, Section 2.2.3, the optimum time for the 550°C pre-contact HT is 4 minutes.

TABLE 2.16

Effect of 550° HT time on CdTe cell results.
All samples with Cu/ITO contacts optimized with
post-contacting HT.

Sample #	H.T. time(min) 550°C, air	V_{oc} (V)	J_{sc} + (mA/cm^2)	FF (%)	η (%)
40597.212	1	0.53	13.4	45	3.6
40597.312	2	0.57	14.4	64	6.0
40597.322	4	0.63	17.2	58	7.1
40597.132	4	0.62	19.5	59	8.2
40597.12	8	0.60	17.6	65	7.9

+ ELH simulation at 87.5 mW/cm^2; cell temperature 32°C

Series Resistance Analysis

The I-V characteristics of three CdTe/CdS cells were analyzed as a function of light intensity to determine A-factor, J_o, and the light dependent and independent series resistance. Two samples underwent the rapid heat treatment sequence while one received the slow cool treatment. ITO/Cu contacts were used on two sample (quick and slow heat treatment) and one had an Au contact (rapid heat treatment).

The method of Swartz[26] was used to separate the light independent, Rc, and the light dependent, R_L, series resistance from plots of $\left.\frac{dV}{dJ}\right|_{V=Voc}$ vs 1/Jsc. The intercept yields R_c directly while the slope (ΔV) yields R_L (photoconductive) from

$$\left.\frac{dV}{dJ}\right|_{V=Voc} = Rc + \frac{V}{Jsc}$$

$$V_L = V\left(\frac{JL}{J_{sc}}\right) - \frac{AkT}{q}$$

$$R_L = \frac{V_L}{J_L}$$

where V_L is the voltage drop across the photoconductive layer.

Plots of $\left.\frac{dv}{dJ}\right|_{V=Voc}$ vs. $1/J_{sc}$ for the three samples are shown in Figure 2.9 and Table 2.17 summarizes the results.

Table 2.17
Series Resistance of CdTe/CdS with Different Contacts and Heat Treatments

Sample #	40533.12	40533.32	40533.21
Heat treatment	rapid	rapid	slow
CdTe contact	Au	Cu/ITO	Cu/ITO
Voc(V)	0.574	0.591	0.488
Jsc(mA/cm^2)	17.9	18.6	15.9
FF(%)	53.4	55.7	43.7
A	1.73	1.71	2.33
Jo(mA/cm^2)	6×10^{-5}	$<10^{-4}$	5×10^{-3}
R_C(Ω-cm^2)	6.4	1.8	7.4
R_L(Ω-cm^2)	1.5	1.6	1.9

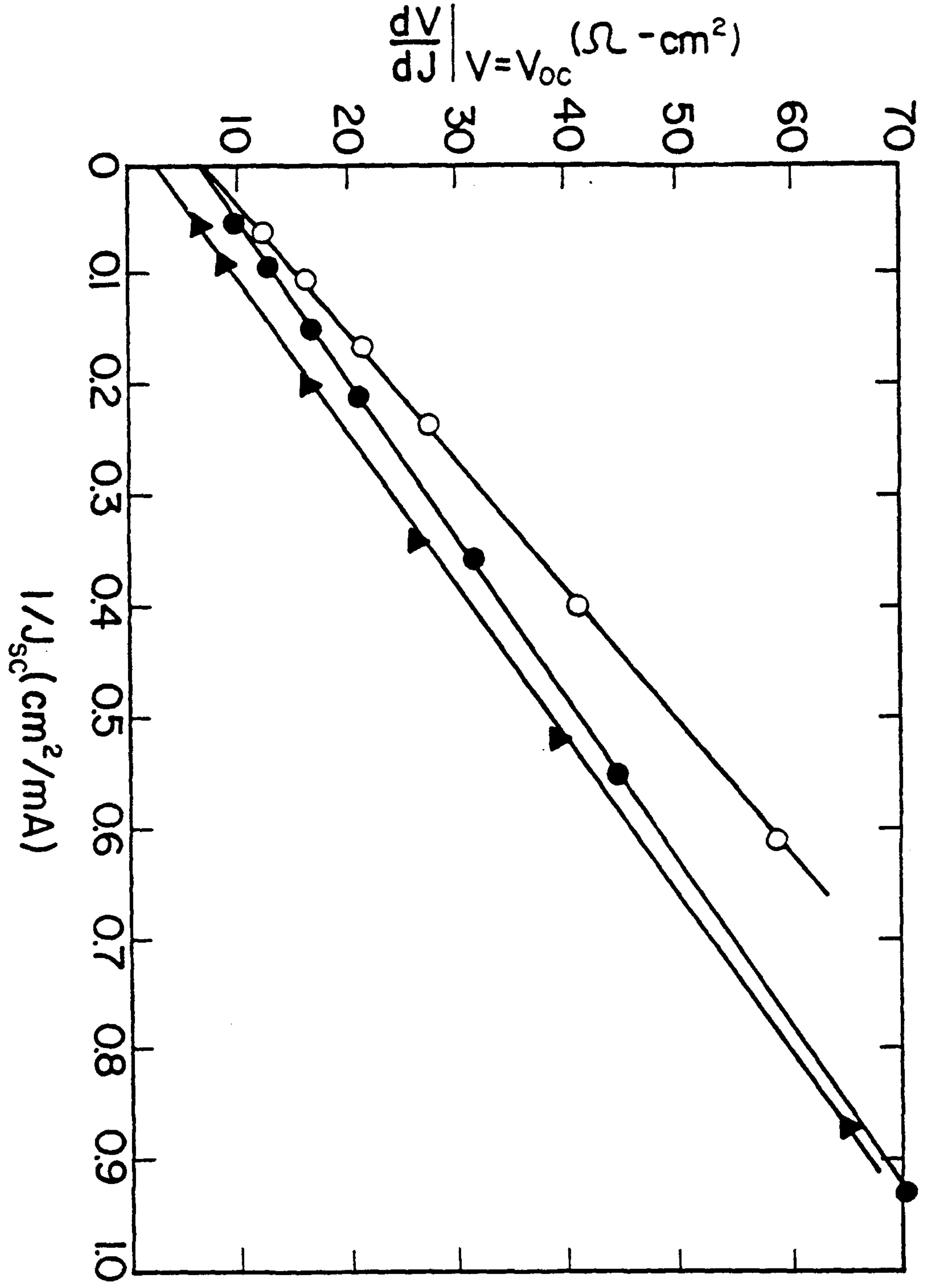

Figure 2.9: Plot of $\frac{dV}{dJ}\Big|_{V=V_{oc}}$ vs $1/J_{sc}$ used to separate the light dependent and light independent series resistance.

The combination of the rapid heat treatment with the Cu/ITO contacts yields the highest FF and lowest resistance, primarily through the contact resistance, R_c. Since R_L is nearly the same for all cells, the photoconductivity of the CdTe is independent of the type of heat treatment and contact. This suggests that diffusion of Cu or Au into the CdTe at this temperature-time cycle does not change the photoconductivity of the CdTe. Further, the difference in A and J_o for the rapid and slow heat treatments indicates that the heating and cooling rate reduces the recombination in the devices. Thus, the rapid heat treatment effects both the contact and junction properties.

Dark Diode Analysis

Dark J-V measurements as function of temperature were made and analyzed on several devices to determine J_o, B, A, J_{oo}, and E_a from:

$$J=J_o \exp\left[\left(B+\frac{q}{AkT}\right)V\right]$$

and

$$J_o= J_{oo} \exp(-Ea/kT)$$

where A - standard A-factor for thermally excited process
B - tunnelling parameter
E_a - activation energy

The CdTe films used for these devices were deposited at substrate temperatures from 200 to 300°C at different deposition rates. The results of the measurements are summarized in Table 2.18.

Table 2.18
Dark Diode Analysis of CdTe/CdS Cells

Sample #	A	B (V^{-1})	J_o (mA/cm^2)	J_{oo} (mA/cm^2)	Ea (eV)	V_{oc} (V)
40537.23	4.6	10.2	$1.5X10^{-5}$	7.7×10^{7}	0.76	0.63
40544.31	2.8	7.8	$4.5X10^{-5}$	$9.7X10^{7}$	0.74	0.56
40545.12	2.9	57	$4.4X10^{-5}$	$2.1X10^{8}$	0.76	0.57
40551.23	710	~18.8	$3.6X10^{-5}$	$7.9X10^{6}$	0.68	0.60

The results indicate that tunneling is a significant contribution to the dark diode current transport. The J_o values obtained are comparable to J_o obtained at room temperature by varying light intensity (Table 2.9). The values for E_a are in the same range as those reported by Isett,[27] E_a = 0.71 eV, and by Werthen [28], E_a = 0.76 eV. Thus, the low V_{oc} results from high J_{oo} (10^{7} to 10^{8} mA/cm^2) which is consistent with either tunneling or interface recombination. Attempts to modify the CdTe-CdS interface by etching the CdS surface thermally or with HCl prior to the CdTe deposition do not change the V_{oc} or overall cell performance for IEC cells.

Spectral Response

Spectral response measurements have been made on 12 cells from 8 different samples, as a function of voltage and light bias. The short circuit currents of these devices ranged from 7.5 to 18 mA/cm^2. The following results were obtained:

1. There is little or no change in the shape of the spectral response curve with either voltage or light bias - i.e., the spectral response increases or decreases uniformly at all wavelengths. Figure 2.10 shows a typical spectral response at different bias condition.

2. For samples with low Jsc (<16mA/cm^2) the loss in current is due to a reduction in the response at the shorter wavelengths (<700nm). Figure 2.11 and 2.12 show the normalized spectral response curves for four different cells having J_{sc} ranging from 7 to 14.5 mA/cm^2 at 0.0V and -1.0V bias under ELH illumination. The loss in response at λ<700nm could be due to variations in optical generation or possibly the formation of a buried junction.

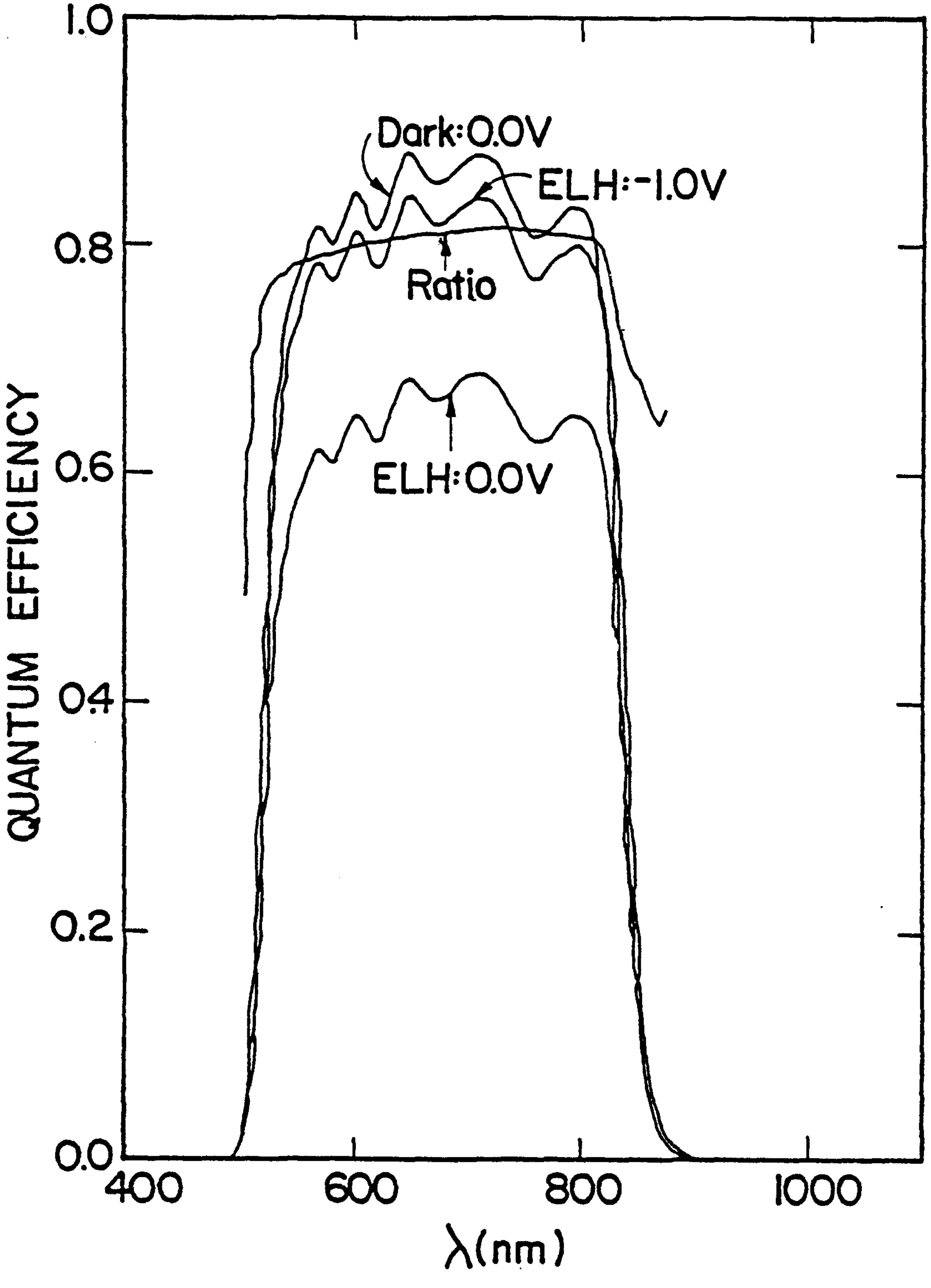

Figure 2.10: Spectral responses at different bias conditions for a CdTe/CdS cell.

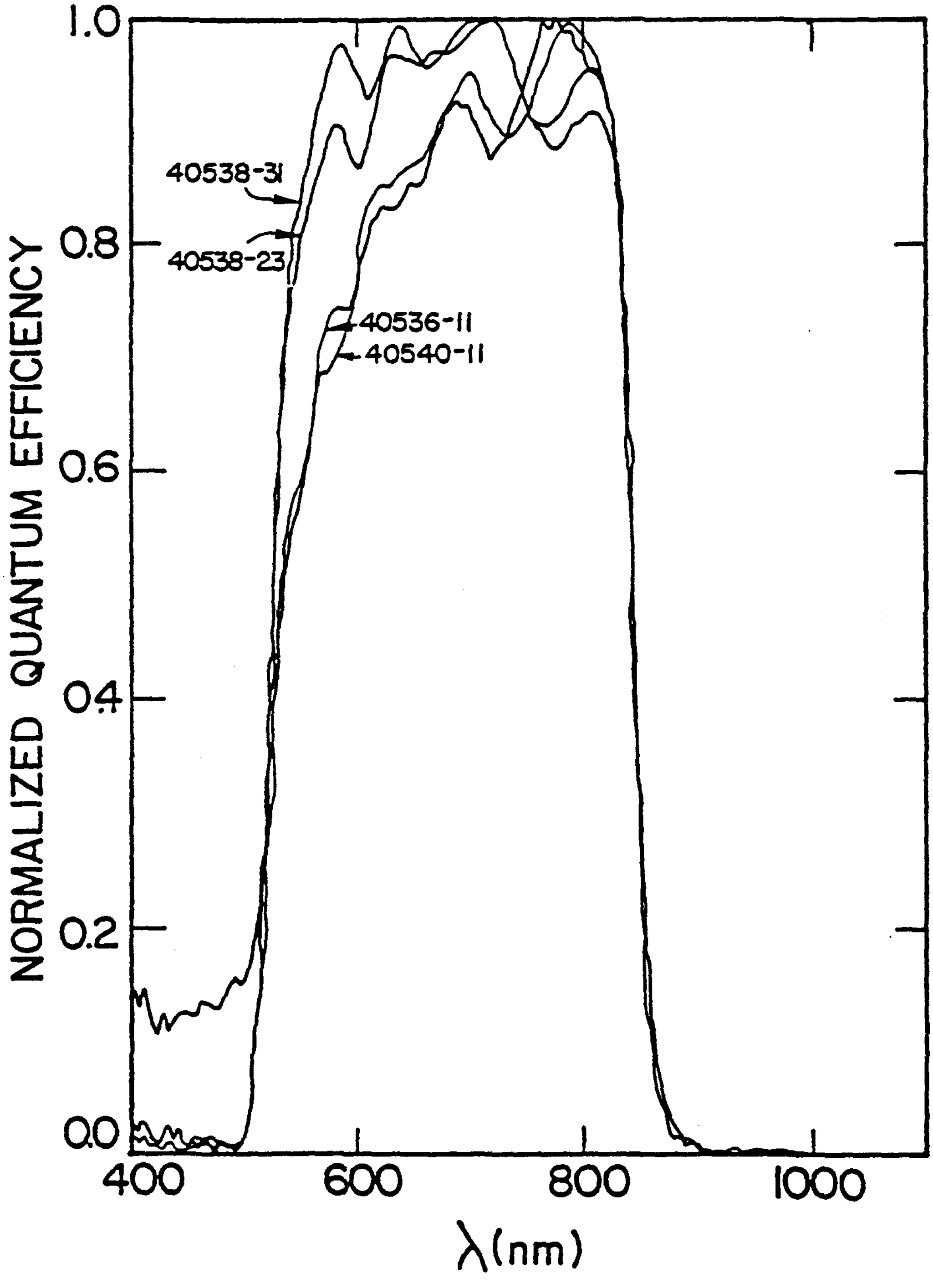

Figure 2.11: Spectral response at 0.0V bias under ELH illumination for four CdTe/CdS cells with J_{sc} from 7 to 14.5 mA/cm^2.

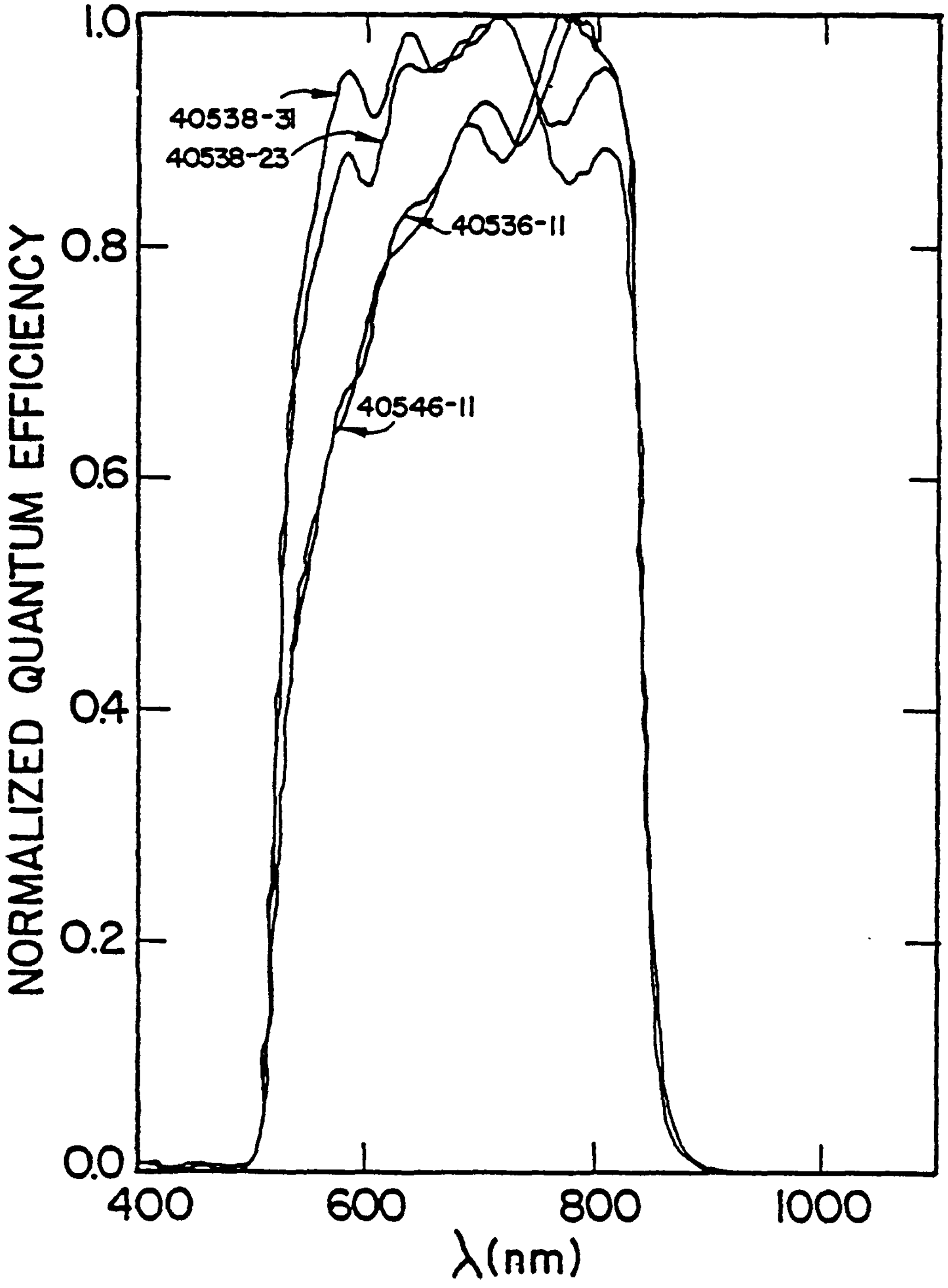

Figure 2.12 Spectral response at −1.0V bias under ELH illumination for four CdTe/CdS cells with J_{sc} from 7 to 14.5 mA/cm².

SECTION 3.0
TANDEM CELL DEVELOPMENT

3.1 MONOLITHIC $CuInSe_2$ - CdTe TANDEM CELL

Monolithic CdTe/CdS: $CuInSe_2$/CdS tandem cells were produced by a sequential deposition process. Efficiencies were generally low, primarily due to a contacting problem with the CdTe/CdS cell. During much of the contract attention was focussed on improving the individual junctions and a relatively small number of tandem structures were actually manufactured. Progress on the CdS/CdTe cell has been the main obstacle to further tandem cell improvement.

Cell Processing

The tandem cells were produced by depositing the CdS/CdTe cell on top of an existing CdS/$CuInSe_2$ cell. The 1 x 1 inch 7059/Mo/$CuInSe_2$/CdS substrate layer was coated with an ITO layer followed by a 20-50 Å layer of Cu. Ni bus bars were first deposited on the top surface of the CdS layer to provide a contact to the interconnect for individual cell testing. The CdTe layer was then deposited and heat treated, generally for two hours at 350°C. The devices were completed by the deposition of about 1.5 µm of undoped CdS followed by Ni bus bars and a final ITO layer.

An array of 12 tandem cells were delineated by a photolithography and etching process. A considerable amount of difficulty was encountered in trying to etch through the ITO interconnect layer. ITO layers which have not been heat treated etch readily in the cold HCl that is used for individual single junction cell delineation. However, after the heat treatment given the CdTe layer prior to the final CdS layer, it was shown that the ITO crystallizes and becomes much more resistant to HCl etching. A technique which allows delineation of the cells has been developed in which the ITO interlayer is connected to a Zn electrode during the HCl etching process. The resulting galvanic effect considerably enhances the etching rate.

Material Analysis

A major problem in making tandem devices is the surface structure of the $CuInSe_2$/CdS cell which causes problems in fabricating the devices and reduces performance of the cells. Large protuberance, 5-10 microns above the $CuInSe_2$/CdS cell surface, caused shorted tandem cells due to etching down the protuberance during delineation of the devices. By modifying substrates temperature, during the $CuInSe_2$ deposition some improvement in surface structure was achieved.

Cell Results

Table 3.1 and Figure 3.1 show I-V test results for the best efficiency devices produced. At this stage of device development, it is clear that a number of effects were substantially limiting device performance. The total current flow through the tandem is being limited by transmission through the upper layers of the cell. Short circuit currents in the $CuInSe_2$/CdS junction, tested through the CdTe/CdS cell have only reached 10 mA/cm². Overall performance of the CdTe/CdS junction is well below optimum and as this junction is improved, tandem performance will benefit directly. Figure 3.2 shows the individual spectral response of the junctions in the tandem configuration using the accessible terminal to the ITO/Cu interconnect. There is some response of the $CuInSe_2$ junctions at photon energies above the CdTe band gap.

Table 3.1
I-V Results of Tandem and Individual Solar Cells

Device	V_{oc} (V)	J_{sc}^{+} (mA/cm²)	FF (%)	Eff (%)
Tandem	0.792	6.7	49	3.0
(CdHg)Te	0.465	9.7	36	1.9
$CuInSe_2$	0.32	6.3	51	1.2
Tandem	1.02	6.5	40	3.0
CdTe	0.68	8.3	30	1.9
$CuInSe_2$	0.33	6.1	46	1.1

+ ELH simulation at 87.5 mW/cm²; cell temperature 32°C

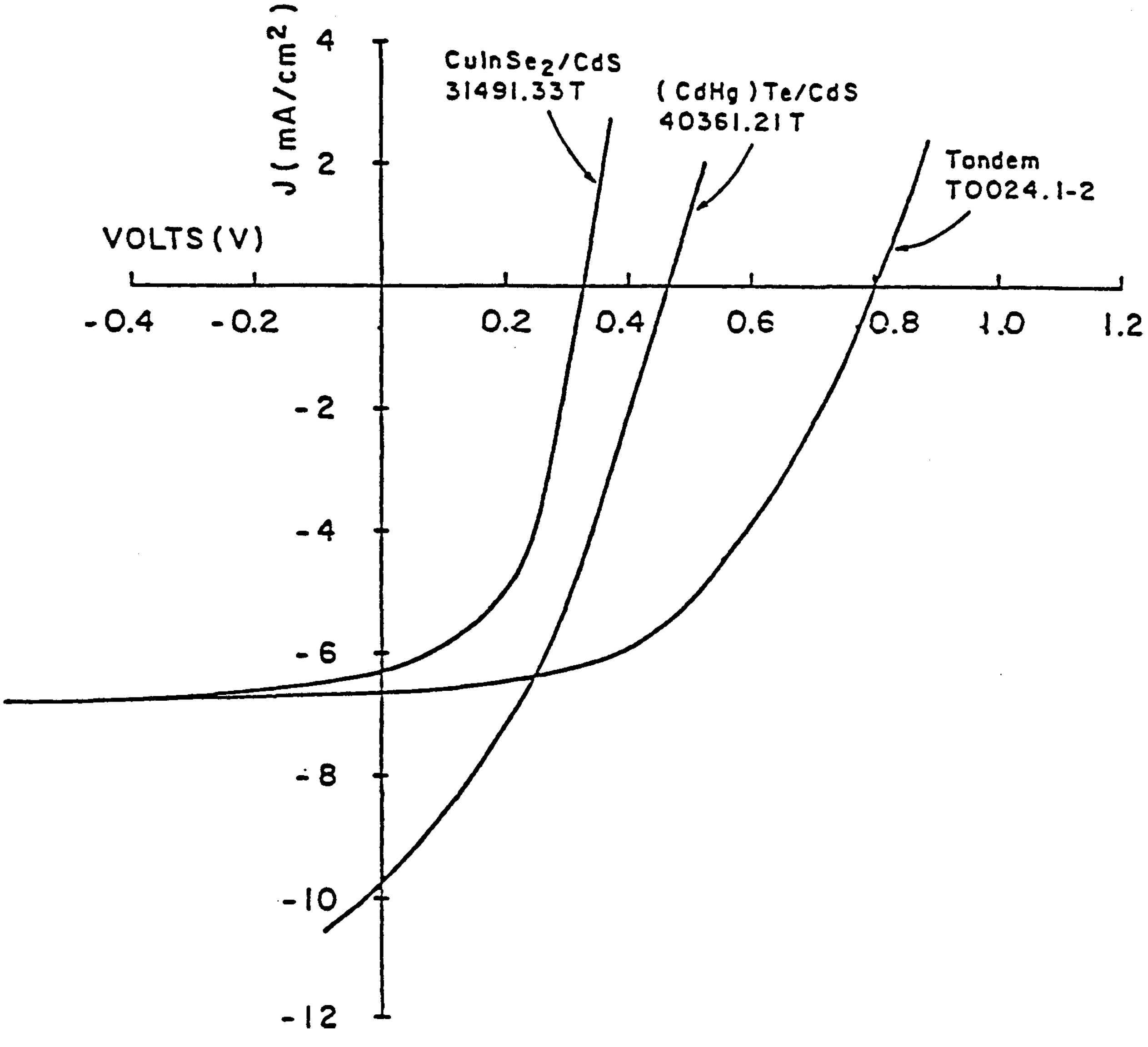

Figure 3.1: I-V curves for $CuInSe_2$-CdTe tandem cell and the individual junctions.

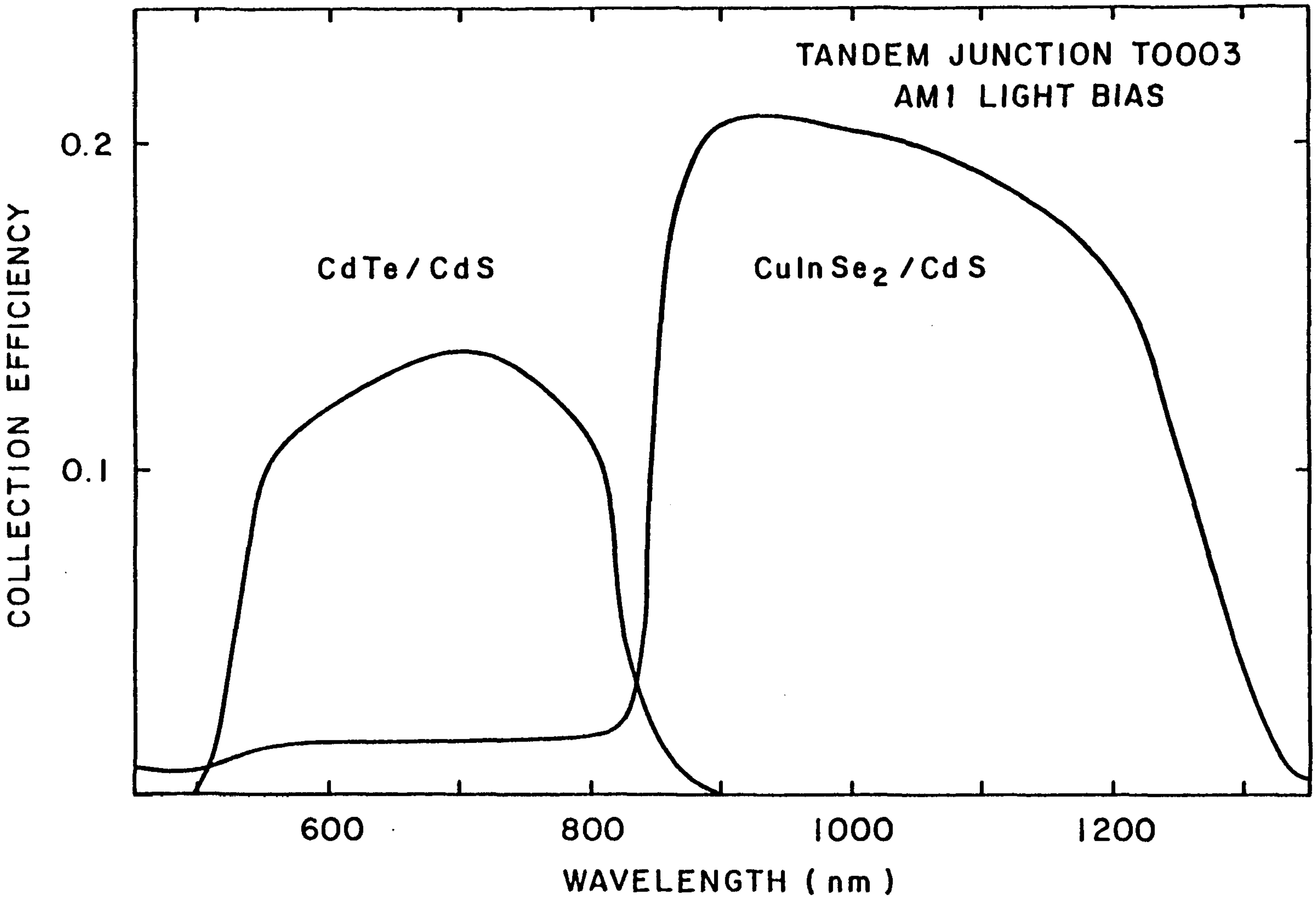

Figure 3.2: Spectral response of individual junctions in a tandem cell of 0.0 volts bias with ELH illumination.

3.2 PRELIMINARY PROCESS DESIGN

Preliminary process designs for four and two terminal tandem devices have been carried out. Figures 3.3A through 3.3D and 3.4A through 3.4D summarize the results of these designs for two terminal and four terminal devices, respectively. These preliminary process designs are based on what has been achieved on a laboratory scale. Detailed designs of a commercial scale process must rely on economic evaluation of the deposition steps within the context of the entire module assembly and targeted consumer market. Such an economic evaluation is beyond the scope of this work. However, an example of design requirements for commercial scale production of economical photovoltaic modules is given by Russell et al.[29]. The preliminary process design shown in Figures 3.3A through 3.3D and 3.4A through 3.4D can best be used to identify specific process steps where further research is required. Specifically, further research is required for key process steps that:

- could limit the overall process capacity
- could require large amounts of materials as a result of low utilization.
- are not optimized on a laboratory scale
- operate under processing conditions which may be technologically difficult or expensive.

The specific process steps that require further research include:

- CdTe deposition step. This is the capacity limiting step in both processes and is the least optimized on the laboratory scale in terms of the single junction device performance and material deposition. However, it is known that single phase CdTe can be deposited at much higher rates for the low substrate temperatures indicated in the preliminary process design. High cell efficiencies at high deposition rates (>1 μm/min) have been demonstrated [17] but at substrate temperatures that may destroy the material properties and device performance of the preceding layers for a two terminal structure.
- $CuInSe_2$ deposition step. On a laboratory scale, the single junction device performance and deposition rate is adequate. However, the high copper and indium source temperatures may require development of alternative techniques to resistance heating.

- Contacting CdTe. The material system and resulting device properties have not yet been optimized on a laboratory scale. The processing necessary, however, does not appear to be a problem.

- Heat treatments. This is a very important step for optimizing the device performance. The detailed effects of heat treatments on the material properties are unknown but may be of little importance from a processing point of view as long as the effects on device performance are reproducible and uniform. The effects of heat treatments on $CuInSe_2$ single junction device performance has been discussed by Birkmire et al.[3]. If the optimal heat treatment times were to vary across a large area substrate then a significant quality assurance problem for monolithically integrated submodules would result.

In order to address these processing problems and to collect the necessary information for a detailed process design, it is desirable to quantify the important equilibrium and rate processes. This is best accomplished by using verifiable first order mathematical models. In this way, issues such as depletion of raw materials, generation of undesirable side products, utilization of raw materials, and deposition uniformity, which may not be important on a laboratory scale can be addressed during the detailed preliminary design. Verified first order models for the deposition of two of the active semiconductor layers - CdS and CdTe - have been published[30,31]. A verified model for $CuInSe_2$ depositions does not exist though one has been proposed[32].

Whatever technique is used for depositing $CuInSe_2$, a first order model is needed to develop designs for effective management of by-products, effluents and waste streams. The preliminary process designs shown in Figures 3.3A through 3.3D and 3.4A through 3.4D are self-explanatory. This preliminary design is only one example of many possibilities. A number of alternate deposition techniques could be used for the various layers. The best technique for any one layer will depend on economics and compatibility with techniques and materials used in the preceding and successive layers. Material consumption and utilization (Figures 3.3C and 3.4C) are estimates based on conceptual designs for large area CdS and CdTe depositions and are the best plausible values that are considered as achievable.

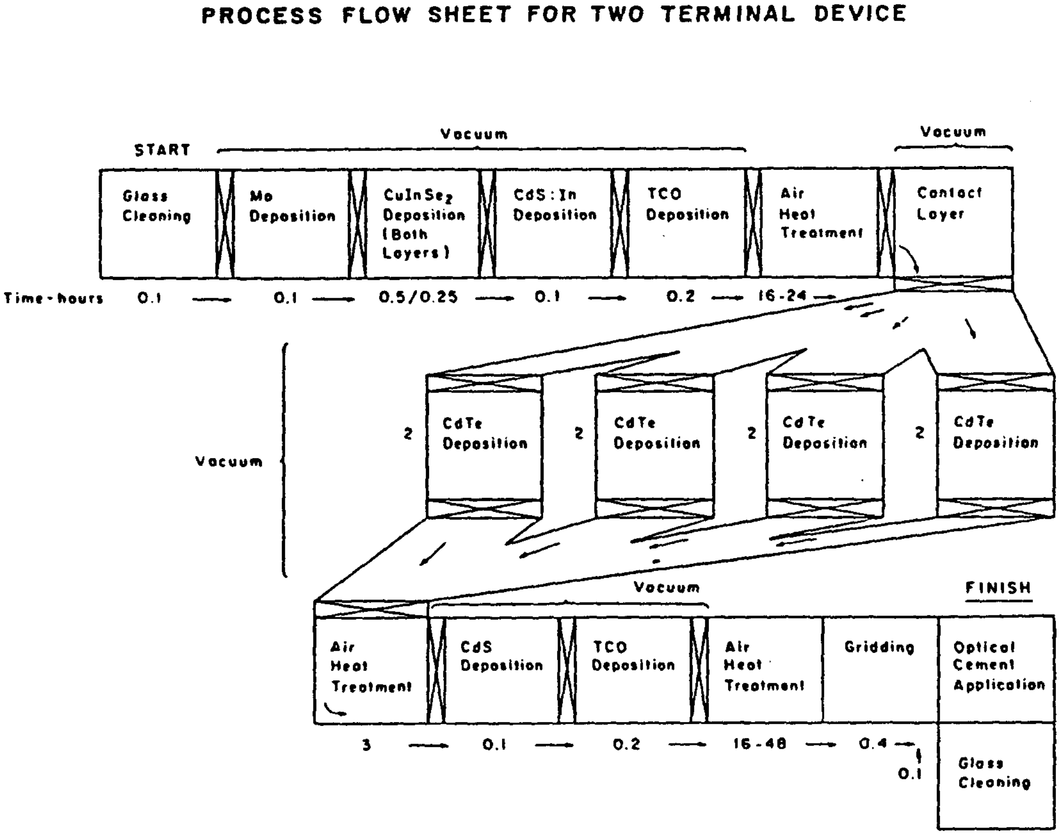

Figure 3.3a Process Flow Sheet for Two Terminal Device

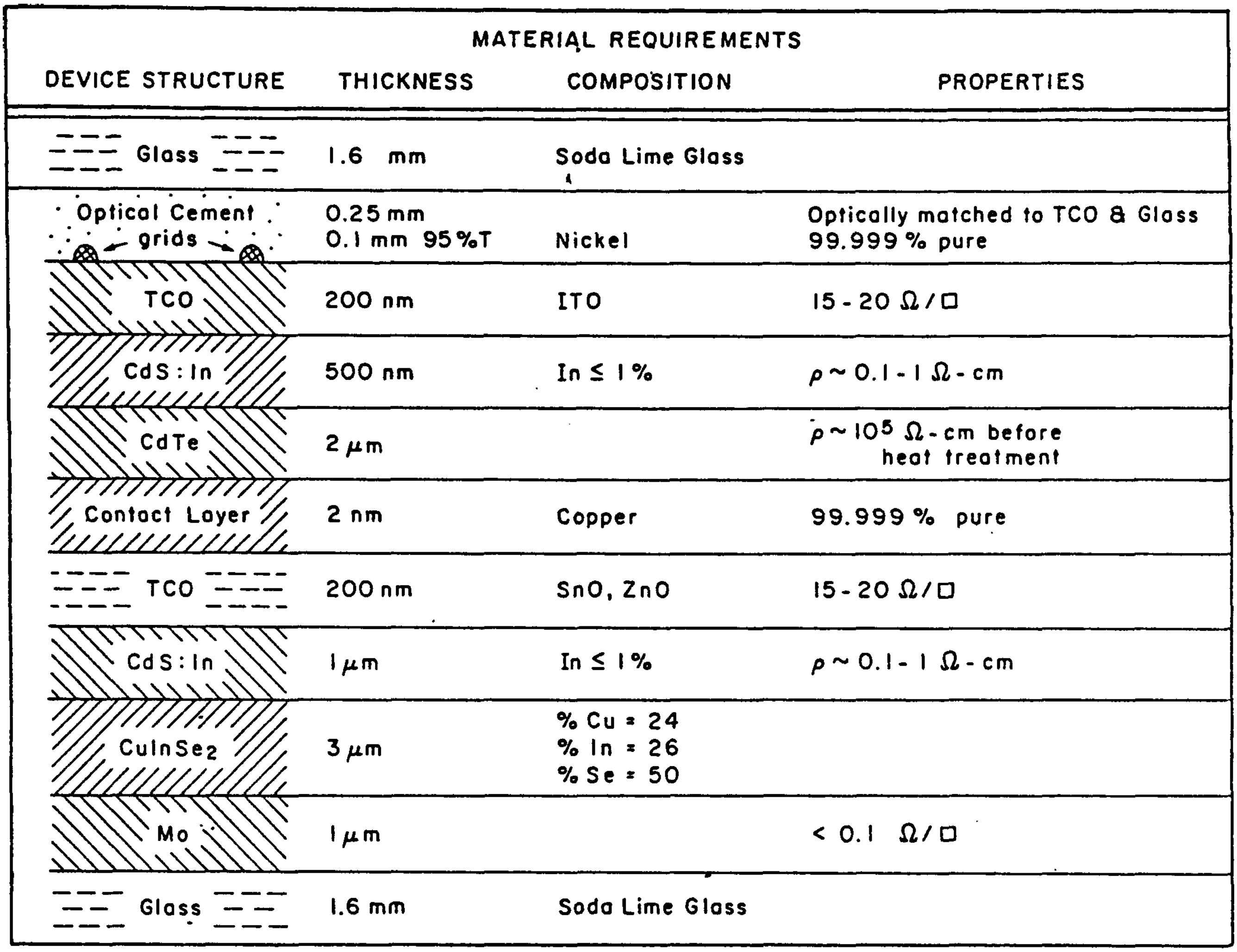

	MATERIAL REQUIREMENTS		
DEVICE STRUCTURE	THICKNESS	COMPOSITION	PROPERTIES
Glass	1.6 mm	Soda Lime Glass	
Optical Cement grids	0.25 mm 0.1 mm 95%T	 Nickel	Optically matched to TCO & Glass 99.999 % pure
TCO	200 nm	ITO	15 - 20 $\Omega/\square$
CdS : In	500 nm	In ≤ 1 %	$\rho \sim 0.1 - 1\ \Omega\text{-cm}$
CdTe	2 μm		$\rho \sim 10^5\ \Omega\text{-cm}$ before heat treatment
Contact Layer	2 nm	Copper	99.999 % pure
TCO	200 nm	SnO, ZnO	15 - 20 $\Omega/\square$
CdS : In	1 μm	In ≤ 1 %	$\rho \sim 0.1 - 1\ \Omega\text{-cm}$
CuInSe$_2$	3 μm	% Cu = 24 % In = 26 % Se = 50	
Mo	1 μm		< 0.1 $\Omega/\square$
Glass	1.6 mm	Soda Lime Glass	

Figure 3.3b Two Terminal Tandem Device - Design Basis

MATERIAL CONSUMPTION FOR TWO TERMINAL DEVICE

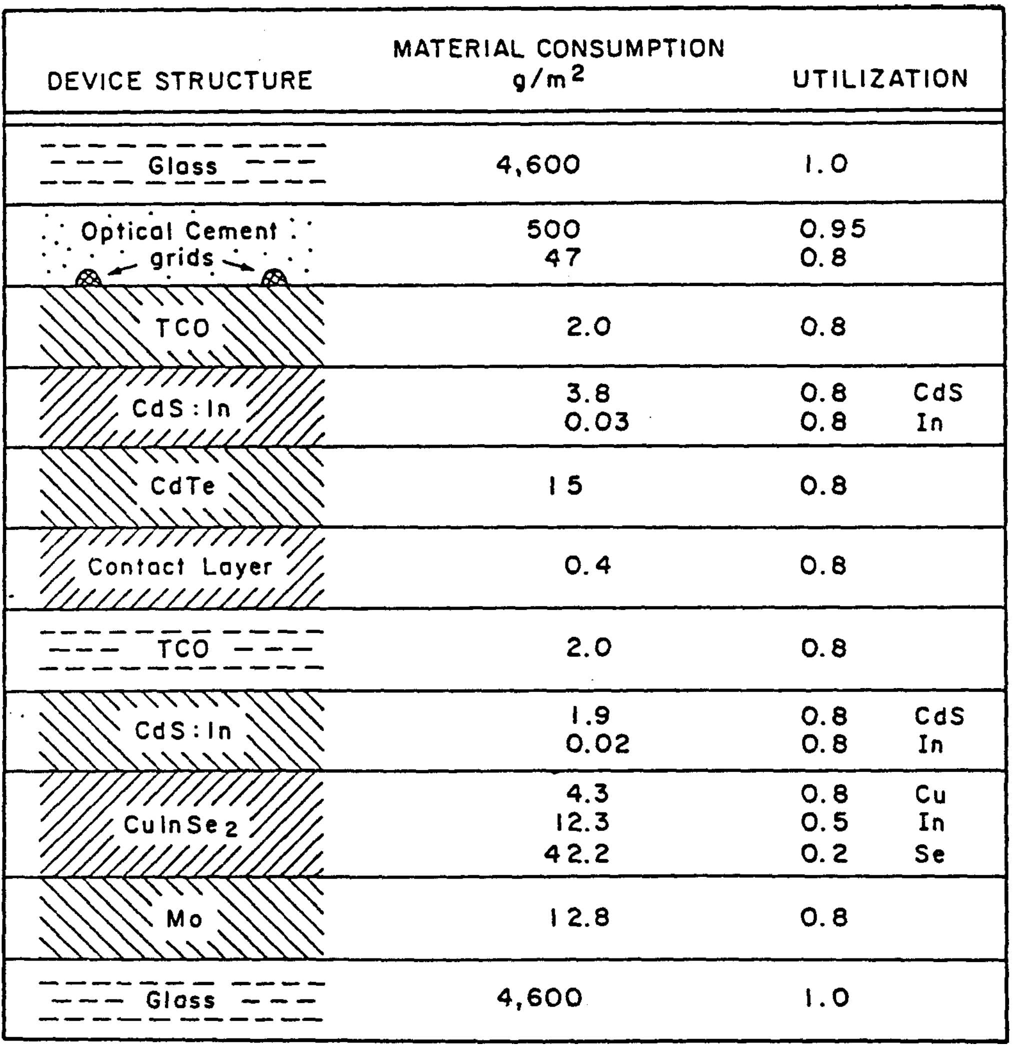

DEVICE STRUCTURE	MATERIAL CONSUMPTION g/m^2	UTILIZATION	
Glass	4,600	1.0	
Optical Cement	500	0.95	
grids	47	0.8	
TCO	2.0	0.8	
CdS : In	3.8	0.8	CdS
	0.03	0.8	In
CdTe	15	0.8	
Contact Layer	0.4	0.8	
TCO	2.0	0.8	
CdS : In	1.9	0.8	CdS
	0.02	0.8	In
$CuInSe_2$	4.3	0.8	Cu
	12.3	0.5	In
	42.2	0.2	Se
Mo	12.8	0.8	
Glass	4,600	1.0	

Figure 3.3c Material Consumption for Two Terminal Device

DEVICE STRUCTURE	TECHNIQUE	DETAILS
Glass	Purchased	Cleaned prior to use
Optical Cement grids	Mechanical Application Screen Printed	
TCO	Sputtered	
CdS : In	Vacuum Evaporation	1.0 $\mu m/min$ $T_s = 220°C$ $P < 10^{-4}$ Torr Post deposition Ht. treatment = 16-48 hr in air at 200°C
CdTe	Vacuum Evaporation	1.0 $\mu m/hr$ $T_s = 180°C$ $P < 10^{-4}$ Torr Post deposition Ht. treatment = 3 hr in air at 300°C
Contact Layer	Sputtered	$P < 10^{-6}$ torr
TCO	Sputtered	Heat Treatment of $CuInSe_2/CdS(In)$ Device : 200 °C 16-24 hr in air .
CdS : In	Vacuum Evaporation	1.0 $\mu m/min.$ $T_s = 220°C$ $P < 10^{-4}$ Torr
$CuInSe_2$	Vacuum Evaporation (Sputtering)	Two layer deposition : Excess of Se used $P < 10^{-4}$ Torr 1. $T_s = 350°C$ 10 Å/sec $t_1 = 1.7\ \mu m$ Cu rich $T_s = 450°C$ 14 Å/sec $t_2 = 1.3\ \mu m$ In rich
Mo	Sputtered	
Glass	Purchased	Cleaned prior to Mo deposition

Figure 3.3d Two Terminal Tandem Device - Processing Requirements

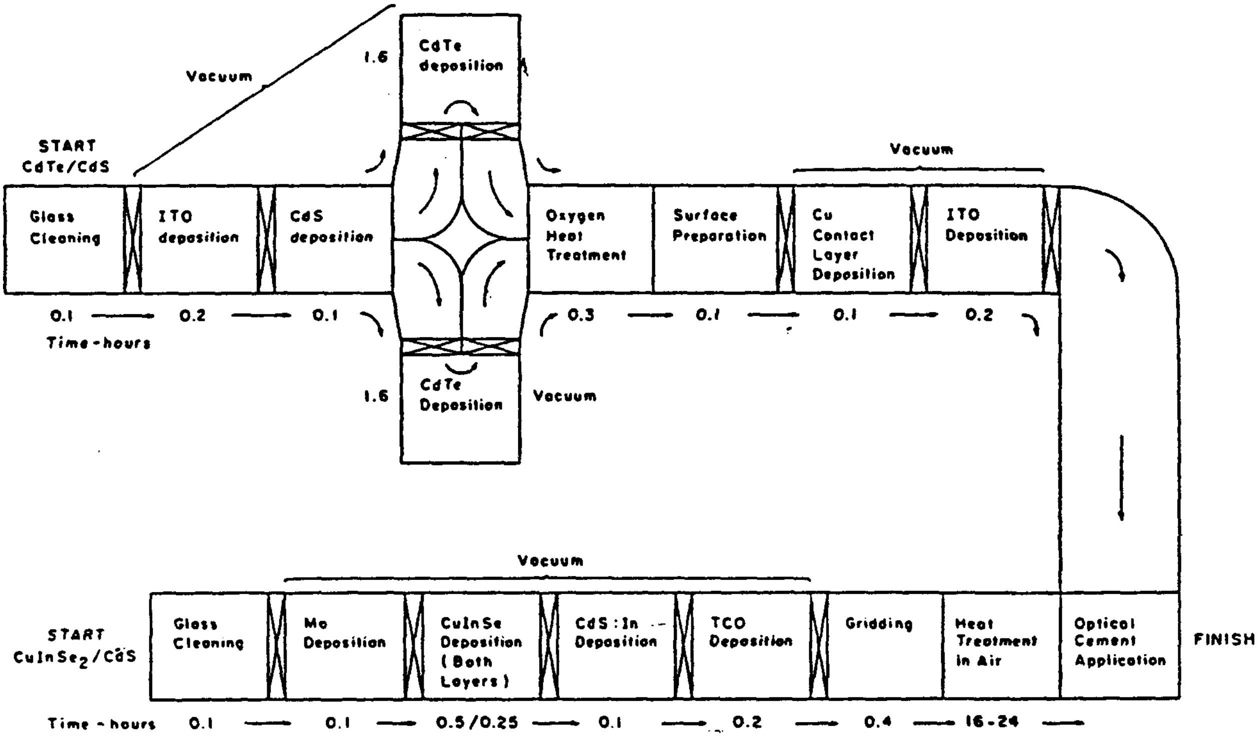

Figure 3.4a Process Flow Sheet for Four Terminal Device

	MATERIAL REQUIREMENTS		
DEVICE STRUCTURE	THICKNESS	COMPOSITION	PROPERTIES
Glass	1.6 mm	Soda Lime Glass	
Mo	1 μm		$< 0.1\ \Omega/\square$
$CuInSe_2$	3.0 μm	% Cu = 24 % In = 26 % Se = 50	
CdS : In	1.0 μm	In ≤ 1%	$\rho \sim 0.1 - 1\ \Omega$ - cm
TCO	200 nm	SnO ZnO	$15 - 20\ \Omega/\square$
grids Optical Cement	0.1 mm 95%T 0.25 mm	Nickel	99.999 % pure Optically matched to TCO
TCO	200 nm	ITO	$15 - 20\ \Omega/\square$
Contact Layer	1-5 nm	Copper	99.999 % pure
Cd Te	2 μm		
CdS	500 nm		
ITO	200 nm		$15 - 20\ \Omega/\square$
Glass	1.6 mm	Soda Lime Glass	

Figure 3.4b Four Terminal Tandem Device - Design Basis

DEVICE STRUCTURE	MATERIAL CONSUMPTION g/m^2	UTILIZATION	
Glass	4,600	1.0	
Mo	12.8	0.8	
$CuInSe_2$	4.3 12.3 42.2	0.8 0.5 0.2	Cu In Se
CdS : In	1.9 0.02	0.8 0.8	CdS In
TCO	2.0	0.8	
grids Optical Cement	47 500	0.8 0.95	
TCO	2.0	0.8	
Contact Layer	~ 0.4	0.8	
CdTe	15	0.8	
CdS	3.8	0.8	
ITO	2.0	0.8	
Glass	4,600	1.0	

Figure 3.4c Material Consumption for Four Terminal Device

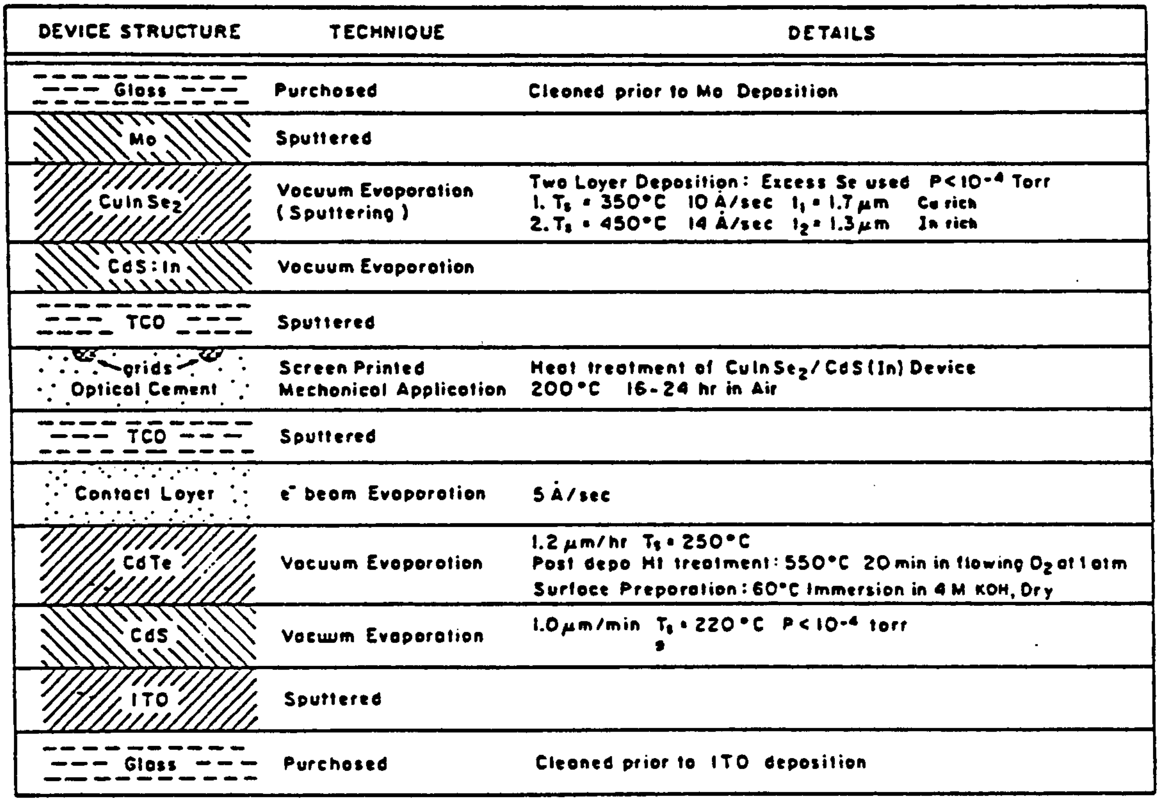

DEVICE STRUCTURE	TECHNIQUE	DETAILS
Glass	Purchased	Cleaned prior to Mo Deposition
Mo	Sputtered	
$CuInSe_2$	Vacuum Evaporation (Sputtering)	Two Layer Deposition: Excess Se used $P<10^{-4}$ Torr 1. T_s = 350°C 10 Å/sec t_1 = 1.7 µm Cu rich 2. T_s = 450°C 14 Å/sec t_2 = 1.3 µm In rich
CdS:In	Vacuum Evaporation	
TCO	Sputtered	
grids Optical Cement	Screen Printed Mechanical Application	Heat treatment of $CuInSe_2$/CdS(In) Device 200°C 16-24 hr in Air
TCO	Sputtered	
Contact Layer	e^- beam Evaporation	5 Å/sec
CdTe	Vacuum Evaporation	1.2 µm/hr T_s = 250°C Post depo Ht treatment: 550°C 20 min in flowing O_2 at 1 atm Surface Preparation: 60°C Immersion in 4 M KOH, Dry
CdS	Vacuum Evaporation	1.0 µm/min T_s = 220°C $P<10^{-4}$ torr
ITO	Sputtered	
Glass	Purchased	Cleaned prior to ITO deposition

Figure 3.4d Processing Requirements for Four Terminal Tandem Device

SECTION 4.0

Future Research

$CuInSe_2$ Cells

Future research and development is needed in order to achieve higher efficiencies and to determine the limits of performance for $CuInSe_2$ thin film solar cells. In order to systematically raise the efficiency of $CuInSe_2$ devices and to establish the limiting achievable efficiency, improved understanding at both the material and device level is required. At the basic materials level it has not been established with certainty how the carrier density is controlled in the $CuInSe_2$, nor is it known to what extent or by what mechanisms this is affected by the growth process and subsequent heat treatments. The morphology and surface roughness of the $CuInSe_2$ are also certain to affect cell performance. Fundamental studies of the influence of material preparation conditions on carrier concentration and morphology are needed.

Basic understanding of the material parameters and the junction mechanisms which control the open circuit voltage should lead to devices with increased open circuit voltage and efficiency. Optimized wide gap window layers such as (CdZn)S and ZnO can provide for increased blue response, and may enhance V_{oc}. Detailed analysis of fill factor losses, leading to optimum contacts are also needed.

Tandem Cell Based on $CuInSe_2$

Research should continue on monolithic two-terminal cascade cells since multi-junction cells have the potential of achieving the highest efficiencies. Research should be directed towards using existing technologies for a-Si and CdTe as the top cells in conjunction with the $CuInSe_2$/CdS bottom cells. Processing limits reflecting the most sensitive thin-film material used in the device should be established. Methods must be developed to electrically match the individual junctions at maximum power output and to minimize the spectral sensitivity of the two-terminal configuration.

Section 5.0

REFERENCES

1. IEC Final Report XL-2-02078-01 July, 1983.
2. R.A. Michelsen and W.S. Chen, Appl. Phys. Lett., 36(1980)371.
3. R.W. Birkmire, L.C. DiNetta, P.G. Lasswell, J.D. Meakin and J.E. Phillips, Solar Cells 16(1986)419.
4. R.J. Matson, K.A. Emery and R.E. Bird, Solar Cells 11 #2(1984)105.
5. J.E. Phillips, 14th IEEE Photovoltaics Specialists Conference,(1980)734.
6. E.H. Roderick, "Metal Semiconductor Contacts", Claredon Press Oxford(1978).
7. S.S. Hegedus, IEEE Transactions on Electron Devices ED-31 #5(1984)629.
8. A. Rothwarf, Solar Cells, 2(1980)115.
9. IEC Third Quarterly Report #XL-4-04025-1 February 1985.
10. IEC First Quarterly Report #XL-4-04025-1 August 1984.
11. IEC Semi-Annual Report XL-4-04025-1 November 1984.
12. IEC Annual Report XL-4-04025-1 July 1985.
13. IEC Fifth Quarterly Report XL-4-04025-1 August 1985.
14. IEC Final Report XL-4-03146-1 January 1986.
15. T.P.L. Li, Proceedings IEEE 33rd Electronic Components Conference, (1983)546.
16. B.M. Basol and E.S. Tseng, Appl. Phys. Lett. 48 #14(1986)946.
17. Y. Tyan and E. A. Perez-Aburne, Proceedings of the 16th IEEE Photovoltaic Specialists Conference (1982)781.
18. T.P. Thorpe, A.L. Fahrenbruch, and R.H. Bube, J. Appl. Phys. 60 #10(1986)3622.
19. D.J. Olego, J.P. Faurie, S.Siuananthan and P.M. Raccah, Appl. Phys. Lett. 47 #11(1985)1172.
20. H. Arwin and D. E. Aspnes, J. Vac. Sci. Technol, A2(3), 1984.
21. M.H. Patterson and R.H. Williams, J. Phys. D: Appl. Phys., 11, 1978.
22. J.G. Werthen, J.-P. Haring, and R.H. Bube, J. Appl. Phys., 54,(2), 1983.
23. W.J. Danaher, L.E. Lyons, and G.C. Morris, Appl. Surf. Sci., 22/23, 1985.
24. A. Ebina, K. Asano, Y. Suda, and T. Kakahaski, J. Vac. Sci Technol., 17(5),1980.
25. H. Matsumoto, A. Nakano, H. Uda, S. Ikegama and T. Miyuzawa, Jap. Jour. Appl. Phys. 21(1982)800.
26. G.A. Swartz, Semiconductors and Semimetals (J.I. Pankove, Editor)V210, Academic Press, Inc. (1984)40.
27. L.C. Isett, J. Appl. Phys. 56 #12(1984)3508.
28. J.G. Werthen, A.L. Fahrenbruch, and R.H. Bube, J. Appl. Phys. 54(1983)2750.

29. T.W.F. Russell, B.N. Baron and R.E. Rocheleau, Fundamentals and Applications of Solar Energy II, AIChE Symposium Series 77, (1981)70-77.
30. R.E. Rocheleau, Ph.D. Dissertation, U. of Delaware, 1981.
31. B.N. Baron, S.C. Jackson, R.E. Rocheleau, Final Report for SERI Subcontract #XL-4-03146-1 "Fundamental Engineering Analysis of CdTe/CdS Photovoltaic Processing."
32. S.C. Jackson, B.N. Baron, R.E. Rocheleau and T.W.F. Russell, "A Chemical Reaction Model for Physical Vapor Deposition of Compound Semiconductor Films." Submitted to AIChE Journal.
33. P.E. Russel, O. Jamjoum, R.K. Ahrenkiel, L.L. Kazmerski, R.A. Mickelsen and W.S. Chen, Appl. Phys. Lett. 40,995 (1982).

Appendix 1

A Chemical Reaction Model for Physical Vapor Deposition of Compound Semiconductor Films

A model for the physical vapor deposition of compound semiconductor films that describes film growth from component molecular beams is presented. Constitutive relationships are used in the model to account for incomplete adsorption from the incident molecular beams, emission of adsorbed components into vacuum, and surface reactions of the elemental species. The model predicts film composition and growth rate as a function of incident fluxes and substrate temperature. It is applicable for important binary and ternary alloy semiconductors including the II-VI and III-V compounds over the range of deposition conditions yielding both stoichiometric and two-phase films. In this paper the model equations and the behavior predicted by the model are described for a number of material systems including (CdHg)Te, (CdZn)S, and $CuInSe_2$.

S. C. Jackson, B. N. Baron,
R. E. Rocheleau and T. W. F. Russell
Institute of Energy Conversion
University of Delaware
Newark, DE 19716

Introduction

Thin-film compound semiconductors including the II-VI and III-V materials are used in photovoltaic cells (Russell et al., 1979), photonic devices (Mino et al., 1985), and thin-film transistors for large area display (Brody, 1984). This wide range of applications is the result of the high light absorption of such semiconductors and their ability to be controlled and adjusted for energy gap and refractive index using ternary alloys.

Physical vapor deposition (PVD) techniques including molecular beam epitaxy (MBE), vacuum evaporation, sputtering, electron beam evaporation, and hot wall evaporation are frequently used to deposit these compound semiconductors. A comprehensive review of physical vapor techniques can be found in Bunshah et al. (1982). Physical vapor deposition is best characterized by a comparison to chemical vapor deposition. While surface reactions can be very important for both deposition techniques, the manner in which film precursors are delivered to the substrate distinguishes these two techniques. In physical vapor deposition, the film precursors are generated and delivered to the film using a physical process. That is, the film precursors are generated from an independently controlled source separated from the substrate. The sources are typically an evaporation cell (a Knudsen cell or open boat). The film precursors are transported to the substrate by a molecular or atomic beam in high vacuum.

In chemical vapor deposition, however, gas phase reactions initiated by light, heat, or high-energy electrons (plasma) generate the film precursors typically in close proximity to the substrates. Gas phase and surface reactions may be closely coupled with the potential of significant heat and mass transport effects.

In this paper, a chemical reaction engineering model for the growth of binary and ternary compound semiconductor films from component molecular beams is described. This quantitative mathematical description provides a methodology for analyzing and understanding the laboratory-scale deposition process in order to guide materials research and the design of commercial production units.

Physical Situation

Physical vapor deposition techniques utilize molecular beams directed onto a temperature-controlled substrate upon which the species adsorb and react to deposit a film. In molecular beam epitaxy and vacuum evaporation the molecular beams are generated from individually heated compound or elemental sources. Figure 1 shows a representative thermal evaporation system with effusion-type sources. Evaporated materials flow from the source bottles, exit the collimating nozzles into vacuum, and

---

Correspondence concerning this paper should be addressed to R. E. Rocheleau.

S. C. Jackson is with the Engineering Department, E. I. duPont deNemours & Co., Wilmington, DE 19898.

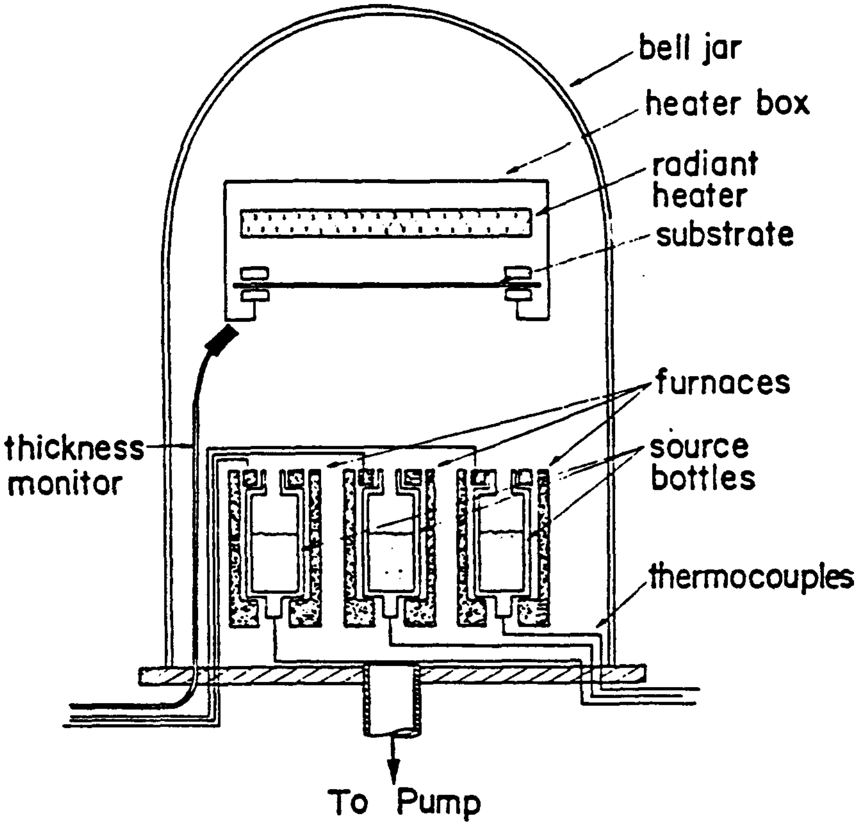

Figure 1. Typical vacuum system components for a three-source system.

form beams of evaporant atoms or molecules. At the pressures used in physical vapor deposition (less than 10^{-6} Pa) the evaporant material experiences few intermolecular collisions. The molecular flux or beam intensity at any surface within the system depends on the spatial distribution of the beam, the orientation of the surface toward the source, the source-to-surface distance, and the total mass flow from the source (Dayton, 1961; Stickney et al., 1968; Giordmaine and Wang, 1960; Jackson et al., 1985).

The growth of compound thin films from component molecular beams has been described by many investigators (Gunther, 1968; Smith and Pickhardt, 1975; Faurie et al., 1983, 1985; Chow and Johnson, 1985; Jansen and Melnyk, 1984; Foxon, 1983; Kawabe and Matsiura, 1984; Myers et al., 1982; Summers et al., 1984) with general agreement that the conversion or utilization of one species and the film composition vary with the substrate temperature and flux of the other components. A simplified description of the generally accepted mechanisms that explain this behavior follows.

The substrate suspended over the sources intercepts material from the component beams. The incident molecules will either be reflected or be adsorbed. The fraction reflected depends on the energy of the incident species and the thermal accommodation characteristics of the substrate. The adsorbed species, generally considered to be adatoms, can diffuse to favorable low-energy sites and react, or can be emitted into vacuum. If the substrate temperature is low enough, adatoms may have insufficient energy to diffuse and react or be emitted into vacuum. These adatoms will be codeposited with the compound film as crystal defects or as a second phase. As a result of these competing processes, the growth rate and composition of the deposited film vary depending on the incident flux from each source, the energy of the incident species, and the substrate temperature.

Model Equations

In this section, model equations are developed using steady state component and overall mass balances that account for all incident, adsorbed, emitted, and reflected species. Constitutive equations providing a quantitative description of the rate processes are presented. The material- and process-specific model parameters that must be obtained from the literature or through experiment are described. No equipment-specific fitting parameters are needed.

Mass balances

The steady state component balances for the control volume at the surface of the growing film as shown in Figure 2 are:

$$\frac{1}{\phi Mw(j)}\frac{dMj}{dt} = r(i,j) - r(r,j) - r(e,j) - r(rxt,j) \quad (1)$$

where j represents each of the components in the reacting system. For example, in the (CdZn)S material system, six components are considered: Cd, Zn, S, CdS, ZnS, and (CdZn)S. If compound sources are used, then the molecular beams will consist of monatomic cadmium and zinc and diatomic sulfur (Jackson, 1984). Elemental sources, however, form beams of monatomic cadmium and zinc and polyatomic sulfur, S_n, where the number of sulfur atoms, n, depends on the operating temperature and pressure of the source (Mills, 1974). For typical conditions reported in this work S_6, S_7, and S_8 are the predominate

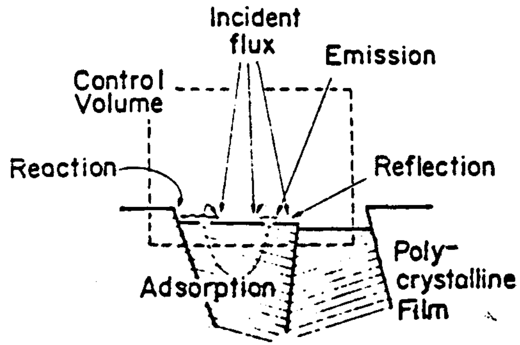

MASS BALANCES:

Accumulation of component j, kg moles/m^2/sec

$r(d,j) =$

$+r(i,j)$ ~ Incident rate of j, kg moles/m^2/sec

$-r(r,j)$ ~ Reflection rate of j, kg moles/m^2/sec

$-r(e,j)$ ~ Emission rate of j, kg moles/m^2/sec

$-r(rxt,j)$ ~ Reaction rate of j, kg moles/m^2/sec

Figure 2. Control volume at surface of a growing film and basic mass balance showing accumulation terms.

species. For compound films [CdS, ZnS, (CdZn)S in the solid phase], the component balances are used to account for the stoichiometry of the film. They do not represent the structure of the film nor do they imply the existence of single molecules of CdS or ZnS in the solid or adsorbed phase.

The lefthand side of Eq. 1 represents the molar rate of accumulation or deposition of adsorbed component j per unit area (ϕ):

$$r(d,j) = \frac{1}{\phi Mw(j)} \frac{dMj}{dt} \qquad (2)$$

Equation 1 is based on a control volume small enough that the incident flux from each source is uniform within it. The net rate of surface diffusion into the control volume is assumed to be negligible compared to this incident flux. The incident component $r(i,j)$ is either adsorbed or reflected from the surface where the rate of reflection is $r(r,j)$. The adsorbed component may react at a rate $r(rxt,j)$ to form a compound, be emitted from the surface into vacuum at a rate $r(e,j)$, or be codeposited with the compound in an elemental form at a rate $r(d,j)$. Solutions of Eq. 1 with appropriate constitutive rate expressions for $r(i,j)$, $r(r,j)$, $r(e,j)$, and $r(rxt,j)$ for all components within the control volume yield the deposition rate and composition of the film as a function of the component incident rates or fluxes, the temperature of the incident species, and the substrate temperature.

Constitutive relationships

Incident Flux. The incident flux rate of each component can be measured independently or be calculated using previously verified models (Jackson et al., 1985; Rocheleau et al., 1982). The rate at which the material leaves the control volume is controlled by two mechanisms, reflection $r(r,j)$, and emission of the adsorbed species into vacuum $r(e,j)$, as indicated in Figure 2.

Adsorption-Reflection. The incomplete adsorption of an incident component is characterized by the reflection factor δ (Hirth and Pound, 1960; Eyring et al., 1964; Hirth, 1966). The reflection rate can be assumed to be proportional to the incident rate:

$$r(r,j) = [1 - \delta(j)]r(i,j) \qquad (3)$$

where $\delta(j)$ is the reflection factor of incident component j.

The reflection factor is weakly dependent on the temperatures of the substrate and the incident molecule. It also depends on the composition of the deposited film (Eyring t al., 1964). By definition $\delta(j)$ must be between zero and one. In practice, the reflection factor of one component of a compound film can be determined experimentally by using an excess flux of the second component from an elemental source (Smith and Pickhardt, 1975).

Emission. The rate at which the adsorbed components are emitted from the substrate back into vacuum, $r(e,j)$, depends on the composition of the surface, expressed as the adatom concentration $[j^*]$, the binding energy of the adatom to the substrate and the thermal energy of the adatom:

$$r(e,j) = Ev(j)[j^*] \qquad (4)$$

The emission factor, $Ev(j)$, characterizes the binding energy to the substrate and the thermal energy of the adatom. The emission factors are component-specific and may depend on the species present as an adatom, e.g., S_2 vs. S_8. As will be shown below, it is not necessary to evaluate the value of the emission factor since it is lumped together with the forward reaction rate constant.

Reaction. An adsorbed species may react to form the binary or ternary alloy semiconductor, may be emitted into vacuum, or may be codeposited as a second phase. In order to simplify the equations that follow, a one-to-one stoichiometry for the reaction step is assumed. This assumption is applicable to the II-VI and III-V classes of compounds. However, by assuming other stoichiometries the model can be applied to any class of compounds. Equation 5 shows the net reaction for the formation of a solid phase ternary alloy film of $(A_1 - xB_x)Y$ allowng for the codeposition of the element Y:

$$(1 - x)A^* + xB^* + (1 + \lambda)Y^* \rightarrow (A_{1-x}B_x)Y + \lambda Y \qquad (5)$$

The coefficient x in Eq. 5 is zero for deposition of a binary semiconductor AY. If codeposition of a second elemental phase does not occur, then λ is also zero. The ability to predict codeposition of an element is particularly important for low vapor pressure materials like tellurium during the formation of HgTe or when there is a large incident flux rate of one element.

The ternary alloy $A_{1-x}B_xY$ shown in Eq. 5 is modeled as a random mixture of $(1 - x)AY$ plus xBY. Constitutive equations for the formation of AY and BY, described by Eq. 5, are derived by assuming that the kinetic expressions are governed by two competing, parallel surface reactions:

$$(1 - x)A^* + (1 - x)Y^* \underset{k_r(AY)}{\overset{k_f(AY)}{\rightleftharpoons}} (1 - x)AY \qquad (6)$$

$$xB^* + xY^* \underset{k_r(BY)}{\overset{k_f(BY)}{\rightleftharpoons}} xBY \qquad (7)$$

The net reaction rates for species A, B, Y, AY, and BY are then represented by:

$$r(rxt, A) = k_f(AY)[A^*]^n[Y^*]^m - (1 - x)k_r(AY) \quad (8)$$

$$r(rxt, B) = k_f(BY)[B^*]^n[Y^*]^m - xk_r(BY) \quad (9)$$

$$r(rxt, Y) = r(rxt, A) + r(rxt, B) \quad (10)$$

$$r(rxt, AY) = -r(rxt, A) \quad (11)$$

$$r(rxt, BY) = -r(rxt, B) \quad (12)$$

where:

$k_f(AY)$, $k_f(BY)$ = The forward reaction rate constants for the formation of the AY and BY compounds, respectively.
$k_r(AY)$, $k_r(BY)$ = The reverse reaction rate constants for the formation of the AY and BY compounds, respectively, $kmol/m^2 \cdot s$ or $(no./cm^2/s)$.
n, m = Order of the reaction with respect to each component. Value is on the order of 1.0.

The factors $(1 - x)$ and x in Eqs. 8 and 9 account for the decrease of the net reverse reaction rate with the composition of the film relative to the pure compounds due to the effective surface coverage with AY or BY, respectively. Large changes in the energetics in the process would be seen by changes in k_f with surface composition. Equations 8 and 9 are similar to the surface reaction step proposed by Somarjai and Jepsen (1964) for the evaporation of CdS, and are similar to the interaction probability theory for the deposition of compound semiconductors proposed by Freller and Gunther (1982).

As shown in Eqs. 6–9, the reaction rate is described by two kinetic constants, the forward rate constant k_f, and the reverse rate constant k_r. In this model the forward and reverse rate constants are assumed to have the usual Arrhenius form:

$$k_r \quad \text{or} \quad k_f = k' \exp[-E/(R_o T_s)] \quad (13)$$

For most compounds of interest, including many II-VI and III-V semiconductors (Somerjai and Jepsen, 1964) the dissociation of the compound to form the adsorbed elemental species is the rate-controlled step during evaporation. The reverse reaction only becomes important at high substrate temperatures where dissociative evaporation of the compound is significant.

Codeposition of Second Phase. A second elemental phase is formed if the adsorption rate of the incident flux, $\delta(j)r(i, j)$, is greater than the sum of the reaction rate $r(rxt, j)$, Eqs. 8–12, and the emission rate $r(e, j)$. The emission rate of the element is then assigned a maximum value given by the Hertz-Knudsen equation:

$$r(e_{max,j}) = P(T_a, j)\alpha_v(j)[2\pi R_o T_a Mw(j)]^{-1/2} \quad (14)$$

where:

$P(T_{a,j})$ = Vapor pressure of element j at the adatom temperature, Pa $(dynes/cm^2)$
$\alpha_v(j)$ = Evaporation coefficient for the element j
T_a = Adatom temperature, K
R_o = Gas law constant
$Mw(j)$ = Molecular weight of species, j

This expression, Eq. 14, was successfully used with the other model equations to accurately predict deposition conditions where codeposition of Te occurs for the (CdHg)Te material system.

Application of the Model

In this section the model equations are solved for three material systems, (CdZn)S, (CdHg)Te, and $CuInSe_2$. Specific assumptions, the model equations, and values of the model parameters are listed for each system. The model predictions are shown to agree closely with experimental behavior.

(CdZn)S

The key assumptions used to simplify the model, Eqs. 1–15, for the (CdZn)S material system are the following.

1. The incident and reflected flux of the compound components are zero:

$$r(i, \mathrm{CdS}) = r(i, \mathrm{ZnS}) = 0 \quad (15)$$

$$r(r, \mathrm{CdS}) = r(r, \mathrm{ZnS}) = 0 \quad (16)$$

Compound and elemental sources have been used for (CdZn)S depositions. In either case, only elemental species exist in the incident flux since the compounds dissociatively evaporate and the rate of forming the compound species in the space between the source and substrate is negligible at the vacuums used.

2. CdS and ZnS are known to evaporate dissociatively; therefore, their rate of emission into vacuum is zero:

$$r(e, \mathrm{CdS}) = r(e, \mathrm{ZnS}) = 0 \quad (17)$$

3. The three elements, Cd, Zn, and S, are reasonably volatile at the substrate temperatures (200–260°C) and incident fluxes of interest. Consequently, it is assumed that they are not deposited as an elemental phase with the compound film:

$$r(d, \mathrm{Cd}) = r(d, \mathrm{Zn}) = r(d, \mathrm{S}) = 0 \quad (18)$$

At substrate temperatures below ~180°C or an excess incident flux of $>50 \times 10^{-8}\ kmol/m^2 \cdot s$ of the least volatile component, zinc, elemental deposition is likely. Equations dealing with codeposition have been applied to (CdHg)Te system and are discussed below.

4. At the substrate temperature of interest, the reverse reaction rate is negligible:

$$k_r(\mathrm{CdS}) = k_r(\mathrm{ZnS}) = 0 \quad (19)$$

At substrate temperatures >300°C, dissociation of the compound—i.e., the reverse reaction rate—becomes important, as evidenced by the rate of dissociative evaporation.

Substituting these assumptions, Eqs. 15–19, into the model, Eqs. 1–14, and simplifying gives a system of four simultaneous equations; these, Eqs. 20–23, are shown at the top of Table 1 along with condition Eqs. 24 and 25.

Three sets of experiments were done to verify the model equations and determine values of the model parameters: cadmium sulfide depositions, zinc sulfide depositions, and depositions of the ternary alloy, cadmium-zinc sulfide. In each experiment the

Table 1. (CdZn)S Deposition Model Equations and Parameters

Equations

$$r(d, \mathrm{CdS}) = K(\mathrm{CdS})\,[\delta(\mathrm{Cd})\, r(i, \mathrm{Cd}) - r(d, \mathrm{CdS})]^{n} \times \{\delta(s)\, r(i, s) - r[d, (\mathrm{CdZn})\mathrm{S}]\}^{m} \quad (20)$$

$$r(d, \mathrm{ZnS}) = K(\mathrm{ZnS})\,[\delta(\mathrm{Zn})\, r(i, \mathrm{Zn}) - r(d, \mathrm{ZnS})]^{n} \times \{\delta(s)\, r(i, s) - r(d, (\mathrm{CdZn})\mathrm{S}]\}^{m} \quad (21)$$

$$r[d, (\mathrm{CdZn})\mathrm{S}] = r(d, \mathrm{CdS}) + r(d, \mathrm{ZnS}) \quad (22)$$

$$x = r(d, \mathrm{ZnS})/r[d, (\mathrm{CdZn})\mathrm{S}] \quad (23)$$

where

$$K(\mathrm{CdS}) = k_f(\mathrm{CdS})/Ev(\mathrm{Cd})^{n}/Ev(\mathrm{S})^{m} \quad (24)$$

$$K(\mathrm{ZnS}) = k_f(\mathrm{ZnS})/Ev(\mathrm{Zn})^{n}/Ev(\mathrm{S})^{m} \quad (25)$$

Parameter	Value	Deposition Conditions
$\delta(\mathrm{Cd})$	0.8–0.9	$T_s = 200$–260°C $T_i = 430$–460°C
$\delta(\mathrm{Zn})$	0.6–0.7	$T_s = 200$–260°C $T_i = 534$–577°C
$\delta(\mathrm{S})$	0.5–0.7	$T_s = 200$–260°C $T_i = 167$–172°C
n, m	½ or 1	$T_s = 200$–260°C $x = 0.0$–1.0
$K(\mathrm{ZnS}), K(\mathrm{CdS})$		
for $n = m = 1$	$>10^{8}$ m^3 · s/kmol	$T_s = 200$–260°C
for $n = m = ½$	>10 (dimensionless)	$x = 0.0$–1.0
$K(\mathrm{Zns})/K(\mathrm{CdS})$		
for $n = m = 1$	~16	$T_s = 200$–220°C
for $n = m = ½$	~4	$x = 0.1$–0.9

deposition rate $r[d, (\mathrm{CdZn})\mathrm{S}]$ and zinc fraction x were measured as a function of the incident flux composition and substrate temperature. A nonlinear least-squares procedure was used to fit the model predictions to the experimental data. The model was considered accurate if the calculated goodness of fit-of the model from the nonlinear least-squares program was equal to the estimated experimental error for both the film composition, x, and the deposition rate, $r(d, \mathrm{CdS})$, $r(d, \mathrm{ZnS})$, or $r(d, \mathrm{CdZnS})$. These criteria were met. The resulting estimated values of the model parameters are shown in Table 1. The solution of the model equations is discussed more fully elsewhere (Jackson, 1984).

A convenient way to present the results for CdS and ZnS depositions is to plot the deposition rates, $r(d, \mathrm{CdS})$ or $r(d, \mathrm{ZnS})$, as a function of the incident flux rate of one element while fixing the incident flux rate of the second elemental component. This type of plot is shown in Figure 3 for the deposition of ZnS as a function of the sulfur incident flux rate for a substrate temperature of 200°C. Experimental data points and curves representing the best-fit model predictions are shown for each of four different zinc incident flux rates. Near the origin of the graph, the film growth rate is proportional to the sulfur incident rate, $r(i, \mathrm{S})$. The slope in this region is approximately equal to the value of the sulfur reflection factor obtained from the least-squares analysis. Thus, in the sulfur-limited regime, the growth rate is described by

$$r(d, \mathrm{ZnS}) \sim \delta(\mathrm{S})r(i, \mathrm{S}) \quad (26)$$

where

$$\delta(\mathrm{S}) \sim 0.5 \quad (27)$$

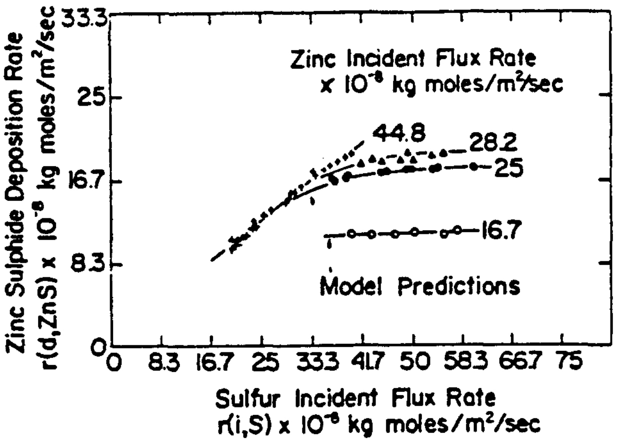

Figure 3. Dependence of ZnS deposition rate on sulfur incident flux rate.
Substrate temp., 200°C; no incident Cd

Similarly, at a high sulfur incident flux rate the deposition rate becomes independent of the sulfur flux rate. Where the curves are horizontal in Figure 3, the deposition rate is ~70% of the zinc incident rate, a fraction that is very close to the Zn reflection factor. An expression analogous to Eq. 26 is then applicable in this regime:

$$r(d, \mathrm{ZnS}) \sim \delta(\mathrm{Zn})r(i, \mathrm{Zn}) \quad (28)$$

where

$$\delta(\mathrm{Zn}) \sim 0.7 \quad (29)$$

The close agreement between the limiting slopes determined graphically from the sulfur- and zinc-rich regimes and the numerically determined reflection factors indicates that the deposition rate in these regimes is limited by the rate at which the low incident flux component is adsorbed onto the substrate.

Not only does the model accurately predict the sulfur- and zinc-limited regimes, it also accurately predicts the transition or knee in the curves shown in Figure 3. At the knee in the curves, the rate of deposition is controlled by the rates at which the adsorbed zinc and sulfur react. The curvature of the bend depends on the speed of the reaction relative to the emittance rate of the elemental components. For a very fast reaction, the curvature is very sharp, as is the case in Figure 3, indicating that the deposition is limited by the adsorption rate of one of the components. From the CdS and ZnS depositions, only an approximate or minimum value for the apparent reaction rate constants $K(\mathrm{CdS})$ and $K(\mathrm{ZnS})$, can be estimated. Further, since it is a very fast reaction, the orders of the reaction, n and m, cannot be accurately estimated from this data. Minimum values of $K(\mathrm{CdS})$ and $K(\mathrm{ZnS})$ are shown in Table 1 for two values of n and m.

For the alloy depositions, the goodness of fit was again equal to the estimated experimental error for both the film composition x, and deposition rate $r[d, (\mathrm{CdZn})\mathrm{S}]$. Excellent agreement between the predicted film composition and measured film composition for the alloy film is shown in Figure 4. The predicted composition is within 3 atomic percent of the measured composition across the range of composition from 10 to 90 atomic percent. The values of the model parameters used for these pre-

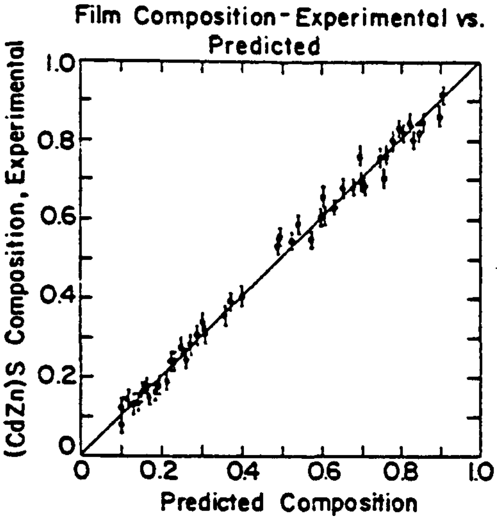

Figure 4. Comparison of measured and predicted Zn fraction x in $(Cd_{1-x}Zn_x)S$ alloy films.

dictions agreed with those obtained for the CdS and ZnS depositions. In addition, the data from the alloy depositions show that the zinc reacts faster than the cadmium so that the ratio of the apparent rate constants for ZnS to CdS is greater than one. The ratio resulting from the numerical fit is shown in Table 1.

During development of the model, several alternate rate expressions were tried for the rate of reaction step, Eqs. 8–12. These included a Langmuir-Hinshelwood-Hougen-Watson expression (Carberry, 1976) as well as an interaction probability relationship first proposed by Gunther (1968). However, none of these was able to model the strong asymptotic behavior of the data. The strong asymptotic behavior shown in Figure 3 has been reported by others, including Smith and Pickhardt (1975), and Foxon (1983) for other II-VI and III-V compounds. This suggests that the model may be applicable to wide classes of compounds formed by physical vapor deposition techniques.

(HgCd)Te

Several assumptions, similar to those used for the (CdZn)S material system, are used to simplify the model for the (HgCd)Te material system. These include the following.

1. The incident and reflected flux of the compound components are zero:

$$r(i, \mathrm{HgTe}) = r(i, \mathrm{CdTe}) = 0 \qquad (30)$$

$$r(r, \mathrm{HgTe}) = r(r, \mathrm{CdTe}) = 0 \qquad (31)$$

As in the (CdZn)S system both compound and elemental sources have been used for (CdZn)S depositions. In either case, only elemental species exist in the incident flux since the compounds dissociatively evaporate and the rate of forming the compound species in the space between the source and substrate is negligible.

2. HgTe and CdTe are known to evaporate dissociatively; therefore, the rate of emission into vacuum is zero:

$$r(e, \mathrm{HgTe}) = r(e, \mathrm{CdTe}) = 0 \qquad (32)$$

3. The metal components, Cd and Hg, are much more volatile than tellurium. Consequently, it is assumed that they are not deposited as an elemental phase with the compound film:

$$r(d, \mathrm{Hg}) = r(d, \mathrm{Cd}) = 0 \qquad (33)$$

Tellurium, however, has such a low volatility that it can form a second elemental phase in the compound film. Consequently, Eq. 14 must be used to estimate the emission rate if an elemental phase forms.

Substituting these assumptions, Eqs. 30–33, into the model and simplifying gives a system of simultaneous equations, Eqs. 34–43, shown in Table 2. Equations 34–40 are nearly identical to those used for the (CdZn)S system, Table 1, except that the reverse reaction rates, $k_r(\mathrm{HgTe})$ and $k_r(\mathrm{CdTe})$, have been included. Equations 41–43 are used to account for codeposition of elemental tellurium. One important feature of Eqs. 41–43 is that the maximum emission rate of tellurium, $r(e_{max}, \mathrm{Te})$ must be evaluated at the adatom temperature, T_a. The adatom temperature depends on the energy or temperature of the incident tellurium, T_i, the substrate temperature, T_s, and the ability of the substrate to accommodate the energy of the incident species. The thermal characteristics of the substrate were modeled using a thermal accommodation coefficient, ϵ, shown in Eq. 42.

The values of the model parameters shown in Table 2 were estimated using physical property data from Mills (1974) and experimental data as discussed elsewhere (Baron and Jackson 1986).

The conversion of CdTe predicted by the model and measured experimentally is shown as a function of substrate temperature and incident flux rate from a compound CdTe source in Figure

Table 2. (HgCd)Te Deposition Model Equations and Parameters

Equations

$$r(d, \mathrm{CdTe}) = K(\mathrm{CdTe})\, r(e, \mathrm{Cd})^n\, r(e, \mathrm{Te})^m\, (1 - x)\, k_r(\mathrm{CdTe}) \qquad (34)$$

$$r(d, \mathrm{HgTe}) = K(\mathrm{HgTe})\, r(e, \mathrm{Hg})^n\, r(e, \mathrm{Te})^m - x\, k_r(\mathrm{HgTe}) \qquad (35)$$

$$r(e, \mathrm{Cd}) = \delta(\mathrm{Cd})\, r(i, \mathrm{Cd}) - r(d, \mathrm{CdTe}) \qquad (36)$$

$$r(e, \mathrm{Hg}) = \delta(\mathrm{Hg})\, r(i, \mathrm{Hg}) - r(d, \mathrm{HgTe}) \qquad (37)$$

$$r(d, (\mathrm{HgCd})\mathrm{Te}) = r(d, \mathrm{CdTe}) + r(d, \mathrm{HgTe}) \qquad (38)$$

$$x = r(d, \mathrm{HgTe})/r[d, (\mathrm{HgCd})\mathrm{Te}] \qquad (39)$$

For no tellurium codeposition

$$r(e, \mathrm{Te}) = \delta(\mathrm{Te})\, r(i, \mathrm{Te}) - r[d, (\mathrm{HgCd})\mathrm{Te}] \qquad (40)$$

For tellurium deposition

$$r(e, \mathrm{Te}) = r(e_{max}, \mathrm{Te}) = P_o(T_a, \mathrm{Te})\, \alpha v(\mathrm{Te})\, [2\pi R_g T_a Mw(\mathrm{Te})]^{-1/2} \qquad (41)$$

$$T_a = (1 - \epsilon)\, T_s + \epsilon T_i \qquad (42)$$

$$r(d, \mathrm{Te}) = \delta(\mathrm{Te})\, r(i, \mathrm{Te}) - r[d, (\mathrm{HgCd})\mathrm{Te}] - r(e_{max}, \mathrm{Te}) \qquad (43)$$

Parameter	Value or Expression	Units
$\delta(\mathrm{Cd}), \delta(\mathrm{Hg}), \delta(\mathrm{Te})$	0.9	—
$r(e_{max}, \mathrm{Te})$	$\dfrac{3.0 \times 10^7}{\sqrt{T_a}} \exp(-17{,}715/T_a)$	kmol/m² · s
$K(\mathrm{CdTe})$	$5.7 \times 10^{-3} \exp(3{,}390/T_s)$	—
$K(\mathrm{HgTe})$	$2.7 \times 10^{-4} \exp(5{,}100/T_s)$	—
$k_r(\mathrm{CdTe})$	$\dfrac{2.8 \times 10^7}{\sqrt{T_s}} \exp(-23{,}030/T_s)$	kmol/m² · s
$k_r(\mathrm{HgTe})$	$\dfrac{1.2 \times 10^7}{\sqrt{T_s}} \exp(-13{,}980/T_s)$	kmol/m² · s
n, m	½	—
ϵ	0.88	—

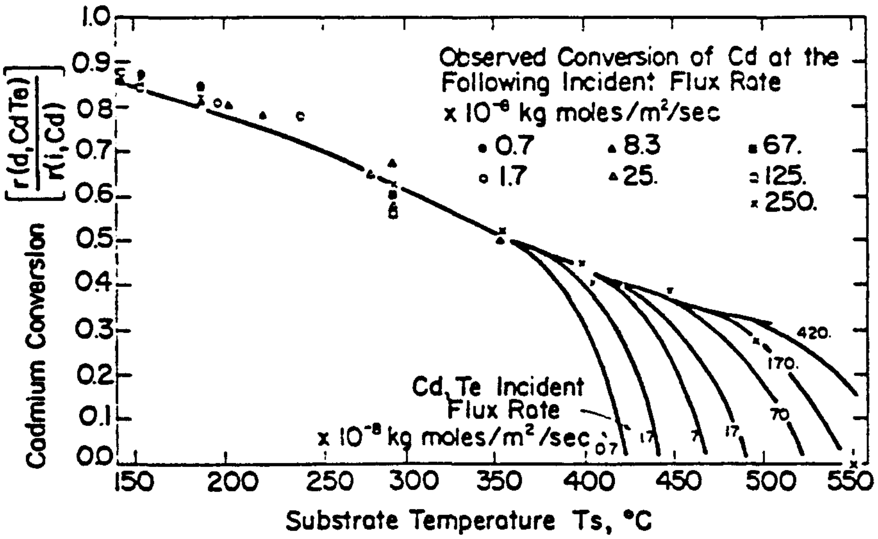

Figure 5. Measured and predicted (solid curves) conversion of Cd as a function of substrate temperature and incident flux rate from a compound CdTe source.

5. The conversion of CdTe is defined as:

$$\eta(\mathrm{CdTe}) = \frac{r(d,\,\mathrm{CdTe})}{r(i)} \qquad (44)$$

The incident flux rates of Cd or Te, $r(i)$, are equal for a compound source as considered in this example. For substrate temperatures from 100 to 350°C, the CdTe conversino changes from 0.9 to 0.5 and is independent of the incident flux. This decrease in the CdTe conversion with the substrate temperature is a result of the greater emission of the adsorbed elemental components at higher substrate temperatures. The insensitivity of the conversion with the incident flux below 350°C is accurately predicted as long as the orders of the reaction with respect to Cd and Te, n and m, are equal to ½. Above 350°C the reverse reaction rate, k_r(CdTe), becomes significant and the CdTe conversion drops rapidly with increasing substrate temperature and becomes dependent on the incident flux. This predicted trend is in part verified by the data.

The effect of varying deposition conditions including the substrate temperature, incident flux rate from a compound CdTe source, and the incident flux temperature on the codeposition of elemental tellurium is shown in Figure 6. The solid lines represent the predicted atomic fraction of tellurium deposited as a second phase in the CdTe film. The source temperature or incident flux temperature, T_i, needed to generate the flux rate indicated is shown at the top of the graph. The open circles represent films deposited at the conditions shown for which no tellurium was observed by X-ray diffraction. The crosses represent conditions for which elemental tellurium, >0.02 atomic fraction, was detected.

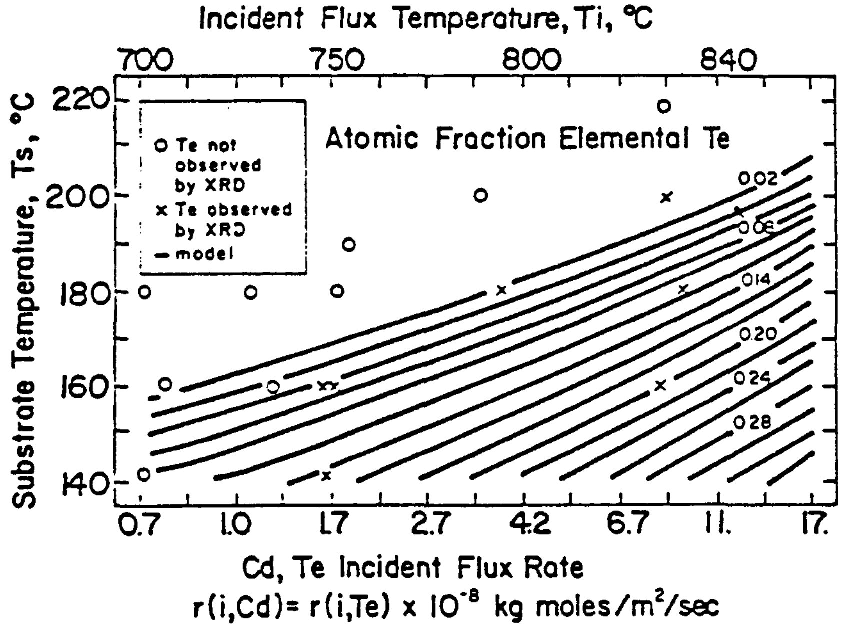

Figure 6. Evaporation conditions yielding codeposited elemental Te using a compound CdTe source.

The experimental data points indicate that elemental deposits of tellurium are formed preferentially at lower substrate temperatures and/or higher incident fluxes. For example, at a substrate temperature of 180°C, elemental deposits were not detected below an incident flux of 1.7×10^{-8} kmol/m^2 · s but were formed above a flux of 4×10^{-8} kmol/m^2 · s. This is in good agreement with the model predictions. The model predicts that at low substrate temperatures CdTe can be deposited without codepositing tellurium, provided that the incident flux and therefore the surface concentration of the adsorbed tellurium is low enough. At high substrate temperatures, adsorbed tellurium is emitted into vacuum more readily from the surface, and consequently a much higher incident flux is required for elemental codeposition.

The model equations were extended to the deposition of (HgCd)Te with the results shown in Figures 7 and 8. The solid lines represent the model behavior using the parameters shown in Table 2. The points are data reported by Faurie et al. (1983). The data were obtained at a constant cadmium and tellurium flux of 1.7×10^{-8} kmol/m^2 · s.

Figure 7 shows the Hg conversion as a function of substrate temperature and mercury flux. The Hg conversion is defined as:

$$n(\mathrm{Hg}) = \frac{r(d, \mathrm{HgTe})}{r(i, \mathrm{Hg})} \tag{45}$$

where $r(d, \mathrm{HgTe})$ is the rate at which HgTe is deposited in the HgCd)Te alloy film. The numbers next to the points indicate the experimental incident fluxes estimated by Faurie (1985).

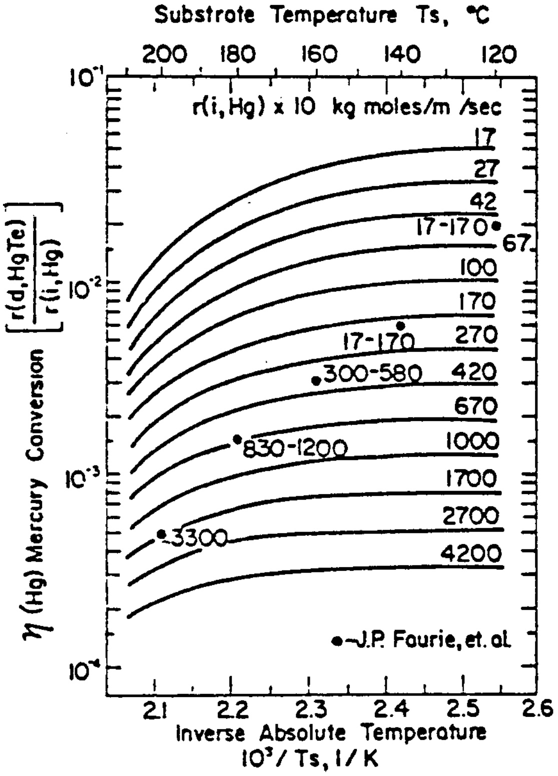

Figure 7. Hg conversion as a function of Hg incident flux rate *r(I*, Hg), and substrate temperature T_s for HgTe deposited in (HgCd)Te alloy.
Data of Faurie et al. (1985)

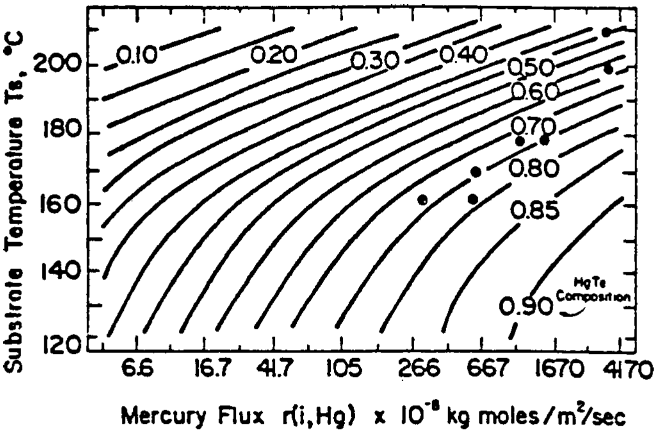

Figure 8. Mole fraction of HgTe deposited in (HgCd)Te alloy as a function of Hg incident flux rate and substrate temperature.
Data of Faurie et al. (1983)

The model predictions are shown as lines of constant mercury flux. As expected, the model predicts a drop in the Hg conversion with an increase in substrate temperature and an increase in the Hg flux. Although the experimental data are not at a constant Hg flux, the data do show a decrease in the Hg conversion with an increased flux and substrate temperature that is consistent with the model predictions.

Figure 8 shows the influence of substrate temperature and mercury flux on the HgTe content of the (HgCd)Te film. The points represent conditions reported by Faurie et al. (1985) that formed (HgCd)Te films with 80% HgTe. The curves, representing the model predictions, show a decrease in the HgTe composition as the substrate temperature increases or the mercury flux decreases. This predicted trend agrees closely with the experimental points. The quantitative agreement is very good except at the highest Hg flux.

CuInSe$_2$

The CuInSe$_2$ material, unlike (CdHg)Te or (CdZn)S, is not an alloy, as shown by its equilibrium phase diagram (Palatnik and Rugacheva, 1967). Several investigators (Don et al., 1985; Stolt et al., 1985) have noticed that the film compositions grown from elemental sources in a vacuum evaporation system appear to lie along a pseudobinary tie line between Cu$_2$Se and In$_2$Se$_3$ with CuInSe$_2$ at the midpoint of this tie line. Another observation used in the assumptions that follow is that Se$_2$ and In$_2$Se are the predominate species volatilized from In$_2$Se$_3$ and CuInSe$_2$ (Mills, 1974; Lamereaux et al., 1983). Based on these observations the following constraints and assumptions are used to simplify the model equations.

1. The selenium incident flux is in excess relative to copper or indium:

$$r(i, \mathrm{Se}) \gg r(i, \mathrm{Cu}) + r(i, \mathrm{In}) \tag{46}$$

This is a constraint rather than an assumption, and reflects the fact that copper and indium are so involatile that without an excess flux of selenium, elemental deposits of copper and indium would form.

2. The incident and reflected flux of the compounds Cu$_2$Se,

In_2Se_3, and $CuInSe_2$ are zero:

$$r(i, \mathrm{Cu_2Se}) = r(i, \mathrm{In_2Se_3}) = r(i, \mathrm{CuInSe_2}) = 0 \qquad (47)$$

$$r(r, \mathrm{Cu_2Se}) = r(r, \mathrm{In_2Se_3}) = r(r, \mathrm{CuInSe_2}) = 0 \qquad (48)$$

Unlike the (CdZn)S and (HgCd)Te material systems, only elemental evaporation sources have been successfully used for $CuInSe_2$ depositions (Michelsen and Chen, 1980; Birkmire et al., 1984). Because of this and the fact that the rate of forming the compound species in the vacuums used is negligible, only elemental species exist in the incident flux.

3. The rate of emission of the compound components Cu_2Se, In_2Se_3, and $CuInSe_2$ are negligible:

$$r(e, \mathrm{Cu_2Se}) = r(e, \mathrm{In_2Se_3}) = r(e, \mathrm{CuInSe_2}) = 0 \qquad (49)$$

These components either do not exist as adsorbed single molecules or they undergo dissociative evaporation.

4. All the copper that is adsorbed, $\delta(\mathrm{Cu})\, r(i, \mathrm{Cu})$, reacts to form a selenide compound:

$$r(rxt, \mathrm{Cu}) = \delta(\mathrm{Cu}) r(i, \mathrm{Cu}) \qquad (50)$$

This is a result of the excess selenium and the highly favorable reaction to form either of the selenide compounds, Cu_2Se or $CuInSe_2$.

5. All the indium that is adsorbed, $\delta(\mathrm{In}) r(i, \mathrm{In})$, reacts to form a selenide compound and is subsequently deposited or is emitted as In_2Se:

$$\delta(\mathrm{In}) r(i, \mathrm{In}) = r(rxt, \mathrm{In}) - 2r(e, \mathrm{In_2Se}) \qquad (51)$$

This results from the use of excess selenium, the favorable reaction to form the selenide compounds, and is consistent with observations (Mills, 1974; Lamereaux et al., 1983) that In_2Se is volatile at the temperatures of interest (~400°C).

6. The rate of formation of adsorbed In_2Se is governed by two reversible reactions that are at equilibrium:

a. For $Cu_2Se(s) + CuInSe_2(s)$ two-phase mixture:

$$2\mathrm{CuInSe_2}(s) \xleftrightarrow{K(\mathrm{CuInSe_2})} \mathrm{Cu_2Se}(s) + \mathrm{IN_2Se}^a + \mathrm{Se}_2^a \qquad (52)$$

where

$$K(\mathrm{CuInSe_2}) = r(e, \mathrm{Se}) r(e, \mathrm{In_2Se}) \qquad (53a)$$

$$K(\mathrm{CuInSe_2}) \alpha [\mathrm{Se}_2^a][\mathrm{In_2Se}^a] \qquad (53b)$$

b. For $In_2Se_3(s) + CuInSe_2(s)$ two-phase mixture:

$$\mathrm{In_2Se_3}(s) \xleftrightarrow{K(\mathrm{In_2Se_3})} \mathrm{In_2Se}^a + \mathrm{Se}_2^a \qquad (54)$$

where

$$K(\mathrm{In_2Se_3}) = r(e, \mathrm{Se}) r(e, \mathrm{In_2Se}) \qquad (55a)$$

$$K(\mathrm{In_2Se_3}) \alpha [\mathrm{Se}_2^a][\mathrm{In_2Se}^a] \qquad (55b)$$

and

$$K(\mathrm{In_2Se_3}) > K(\mathrm{CuInSe_2})$$

7. $CuInSe_2$ is assumed to be a pseudobinary formed from equal amounts of $Cu_2Se + In_2Se_3$:

a. If $r(rxt, \mathrm{Cu}) > r(rxt, \mathrm{In})$ then (56)

$$r(d, \mathrm{CuInSe_2}) = r(rxt, \mathrm{In}) \qquad (57)$$

$$r(d, \mathrm{Cu_2Se}) = \tfrac{1}{2}[r(rxt, \mathrm{Cu}) - r(rxt, \mathrm{In})] \qquad (58)$$

$$r(d, \mathrm{In_2Se_3}) = 0 \qquad (59)$$

b. If $r(rxt, \mathrm{In}) > r(rxt, \mathrm{Cu})$ then (60)

$$r(d, \mathrm{CuInSe_2}) = r(rxt, \mathrm{Cu}) \qquad (61)$$

$$r(d, \mathrm{Cu_2Se}) = 0 \qquad (62)$$

$$r(d, \mathrm{In_2Se_3}) = \tfrac{1}{2}[r(rxt, \mathrm{In}) - r(rxt, \mathrm{Cu})] \qquad (63)$$

c. If $r(rxt, \mathrm{In}) = r(rxt, \mathrm{Cu})$ then (64)

$$r(d, \mathrm{CuInSe_2}) = r(rxt, \mathrm{Cu}) \qquad (65)$$

$$r(d, \mathrm{Cu_2Se}) = 0 \qquad (66)$$

$$r(d, \mathrm{In_2Se_3}) = 0 \qquad (67)$$

Table 3. $CuInSe_2$ Deposition Model Equations and Parameters

Equations	
$r(rxt, \mathrm{Cu}) = \delta(\mathrm{Cu})\, r(i, \mathrm{Cu})$	(50)
$r(rxt, \mathrm{In}) = \delta(\mathrm{In})\, r(i, \mathrm{In}) - 2\, r(e, \mathrm{In_2Se})$	(51)
$r(rxt, \mathrm{Se}) = \tfrac{1}{2} r\,(rxt, \mathrm{Cu}) + \tfrac{3}{2} r(rxt, \mathrm{In})$	(68)
$r(e, \mathrm{Se}) = \delta(\mathrm{Se})\, r(i, \mathrm{Se}) - r\,(rxt, \mathrm{Se}) - r\,(e, \mathrm{In_2Se})$	(69)
If $Cu_2Se(s) + CuInSe_2(s)$ two-phase mixture is formed	
$r(e, \mathrm{In_2Se}) = K(\mathrm{CuInSe_2})/r(e, \mathrm{Se})$	(70)
$r(rxt, \mathrm{Cu}) > r(rxt, \mathrm{In})$	(56)
$r(d, \mathrm{CuInSe_2}) = r(rxt, \mathrm{In})$	(57)
$r(d, \mathrm{Cu_2Se}) = \tfrac{1}{2}[r(rxt, \mathrm{Cu}) - r\,(rxt, \mathrm{In})]$	(58)
$r(d, \mathrm{In_2Se_3}) = 0$	(59)
If $In_2Se_3(s) + CuInSe_2(s)$ two-phase mixture is formed	
$r(e, \mathrm{In_2Se}) = K(\mathrm{In_2Se_3})/r(e, \mathrm{Se})$	(71)
$r(rxt, \mathrm{In}) > r(rxt, \mathrm{Cu})$	(60)
$r(d, \mathrm{CuInSe_2}) = r(rxt, \mathrm{Cu})$	(61)
$r(d, \mathrm{Cu_2Se}) = 0$	(62)
$r(d, \mathrm{In_2Se_3}) = \tfrac{1}{2}[r(rxt, \mathrm{In}) - r\,(rxt, \mathrm{Cu})]$	(63)
If single-phase $CuInSe_2(s)$ is formed	
$K(\mathrm{CuInSe_2})/r(e, \mathrm{Se}) < r(e, \mathrm{In_2Se}) < K(\mathrm{In_2Se_3})/r(e, \mathrm{Se})$	(72)
$r(rxt, \mathrm{In}) = r(rxt, \mathrm{Cu})$	(64)
$r(d, \mathrm{CuInSe_2}) = r(rxt, \mathrm{Cu})$	(65)
$r(d, \mathrm{Cu_2Se}) = 0$	(66)
$r(d, \mathrm{In_2Se_3}) = 0$	(67)

Parameters	Value	Units
$\delta(\mathrm{Cu})$, $\delta(\mathrm{In})$, $\delta(\mathrm{Se})$	0.9	—
$K(\mathrm{CuInSe_2})$	8.3×10.6 $10^{[7.630(1/673 - 1/(T_s - 673))]}$	$\mathrm{kmol/m^2 \cdot s}$
$K(\mathrm{In_2Se_3})$	5.8×10.7 $10^{[7.630(1/673 - 1/(T_s + 673))]}$	$\mathrm{kmol/m^2 \cdot s}$

Substituting these assumptions and simplifications, Eqs. 46–67, into the model and simplifying gives the set of equations shown in Table 3. Although these equations appear dissimilar to those used in the (CdZn)S and (HgCd)Te material systems, they were derived using the same basic mass balances and assuming the same underlying rate processes: adsorption-reflection, emission, and reaction. The model parameters were either set to some reasonable value (the reflection factors equal to 0.9), or were adjusted to give reasonable agreement to available data (Thornton et al., 1984).

Figure 9 shows the overall composition and the conditions necessary to form single-phae $CuInSe_2$. The predictions were calculated for the experimental conditions used to generate the data of Thornton et al. (1984) shown in the inset of Figure 9. There is close agreement between the predicted and measured film compositions. Further, several trends predicted by the model are verified by the data. Specifically, the single-phase $CuInSe_2$ field appears at copper incident flux rates, $r(i, Cu)$, that are less than the indium incident flux rate. This is a result of the emission of In_2Se from the film. The relative composition of copper to indium is larger in the film than it is in the incident flux. For example, at a copper incident flux rate of 2.7×10^{-8} kmol/m² · s, corresponding to a copper to indium flux ratio of 0.53, the copper to indium ratio in the film is one. This reflects the fact that In_2Se is less likely to be emitted from $CuInSe_2$ than from In_2Se_3.

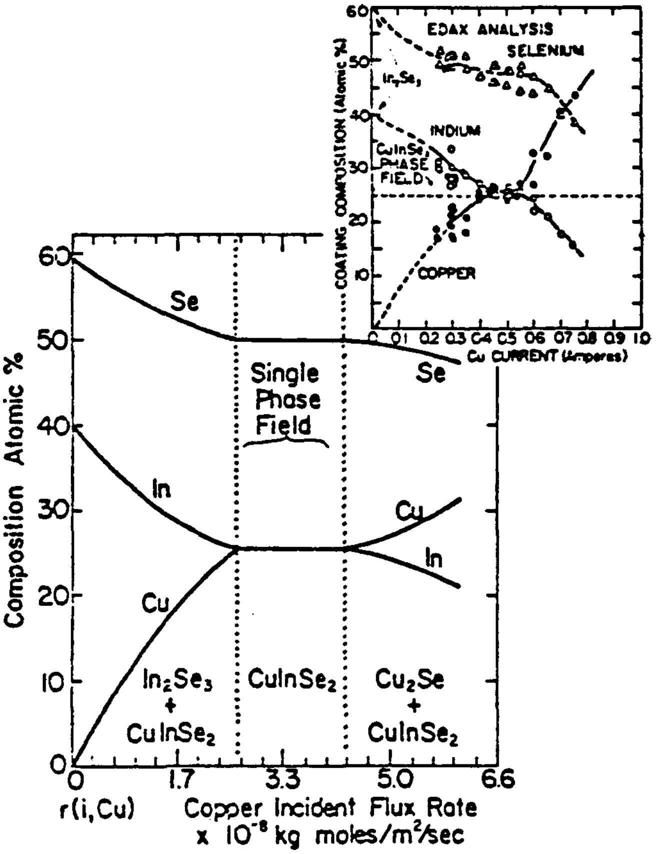

Figure 9. Effect of Cu incident flux on predicted and observed $CuInSe_2$ composition.

Data of Thornton et al. (1984).
Substrate temp., ~400°C
$r(i, In)$ 5×10^{-8} kmol/m² · s
$r(i, Se)$ 1.7×10^{-8} kmol/m² · s

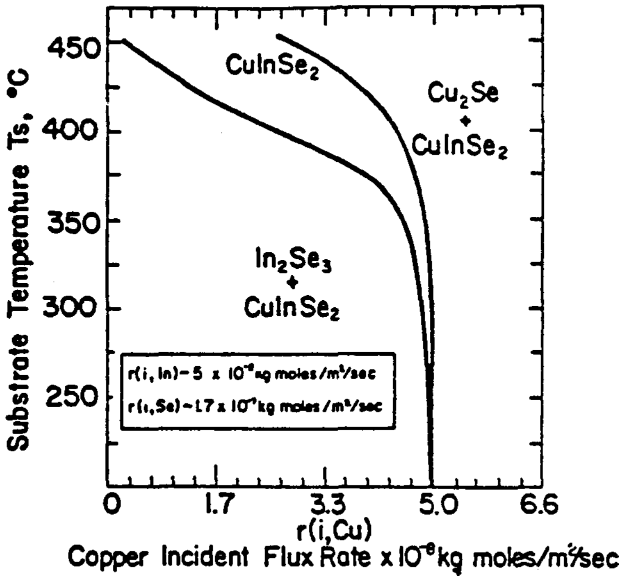

Figure 10. Predicted $CuInSe_2$ single-phase field as a function of substrate temperature and Cu incident flux.

Figure 10 shows how the predicted single-phase $CuInSe_2$ field is shifted with substrate temperature. This field widens and shifts to a lower copper incident flux rate as the substrate temperature is increased. This is consistent with the observation of Michelsen and Chen (1980) and Birkmire et al. (1984) that a lower amount of copper, relative to indium, is required when substrate temperatures are shifted from 350 to 450°C in order to produce device quality (single-phase) $CuInSe_2$ material.

Conclusions

Model equations based on the principle of mass conservation and appropriate constitutive relations have been developed to provide a mathematical description of the physical vapor deposition of a number of important semiconductor films, including (CdZn)S, (HgCd)Te, and $CuInSe_2$. The model predicts the growth rate, alloy composition, and conditions where codeposition of an elemental or second compound phase occurs. The model predictions were shown to agree with available data over a wide range of deposition conditions for all three material systems. The model has, for the first time, quantified several important experimental observations including: the effects of substrate temperature and incident flux on the conversion of incident species, and on the composition of an alloy (Figures 3, 4, 5, 7, and 8); the conditions where an element is codeposited with the compound (Figure 6); and the deposition conditions needed to grow single or multiple compound phases in a film (Figures 9 and 10).

The agreement of the model with the wide range of available data make the model useful for the analysis of bench-scale experiments and the design of large-scale systems. Despite the agreement between the model and available experimental observations, more data are needed to verify the model over a wider parameter space and refine the estimates of the model parameters.

Notation

A, B – arbitrary elemental species from column II or III of the Periodic Table

E – activation energy of the forward reaction rate constant, Eq. 13, J, kcal/mol, ergs, or eV
$Ev(j)$ – emission factor, Eq. 4, 1/s
j – arbitrary elemental or compound species
$[j^*]$ – surface concentration of adsorbed adatoms, kmol/m^2 or no./cm^2
$-K(AY)$ – apparent reaction rate constant, Eqs. 25, 26
$k_f(AY), k_f(BY)$ – true forward reaction rate constant for the formation of AY and BY compounds
$k_r(AY), k_r(BY)$ – reverse reaction rate constants for AY and BY compounds, kmol/m^2/s
k' – preexponential factor for reaction rate constants, Eq. 13
m, n – order of compound formation reaction with respect to each component
Mj – mass of component j in control volume, kg or g
$Mw(j)$ – molecular weight, kg/kmol, g/gmol, or g/no.
$P(T_a, j), P(T_s, j)$ – vapor pressure of species j evaluated at adatom temperature or substrate temperature, Pa, dynes/cm^2
R_g – gas law constant
$r(d, j)$ – deposition rate or rate of accumulation of component j inside control volume, kmol/$m^2 \cdot$ s, no./$cm^2 \cdot$ s
$r(e, j)$ – rate of emission of component j from control volume, kmol/$m^2 \cdot$ s, no./$cm^2 \cdot$ s
$r(e_{max}, j)$ – maximum rate of emission of component j, Eq. 15, kmol/$m^2 \cdot$ sec, no./$cm^2 \cdot$ s
$r(i, j)$ – rate of incident flux of component j into control volume, kmol/$m^2 \cdot$ sec, no./$cm^2 \cdot$ s
$r(rxt, j)$ – rate of reaction of component j within control volume, kmol/$m^2 \cdot$ sec, no./$cm^2 \cdot$ s
$r(r, j)$ – rate of reflection of component j within control volume, kmol/$m^2 \cdot$ sec, no./$cm^2 \cdot$ s
T_a, T_s – adatom and substrate temperatures, K
T_i – temperature of incident beam
t – time, s
x – composition of ternary alloy, atomic fraction
Y – arbitrary elemental component for column V or VI of the Periodic Table

Greek letters

$\alpha_v(j), \alpha_v$ – evaporation coefficient of component j
$\delta(j), \delta$ – reflection factors
ϵ – thermal accommodation coefficient, Eq. 43
λ – relative amount of an element codeposited in a film, Eq. 5
η – material conversion, Eqs. 45, 46
ϕ – surface area covered by control volume, m^2 or cm^2

Literature cited

Baron, B. N., and S. C. Jackson, "Fundamental Engineering Analysis of CdTe/CdS Photovoltaic Processing, Final Report," SERI Subcontract XL-4-03146-1, Jan. 1986, SERI Pub. No. SERI/STR-211-2970 (1986).

Birkmire, R. W., R. B. Hall, and J. E. Phillips, "Material Requirements for High-Efficiency $CuInSe_2$/CdS Solar Cells," *17th IEEE PV Specialists Conf.* Orlando, 882 (1984).

Brody, T. P., "The Thin Film Transistor—A Late Flowering Bloom," *IEEE Trans. Electronic Dev.*, 180-3(11), 1614 (1984).

Bunshah, R. F., et al., *Deposition Technologies for Films and Coatings Developments and Applications*, Noyes, Park Ridge, NJ (1982).

Carberry, J. J., *Chemical and Catalytic Reaction Engineering*, McGraw-Hill, New York, 382–394 (1976).

Chow, P. P., and D. Johnson, "Growth and Characterization of MBE-Grown HgTe-CdTe Superlattices," *J. Vac. Sci. Tech.*, A3(1), 67 (1985).

Dayton, B. B., "Gas Flow Patterns at Entrance and Exit of Cylindrical Tubes," *Trans. 2nd Amer. Vacuum Soc. Vac. Symp.*, 5, 5 (1961).

Don, E. R., S. J. Russell, and R. Hill, "RHEED Studies of $CuInSe_2$ Epitaxial Films," *18th IEEE PV Specialists Conf.*, Las Vegas, 1060 (1985).

Eyring, H., F. M. Wanlass, and E. M. Eyring, Chap. 1, *Condensation and Evaporation of Solids*, E. Rutner, P. Goldfinger, and J. P. Hirth, eds., Gordon and Breach, Neww York, (1964).

Faurie, J. P., private communication (Oct., 1985).

Faurie, J. P., A. Million, R. Boch, and J. L. Tissot, "Latest Developments in the Growth of $Cd_xHg_{1-x}Te$ and CdTe-HgTe Superlattices by Molecular Beam Epitaxy," *J. Vac. Sci. Tech.*, A1(3), 1593 (1983).

Faurie, J. P., M. Boukirche, J. Reno, S. Strananthan, and C. Hsu, "Molecular Beam Epitaxy of Alloys and Superlattices Involving Mercury," *J. Vac. Sci. Tech.*, A3(1), 55 (1985).

Foxon, C. T., "MBE Growth of GaAs and III-V Alloys," *J. Vac. Sci. Tech.*, B1(2), 293 (1983).

Freller, H., and K. G. Gunther, "Three-Temperature Method as an Origin of Molecular Beam Epitaxy," *Thin Solid Films*, **88**, 291 (1982).

Giordmaine, J. A., and T. C. Wang, "Molecular Beam Formation by Long Parallel Tubes," *J. Appl. Phys.*, **31**, 463 (1960).

Gunther, K. G., *The Use of Thin Films in Physical Investigations*, J. C. Anderson, ed. Academic Press, New York, 213–231 (1968).

Hirth, J. P., Chap. 5, *Vapor Deposition*, C. F. Powell, J. H. Oxles, and J. M. Blocher, eds., Wiley, New York (1966).

Hirth, J. P., and G. H. Pound, "Coefficients of Evaporation and Condensation," *J. Phys. Chem.*, **64**, 619 (1960).

Jackson, S. C., "Engineering Analysis of the Deposition of Cadmium-Zinc Sulfide Semiconductor Film," Ph.D. Diss., Univ. Delaware, Newark (1984).

Jackson, S. C., B. N. Baron, R. E. Rocheleau, and T. W. F. Russell, "Molecular Beam Distribution from High Rate Sources," *J. Vac. Sci. Tech.*, A3(5), 1916 (1985).

Jansen, F., and A. R. Melnyk, "The Evaporation and Condensation of As_2Se_3-like Materials," *J. Vac. Sci. Tech.*, A2(3), 1248 (1984).

Kawabe, M., and N. Matsiura, "Preferential Desorption of Ga from Al_xGa_{1-x} as Grown by Molecualr Beam Epitaxy," *Japan J. Appl. Phys.*, 23(6), L351 (1984).

Lamereaux, R. H., K. H. Lau, and R. D. Brittain, "High-Temperature Equilibrium Studies of Copper Indium Selenide," Final Report SERI Subcontract XZ-2-02001 (Mar. 4, 1983).

Michelsen, R. A., and W. S. Chen, "High Photocurrent Polycrystalline Thin-Film CdS/$CuInSe_2$ Solar Cell," *Appl. Phys. Lett.*, **36**, 371, (1980).

Mills, K. C., *Thermodynamic Data for Inorganic Sulphides, Selenides, and Tellurides*, Butterworth, London (1974).

Mino, N., M. Kobayashi, M. Konagai, and K. Takahashi, "Epitaxial Growth of High-Quality ZnSe on Si Substrates by Molecular Beam Epitaxy and Application to DC Electroluminescent Cells," *J. Appl. Phys.*, 58(2), 793 (1985).

Myers, T. H., A. W. Waltner, and J. F. Schetzinor, "Properties of CdTe-Te Alloy Films Prepared Using Molecular Beams," *J. Appl. Phys.*, 53(8), 5697 (1982).

Palatnik, L. S., and E. R. Rogacheva "Phase Diagrams and Structure of Some Semiconductor $A_2^{I}C^{VI}$-$B_2^{III}C^{VI}$ Alloys," *Sov. Phys. Dok.*, **12**, 503 (1967).

Rocheleau, R. E., B. N. Baron, and T. W. F. Russell, "Analysis of Evaporation of Cadmium Sulfide for Manufacture of Solar Cells," *AIChE J.*, **28**, 656 (1982).

Russell, T. W. F., B. N. Baron, and R. E. Rocheleau, "Fundamentals and Application of Solar Energy. II," *AIChE Symp. Ser.*, S-210 (1979).

Smith, D. L., and V. Y. Pickhardt, "Molecular Beam Epitaxy of II-VI Compounds," *J. Appl. Phys.*, 46(6), 2366 (1975).

Somerjai, G. A., and D. W. Jepsen, "Evaporation Mechanism of CdS Single Crystals. I: Surface Concentration and Temperature Dependence of the Evaporation Rate," *J. Chem. Phys.*, 41(5), 1389 (1964).

Stickney, R. E., and R. F. Keating, S. Yamamoto, and W. J. Hastings, "Angular Distributions of Flow from Orifices and Tubes at High Knudsen Numbers," *J. Vac. Sci. Tech.*, 4(1), 10 (1968).

Stolt, L., M. Jargelius, J. Hedstrom, D. Sigurd, and E. Niemi, "Growth of $CuInSe_2$ Thin Films," *18th IEEE PV Specialists Conf.*, Las Vegas, 1047 (1985).

Summers, C. J., E. L. Meeks, and N. W. Cox, "Molecular Beam Epitaxial Growth of CdTe, HgTe, and $Hg_{1-x}CdXTe$ Alloys," *J. Vac. Sci. Tech.*, B2(2), 224 (1984).

Thornton, J. A., D. G. Cerneg, R. B. Hall, S. P. Shea, and J. D. Meakin, "Reactive Sputtered Copper Indium Diselenide Films for Photovoltaic Applications," *J. Vac. Sci. Tech.*, A2(2), [illegible]7 (1984).

Manuscript received Feb. 11, 1986, and revision received Oct. 27, 1986.

Appendix 2

Heat Treatment Procedures

Heating:

Heat treatments are performed in a tube furnace fitted with a quartz liner measuring 6 cm in diameter and 50 cm in length. For air heat treatments the furnace is used in a static flow condition in which the ends of the liner are capped. Flowing conditions are possible by using end caps fitted with gas feed through fixtures.

Samples are paddle-loaded onto a flat ceramic block measuring 4 cm by 4 cm by 2 cm. The block is embedded with a type K thermocouple whose leads are conducted to the outside through a ceramic sheath bonded to the block. In practice, the block is continuously left in the hot furnace. Heatup to nearly 550°C is estimated to take between thirty seconds and one minute. Typically, when samples are loaded, the monitor thermocouple registers a 20 to 30°C drop in temperature. Recovery to the original reading takes between one and two minutes.

Cooling:

Quick cooling involves rapid transfer of the hot sample to a suitable heat sink. A 15 cm by 15 cm by 3 cm aluminum block fitted with an internal flowing water heat exchange manifold and monitor thermocouple is used. The surface of the block is highly polished to provide good physical contact to the sample through surface tension. In practice, the block temperature reads 12 to 13°C in winter and 14 to 15°C in summer.

The ceramic heating block and thermocouple sheath, with sample on top, are withdrawn from the hot oven at the end of the prescribed heat treatment time. The sheath is rotated to allow the sample to fall face-up onto the cooling block. Cooling in this manner from 550°C is estimated to proceed at greater than 100C/sec.

Slow cooling involves removal of the liner and block assembly to the room at the end of the appointed time. For a 550°C heat treatment, cooling the sample to room temperature takes about 20 minutes. For the first 200 degrees, cooling proceeds at about 10C/sec and thereafter at about 0.5C/sec.